# Lawrence Berkeley National Laboratory

## Lawrence Berkeley National Laboratory

### Title

Inventory of Shale Formations in the US, Including Geologic, Hydrological, and Mechanical Characteristics

### Permalink

https://escholarship.org/uc/item/3km9d255

### Author

Dobson, Patrick

### Publication Date

2014-06-01

eScholarship.org Powered by the California Digital Library
University of California

# *Inventory of Shale Formations in the US Including Geologic, Hydrological, and Mechanical Characteristics*

## Fuel Cycle Research & Development

*Prepared for*

*U.S. Department of Energy*
*Used Fuel Disposition*

*Patrick Dobson and*
*James Houseworth*

*Lawrence Berkeley National Laboratory*

*November, 2013*

**FCRD-UFD-2014-000513**
**LBNL-6633E**

**DISCLAIMER**

This information was prepared as an account of work sponsored by an agency of the U.S. Government. While this document is believed to contain correct information, Neither the U.S. Government nor any agency thereof, nor the Regents of the University of California, nor any of their employees, makes any warranty, expressed or implied, or assumes any legal liability or responsibility for the accuracy, completeness, or usefulness, of any information, apparatus, product, or process disclosed, or represents that its use would not infringe privately owned rights. References herein to any specific commercial product, process, or service by trade name, trade mark, manufacturer, or otherwise, does not necessarily constitute or imply its endorsement, recommendation, or favoring by the U.S. Government or any agency thereof, or the Regents of the University of California. The views and opinions of authors expressed herein do not necessarily state or reflect those of the U.S. Government or any agency thereof or the Regents of the University of California.

Revision 2
12/20/2012

# APPENDIX E
# FCT DOCUMENT COVER SHEET [1]

| | |
|---|---|
| Name/Title of Deliverable/Milestone/Revision No. | Inventory of Shale Formations in the US, Including Geologic, Hydrological, and Mechanical Characteristics |
| Work Package Title and Number | Regional Geology R&D - LBNL FT-14LB081402 |
| Work Package WBS Number | 1.02.08.14 |
| Responsible Work Package Manager | Patrick Dobson (Name/Signature) (Signature on File) |

Date Submitted 11/22/2013

| | | | | |
|---|---|---|---|---|
| Quality Rigor Level for Deliverable/Milestone[2] | ☐ QRL-3 | ☐ QRL-2 | ☐ QRL-1<br>☐ Nuclear Data | ☒ Lab/Participant QA Program (no additional FCT QA requirements) |

This deliverable was prepared in accordance with Lawrence Berkeley National Laboratory
*(Participant/National Laboratory Name)*

QA program which meets the requirements of
☒ DOE Order 414.1 ☐ NQA-1-2000 ☐ Other

**This Deliverable was subjected to:**

☐ Technical Review

**Technical Review (TR)**

**Review Documentation Provided**

☐ Signed TR Report or,

☐ Signed TR Concurrence Sheet or,

☐ Signature of TR Reviewer(s) below

☐ Peer Review

**Peer Review (PR)**

**Review Documentation Provided**

☐ Signed PR Report or,

☐ Signed PR Concurrence Sheet or,

☐ Signature of PR Reviewer(s) below

**Name and Signature of Reviewers**

**NOTE 1:** *Appendix E should be filled out and submitted with the deliverable. Or, if the PICS:NE system permits, completely enter all applicable information in the PICS:NE Deliverable Form. The requirement is to ensure that all applicable information is entered either in the PICS:NE system or by using the FCT Document Cover Sheet.*

**NOTE 2**: *In some cases there may be a milestone where an item is being fabricated, maintenance is being performed on a facility, or a document is being issued through a formal document control process where it specifically calls out a formal review of the document. In these cases, documentation (e.g., inspection report, maintenance request, work planning package documentation or the documented review of the issued document through the document control process) of the completion of the activity along with the Document Cover Sheet is sufficient to demonstrate achieving the milestone. If QRL 1, 2, or 3 is not assigned, then the Lab/Participant QA Program (no additional FCT QA requirements box must be checked, and the work is understood to be performed, and any deliverable developed, in conformance with the respective National Laboratory/Participant, DOE- or NNSA-approved QA Program.*

This page is intentionally blank.

# SUMMARY

*Inventory of Shale Formations in the US*

This section provides a summary of the distribution, thickness, and depth of selected shale formations found within many of the sedimentary basins in the contiguous US. Clay-rich shale formations have a number of properties, such as low permeability, high cation exchange potential, and the ability to self seal, which make them candidates for a geologic repository for high-level radioactive waste. The United States has an abundance of thick shale deposits that span a wide range of geologic ages, mineralogic compositions, and geologic environments, some of which might be suitable for hosting repositories to safeguard radioactive waste. The objective of this report is to build upon previous compilations of shale formations within many of the major sedimentary basins in the US by developing GIS data delineating isopach and structural depth maps for many of these units. These data are being incorporated into the LANL digital GIS database being developed for determining host rock distribution and depth/thickness parameters consistent with repository design.

*Rock Properties and In-Situ Conditions for Shale Estimated from Sonic Velocity Measurements*

This section presents the development of methods to assess hydrological and geomechanical properties and conditions for shale formations based on sonic velocity measurements. Publically available data sets have been identified for shales under investigation for nuclear waste disposal in Europe and from shales of interest for oil exploration and production in the North Sea. These data have been used in the development of several correlations which link properties to sonic compressional velocity. The advantage of using correlations based on sonic velocity is that properties can be estimated from geophysical logs. This information is often more readily available than direct property measurements on core that would otherwise be required. Furthermore, geophysical logs typically provide a continuous readout along wells that can be more readily used to characterize spatial variability in properties. The correlations developed are then used to assess properties and conditions in several shale formations of interest within the United States which have publically available data on sonic velocity. Some of the proposed correlations have been previously investigated by others and comparisons between correlations are reasonably consistent. The approach has been extended here to other properties as well as in-situ conditions, in particular, a method to estimate pore-fluid pressure. A method is also developed and used to account for anisotropy for properties where sufficient information is available to assess directional dependence. Some of the correlations, in particular estimation of sonic velocity parallel to bedding from normal to bedding sonic velocity measurements, and estimation of clay content from sonic velocity were found to be weak, indicating that additional independent measurements are desirable to supplement such estimates. Several of the correlations were also constructed from small data sets and require additional data for greater confidence. Similarly, several factors that can influence properties have not been investigated here, including confining stress, fluid saturation conditions, and the organic content of shale. Further verification is also needed for many of the parameter estimates for the US shale formations analyzed; therefore, they should be viewed as initial estimates.

# CONTENTS

1. INTRODUCTION ..... 1

2. INVENTORY OF SHALE FORMATIONS IN THE US ..... 1
- 2.1 INTRODUCTION ..... 1
- 2.2 DATA SOURCES ..... 1
- 2.3 ISOPACH AND STRUCTURE MAPS ..... 3
  - 2.3.1 Appalachian Basin ..... 6
  - 2.3.2 Black Warrior Basin ..... 9
  - 2.3.3 Illinois Basin ..... 10
  - 2.3.4 Michigan Basin ..... 12
  - 2.3.5 Anadarko, Ardmore, and Arkoma Basins ..... 14
  - 2.3.6 Gulf of Mexico Basin ..... 18
  - 2.3.7 Fort Worth Basin ..... 20
  - 2.3.8 Permian Basin ..... 21
  - 2.3.9 Williston Basin ..... 23
  - 2.3.10 Powder River Basin ..... 25
  - 2.3.11 Denver Basin ..... 26
  - 2.3.12 San Juan Basin ..... 27
  - 2.3.13 Green River, Piceance, and Uinta Basins ..... 28
  - 2.3.14 San Joaquin, Santa Maria, and Cuyama Basins ..... 29
- 2.4 CONCLUSIONS ..... 31
- 2.5 REFERENCES ..... 32

3. ROCK PROPERTIES AND IN-SITU CONDITIONS FOR SHALE ESTIMATED FROM SONIC VELOCITY MEASUREMENTS ..... 40
- 3.1 DATA USED TO DEVELOP THE CORRELATIONS ..... 40
- 3.2 THE DEVELOPMENT OF CORRELATIONS TO ASSESS FORMATION PROPERTIES AND CONDITIONS ..... 44
  - 3.2.1 Treatment of Anisotropic Sonic Velocities ..... 44
  - 3.2.2 The Porosity – Seismic Velocity Correlation ..... 47
  - 3.2.3 The Bulk Density – Seismic Velocity Correlation ..... 48
  - 3.2.4 The Clay Content – Seismic Velocity Correlation ..... 50
  - 3.2.5 The Permeability – Porosity - Clay Content Correlation ..... 51
  - 3.2.6 The Porosity–Maximum Effective Stress–Clay Content Correlation ..... 53
  - 3.2.7 Young's Modulus - Seismic Velocity Correlations ..... 56
  - 3.2.8 Shear Modulus – Seismic Velocity Correlation ..... 58
  - 3.2.9 Poisson's Ratio - Seismic Velocity Correlation ..... 60
  - 3.2.10 Cohesive Strength - Seismic Velocity Correlations ..... 61
  - 3.2.11 Friction Angle - Seismic Velocity Correlation ..... 63
  - 3.2.12 Tensile Strength – Seismic Velocity Correlations ..... 65
- 3.3 APPLICATION TO US SHALE FORMATIONS ..... 67
  - 3.3.1 Inputs ..... 67
  - 3.3.2 Correlations Results ..... 68
  - 3.3.3 Barnett Shale ..... 71
  - 3.3.4 Haynesville Shale ..... 71

3.3.5 Pierre Shale ..... 71
3.3.6 Monterey Shale ..... 72
3.4 CONCLUSIONS ..... 72
3.5 REFERENCES ..... 73

4. ACKNOWLEDGMENTS ..... 78

# FIGURES

Figure 2-1. Sedimentary basins in the contiguous US. (Coleman and Cahan, 2012)..... 2

Figure 2-2. Depth and isopach maps of the Utica Shale, Appalachian Basin. Figure produced by LANL from shale data populated into the GIS database. ..... 6

Figure 2-3. Depth and isopach maps of the Marcellus Shale, Appalachian Basin. Figure produced by LANL from shale data populated into the GIS database. ..... 7

Figure 2-4. Variation in total organic carbon in the Utica Shale (Engelder, 2011)..... 8

Figure 2-5. Isopach map of the Chattanooga Shale within the Alabama portion of the Black Warrior Basin (Pashin, 2008) ..... 9

Figure 2-6. Depth and isopach maps of the New Albany Shale, Illinois Basin. Figure produced by LANL from shale data populated into the GIS database. ..... 10

Figure 2-7. Depth and isopach maps of the Maquoketa Shale, Illinois Basin. Figure produced by LANL from shale data populated into the GIS database. ..... 11

Figure 2-8. Structure map of the Antrim Shale, Michigan Basin (Wylie and Wood, 2005). Gas wells are depicted as red dots. ..... 12

Figure 2-9. Depth and isopach maps of the Coldwater Shale, Michigan Basin. Figure produced by LANL from shale data populated into the GIS database. ..... 13

Figure 2-10. Depth and isopach maps of the Kiowa Shale, Anadarko Basin. Figure produced by LANL from shale data populated into the GIS database. ..... 14

Figure 2-11. Depth and isopach maps of the Graneros Shale, Anadarko Basin. Figure produced by LANL from shale data populated into the GIS database. ..... 15

Figure 2-12. Depth and isopach maps of the Fayetteville Shale, Arkoma Basin. Figure produced by LANL from shale data populated into the GIS database. ..... 16

Figure 2-13. Depth and isopach maps of the Woodford Shale, Anadarko and Arkoma Basins. Figure produced by LANL from shale data populated into the GIS database..... 17

Figure 2-14. Depth and isopach maps of the Haynesville Shale, Gulf of Mexico Basin. Figure produced by LANL from shale data populated into the GIS database. ..... 18

Figure 2-15. Depth and isopach maps of the Eagle Ford Formation, Gulf of Mexico Basin. Figure produced by LANL from shale data populated into the GIS database. ..... 19

Figure 2-16. Depth and isopach maps of the Barnett Shale, Fort Worth Basin. Figure produced by LANL from shale data populated into the GIS database. ..... 20

Figure 2-17. Depth and isopach maps of the Woodford Shale, Permian Basin. Figure produced by LANL from shale data populated into the GIS database. ..... 21

Figure 2-18. Depth (relative to sea level) and isopach maps of the Barnett Shale, Permian Basin (Broadhead and Gillard, 2007). ..... 22

Figure 2-19. Depth and isopach maps of the Bakken Formation, Williston Basin. Figure produced by LANL from shale data populated into the GIS database. ..... 23

Figure 2-20. Depth and isopach maps of the Bearpaw Shale, Williston Basin. Figure produced by LANL from shale data populated into the GIS database. ..... 24

Figure 2-21. Depth and isopach maps of the Pierre Shale, Powder River Basin. Figure produced by LANL from shale data populated into the GIS database. ..... 25

Figure 2-22. Depth and isopach maps of the Lebo Shale, Powder River Basin. Figure produced by LANL from shale data populated into the GIS database. ..... 26

Figure 2-23. Depth and isopach maps of the Pierre Shale in the Williston and Denver Basins. Figure produced by LANL from shale data populated into the GIS database..... 27

Figure 2-24. Depth and isopach maps of the Mancos Shale in the San Juan Basin. Figure produced by LANL from shale data populated into the GIS database. ..... 28

Figure 2-25. Depth and isopach maps of the Green River Shale in the Greater Green River, Uinta, and Piceance Basins. Figure produced by LANL from shale data populated into the GIS database. ..... 29

Figure 2-26. Depth and isopach maps of the Monterey Formation in the San Joaquin Basin (Hosford Scheirer, 2013). ..... 30

Figure 2-27. Summary of GIS data for depth to top of shale formations within major sedimentary basins in the US currently incorporated in the LANL GIS database. Figure produced by LANL from shale data populated into the GIS database. ..... 31

Figure 3-1. Velocity ratio plotted against the sonic velocity normal to bedding..... 45

Figure 3-2. Seismic velocity ratio correlation with normal sonic velocity using transformed variables. ..... 46

Figure 3-3. Seismic velocity ratio correlation with normal sonic velocity using physical variables. ..... 46

Figure 3-4. Porosity and sonic velocity correlation using transformed variables..... 47

Figure 3-5. Porosity and sonic velocity correlation using physical variables..... 48

Figure 3-6. Bulk density and sonic velocity correlation using transformed variables..... 49

Figure 3-7. Bulk density and sonic velocity correlation using physical variables..... 49

Figure 3-8. Clay content and sonic velocity correlation using transformed sonic velocity..... 50

Figure 3-9. Clay content plotted against the physical sonic velocity. ..... 51

Figure 3-10. Permeability correlation normal to bedding (using Equations 3-2, 3-4, and 3-5) compared with measurements. Note: see text near end of this section concerning ovals and rectangle. ..... 52

Figure 3-11. Permeability correlation parallel to bedding (using Equations 3-2, 3-3, and 3-4 and 3-6) compared with measurements. Note: see text near end of this section concerning ovals and rectangle..... 53

Figure 3-12. Uniaxial compressive strength normal to bedding and sonic velocity correlation using transformed variables. ..... 54

Figure 3-13. Uniaxial compressive strength and sonic velocity correlation using physical variables. ..... 55

Figure 3-14. Correlation for Young's modulus normal to bedding with sonic velocity using transformed variables. ..... 57

Figure 3-15. Correlation for Young's modulus normal to bedding with sonic velocity using physical variables. ..... 58

Figure 3-16. Correlation for Young's modulus parallel to bedding with sonic velocity. ..... 58

Figure 3-17. Correlation for shear modulus with sonic velocity using transformed variables. ..... 59

Figure 3-18. Correlation for shear modulus with sonic velocity using physical variables. ..... 60

Figure 3-19. Correlation for Poisson's ratio with sonic velocity using transformed variables. ... 61

Figure 3-20. Correlation for Poisson's ratio with sonic velocity using physical variables. ..... 61

Figure 3-21. Correlation for cohesive strength normal to bedding with sonic velocity using transformed variables. ..... 62

Figure 3-22. Correlation for cohesive strength normal to bedding with sonic velocity using physical variables. ..... 63

Figure 3-23. Correlation for cohesive strength parallel to bedding with sonic velocity ..... 63

Figure 3-24. Correlation for friction angle with sonic velocity using transformed variables ..... 64

Figure 3-25. Correlation for friction angle with sonic velocity using physical variables ..... 65

Figure 3-26. Correlation for tensile strength normal to bedding with sonic velocity using transformed variables. ..... 65

Figure 3-27. Correlation for tensile strength normal to bedding with sonic velocity using physical variables. ..... 66

Figure 3-28. Correlation for tensile strength parallel to bedding with sonic velocity. ..... 66

Figure 3-29. Map of U.S. shale gas and shale oil plays (EIA 2011). ..... 67

# TABLES

Table 2-1. Identified data sources for isopach and structural data for shale formations within major sedimentary basins..... 3

Table 3-1. Data from Boisson (2005) (except as noted)..... 41

Table 3-2. Additional Properties of Some Formations from Table 1. ..... 42

Table 3-3. Horsrud (2001) Properties Data..... 43

Table 3-4. Inputs for Properties Estimation. ..... 68

Table 3-5. Estimated Parameters Using Seismic Velocity Correlations from Section 3.2. ..... 69

# ACRONYMS

| | |
|---|---|
| BRI | brittleness index |
| DEM | Digital Elevation Model |
| EIA | Energy Information Administration |
| GIS | Geographic Information Systems |
| LANL | Los Alamos National Laboratory |
| OCR | overconsolidation ratio |
| RMSE | root-mean-square error |
| tcf | trillion cubic feet |
| TOC | total organic carbon |
| UCS | uniaxial compressive strength |
| USGS | U.S. Geological Survey |

This page is intentionally blank.

# 1. INTRODUCTION

This report documents FY13 progress for the work package entitled "Regional Geology R&D – LBNL". The major purpose of this work package is to augment the existing inventory of shale formations in the US in the LANL Geographic Information Systems (GIS) database and to examine physical properties associated with these rocks.

There are two main research tasks for this work package. The first (described in Section 2) is to build upon previous work conducted to obtain isopach and structural top data (either from published maps and figures or as GIS shape files) for selected shale units in the US through literature searches and personal contacts. The second task (described in Section 3) is to develop a methodology through the use of sonic velocity logs to estimate hydrologic and geomechanical properties of shales. Publically available field and laboratory data from shale samples have been used to develop correlations between measured sonic velocities and rock properties such as porosity, bulk density, clay content, permeability, uniaxial compressive strength, Young's modulus, and shear modulus.

# 2. INVENTORY OF SHALE FORMATIONS IN THE US

## 2.1 INTRODUCTION

Clay-rich shale formations have a number of properties, such as low permeability, high cation exchange potential, and the ability to self seal, which make them candidates for a geologic repository for high-level radioactive waste (e.g., Cuadros, 2008). The United States has an abundance of thick shale deposits that span a wide range of geologic ages, mineralogic compositions, and geologic environments, some of which might be suitable for hosting repositories to safeguard radioactive waste. The objective of this report is to build upon previous compilations of shale formations within many of the major sedimentary basins in the US (e.g., Merewether et al., 1973; Gonzales and Johnson, 1985; Dobson, 2011; 2012; Perry et al., 2012; 2013) by developing GIS data delineating isopach and structural depth maps for many of these units. These data are being incorporated into the LANL digital GIS database being developed for determining host rock distribution and depth/thickness parameters consistent with repository design (Perry et al., 2011; 2013). Three main rock types are being incorporated into this database: salts, shales, and granitic basement rocks. This database can then be utilized for screening and comparison of potential repository sites (e.g., Rechard et al., 2011). This report represents an update of the Dobson (2012) report.

## 2.2 DATA SOURCES

Most of the shale data are from sedimentary basins where oil and gas deposits are present (Figure 2-1). EIA (2011) estimates that around 750 trillion cubic feet of undeveloped technically recoverable shale gas and shale oil resources are in discovered shale plays in the lower 48 states. Formations that have been identified as having at least 20 trillion cubic feet (tcf) of shale gas include the Marcellus Shale (410 tcf), the Antrim Shale (20 tcf), the Haynesville Shale (75 tcf), the Eagle Ford Formation (21 tcf), the Fayetteville Shale (32 tcf), the Barnett and Woodford Shales (97 tcf), and the Mancos Shale (21 tcf). Many of these units are not shales in a strict

sense, but may be better described as siliceous mudstones with reduced clay contents; these slightly brittle rocks can be subjected to successful hydrofracture treatment (Gale and Holder, 2010). The EIA has also identified the Monterey Formation in California as having 15.4 billion barrels of technically recoverable shale oil. While many areas within these sedimentary basins are sites of active and prospective oil and gas exploration and development activities, there may be locations (such as within the shallower basin margins) that could be possible candidates for a repository.

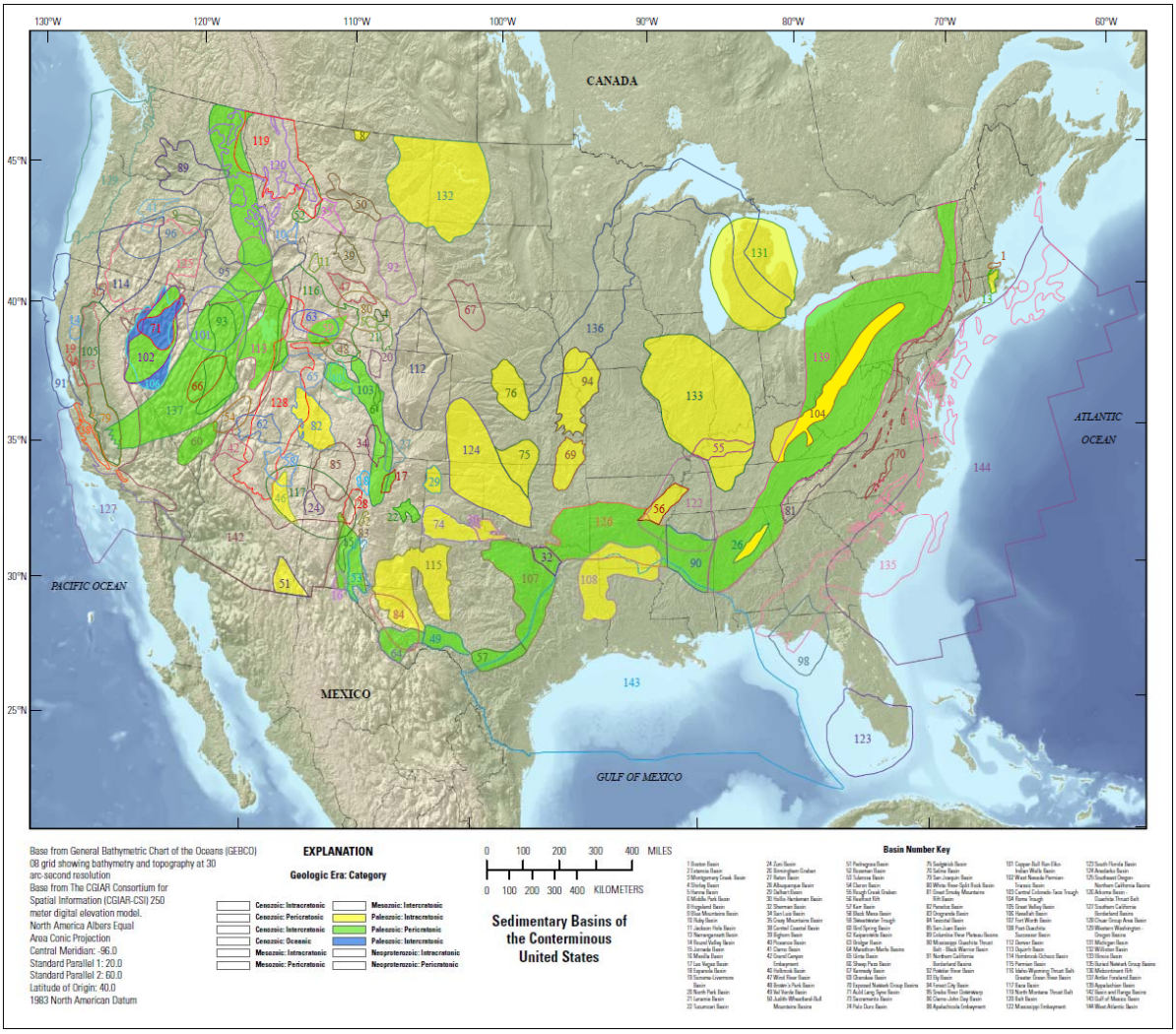


Figure 2-1. Sedimentary basins in the contiguous US. (Coleman and Cahan, 2012)

The data used for this report represent information that was either digitized using ArcGIS from published isopach and structure maps, or was available as GIS shape files that delineate formation isopachs and structural surfaces relative to a known datum, such as sea level or the

ground surface. A number of data sources were obtained from the references listed in the discussions in Hovorka et al. (2003) of seal thickness and seal continuity for different saline formations in US sedimentary basins. The U.S. Geological Survey (USGS) Digital Data Series reports on petroleum systems and geologic assessment of oil and gas resources have been another helpful source of information. Numerous state geological survey reports have provided additional detailed information on local basin stratigraphy. Where maps were used to create GIS data layers, a jpeg version of the map was georectified using multiple geographic reference points (such as country or state boundaries) and the thickness or structure contours were converted to vector format. Where depths are referenced to sea level instead of the ground surface, DEM data are used. In the case of GIS data, metadata files were used to ascertain the geodetic reference datum used. In some cases, multiple data sources were used. More details on the methodology used to create the GIS structural top and isopach shape files can be found in Perry (2012).

## 2.3 ISOPACH AND STRUCTURE MAPS

Maps of shale formation extents, thicknesses, and depths were obtained for the following units as organized by sedimentary basin. Table 2-1 summarizes formations for which isopach and/or structural data have been obtained. More comprehensive lists of shale formations can be found in Dobson (2011) and Gonzales and Johnson (1985). Units listed in ***bold italics*** represent formations for which GIS data have been obtained or generated. This report represents the current status of data collection: this is an ongoing process to populate the LANL GIS database.

Table 2-1. Identified data sources for isopach and structural data for shale formations within major sedimentary basins.

| | |
|---|---|
| **Appalachian Basin** | |
| ***Utica Shale*** | Patchen et al., 2006 (Plates 1-28 & 2-6) (GIS data obtained from West Virginia Geological and Economic Survey) |
| ***Marcellus Shale*** | Erenpreiss et al., 2011 (GIS data obtained from Ohio Department of Natural Resources) |
| Olentangy Shale | Gray et al., 1982 (METC/EGSP Series 313, 314, 318, 320) |
| Ohio Shale | Gray et al., 1982 (METC/EGSP Series 310, 311, 312, 316, 317) |
| **Black Warrior Basin** | |
| Chattanooga Shale | Pashin, 2008 (Figure 6) |
| **Illinois Basin** | |
| ***Maquoketa Shale*** | Willman et al., 1975 (Figure O-26); Collinson et al., 1988 (Figure 22); Kolata and Noger, 1990 (Figure 5-13); Bristol and Buschbach, 1973 (Plate 1) |
| ***New Albany Shale*** | Hasenmueller and Comer, 2000 (GIS data obtained from Illinois State Geological Survey) |

| | |
|---|---|
| **Michigan Basin** | |
| Eau Claire Formation | Catacosinos and Daniels, 1991 (Figure 6) |
| Antrim Shale | Wylie and Wood, 2004; 2005 |
| ***Coldwater Shale*** | Merewether et al., 1973 (Figures 12 & 13); Gonzales and Johnson, 1985 (Figure 3-20) |
| **Anadarko Basin** | |
| Sylvan Shale | Amsden, 1975 (Plates 7 & 8); Amsden, 1980 (Panel 1) |
| ***Woodford Shale*** | Amsden, 1975 (Plates 3 & 4); Cardott and Lambert, 1985 (Figures 2 & 3); Rottmann, 2000 |
| ***Kiowa Shale*** | Macfarlane et al., 1993 (Plates 7 & 8) |
| ***Graneros Shale*** | Macfarlane et al., 1993 (Plates 3 & 4) |
| **Ardmore Basin** | |
| ***Woodford Shale*** | Party et al., 2008 (Slides 41 & 43); Cardott, 2012 (Figure 10); Rottmann, 2000 |
| **Arkoma Basin** | |
| Sylvan Shale | Amsden, 1980 (Panel 1) |
| ***Woodford Shale*** | Amsden, 1980 (Panel 3); Blackford, 2007 (Plates 12 & 13); Rottmann, 2000 |
| Chattanooga Shale | Li et al., 2010 (Plates 4 & 6) |
| ***Fayetteville Shale*** | Ratchford et al., 2006 (Plates 2 & 3); Li et al., 2010 (Plates 3 & 5) |
| **Gulf Coast Basin** | |
| Wilcox Formation | Pitman, 2008 |
| ***Eagle Ford Shale*** | Surles, 1987 (Figures 5, 8, 9, 12, & 14); Pitman, 2008; Harbor, 2011 (Figure 8) (GIS data obtained from US Energy Information Administration) |
| ***Haynesville Shale*** | Hammes et al., 2011 (Figures 7 & 8) |
| Smackover Formation | Pitman, 2008 |
| **Fort Worth Basin** | |
| ***Barnett Shale*** | Pollastro et al., 2007 (Figures 6 & 15) |
| **Permian Basin** | |
| ***Woodford Shale*** | Broadhead, 2010 (Figures 4 & 12); Comer, 1991 (Plates 1 & 2); Ruppel et al., 2005 (GIS data obtained from University of Texas, Bureau of Economic Geology) |
| ***Barnett Shale*** | Broadhead and Gillard, 2007 (Plates V and VII) (GIS data obtained from New Mexico Bureau of Geology and Mineral |

| | |
|---|---|
| | Resources) |
| **Williston Basin** | |
| ***Bakken Shale*** | LeFever, 2008 (Sheets 1 & 5); LeFever et al., 2012 (GIS data obtained from North Dakota Geological Survey) |
| Big Snowy Group | Peterson, 1984 (Figure 12) |
| ***Pierre (Bearpaw) Shale*** | Schurr, 1977 (Figures 5 & 6); Carlson, 1982; Smith, 1999; Condon, 2000 (Plates 8 & 23) |
| **Powder River Basin** | |
| ***Pierre Shale*** | Schurr, 1977 (Figures 5 & 6); Denson et al., 1993a, b, c, d |
| Lebo shale member, Fort Union Formation | Lewis and Hotchkiss, 1981 (Plate 3) |
| Upper Hell Creek confining layer, Lance Formation | Lewis and Hotchkiss, 1981 (Plate 5) |
| **Denver Basin** | |
| ***Pierre Shale*** | Schurr, 1977 (Figures 5 & 6); Dechesne et al., 2011 (Plates 4 & 8) |
| **San Juan Basin** | |
| ***Mancos Shale*** | Ridgley et al., 2013 (Figures 6 & 10) |
| **Green River Basin** | |
| ***Green River Formation*** | Mercier et al., 2010c |
| **Piceance Basin** | |
| ***Green River Formation*** | Mercier et al., 2010a; Mercier and Johnson, 2012 |
| **Uinta Basin** | |
| ***Green River Formation*** | Mercier et al., 2010b; Mercier and Johnson, 2012 |
| **Cuyama Basin** | |
| ***Monterey Formation*** | Lagoe, 1982 (Plate VI); 1984 (Figure 11); Sweetkind et al., 2013 (GIS data obtained from US Geological Survey) |
| **Santa Maria Basin** | |
| ***Monterey Formation*** | Sweetkind et al., 2010 (GIS data obtained from US Geological Survey) |
| **San Joaquin Basin** | |
| Monterey Formation | Hosford Scheirer, 2013 (Figure 7.18) |

### 2.3.1 Appalachian Basin

The Appalachian Basin is a composite foreland basin that contains a thick sequence of Paleozoic sedimentary rocks (Ettensohn, 2008). These rocks have been subjected to a number of orogenic events, resulting in faulting and folding. The Marcellus Shale has been the primary focus for numerous geologic studies (e.g., Lash and Engelder, 2011) because of its prolific shale gas resources.

GIS data were obtained for two major shale formations in this basin: the Ordovician Utica Shale and the Devonian Marcellus Shale, both major shale gas targets. The Utica Shale GIS dataset was developed as part of a comprehensive regional stratigraphic study conducted by the Trenton-Black River Research Consortium of the Ordovician Trenton-Black River carbonate system (Patchen et al., 2006). This study generated an interval-thickness map for the Utica Shale and a structural map for the top of the Trenton Limestone, which serves at the base of the Utica Shale. GIS data obtained from the West Virginia Geological and Economic Survey were used to generate isopach and structure maps for the Utica Shale (Figure 2-2).

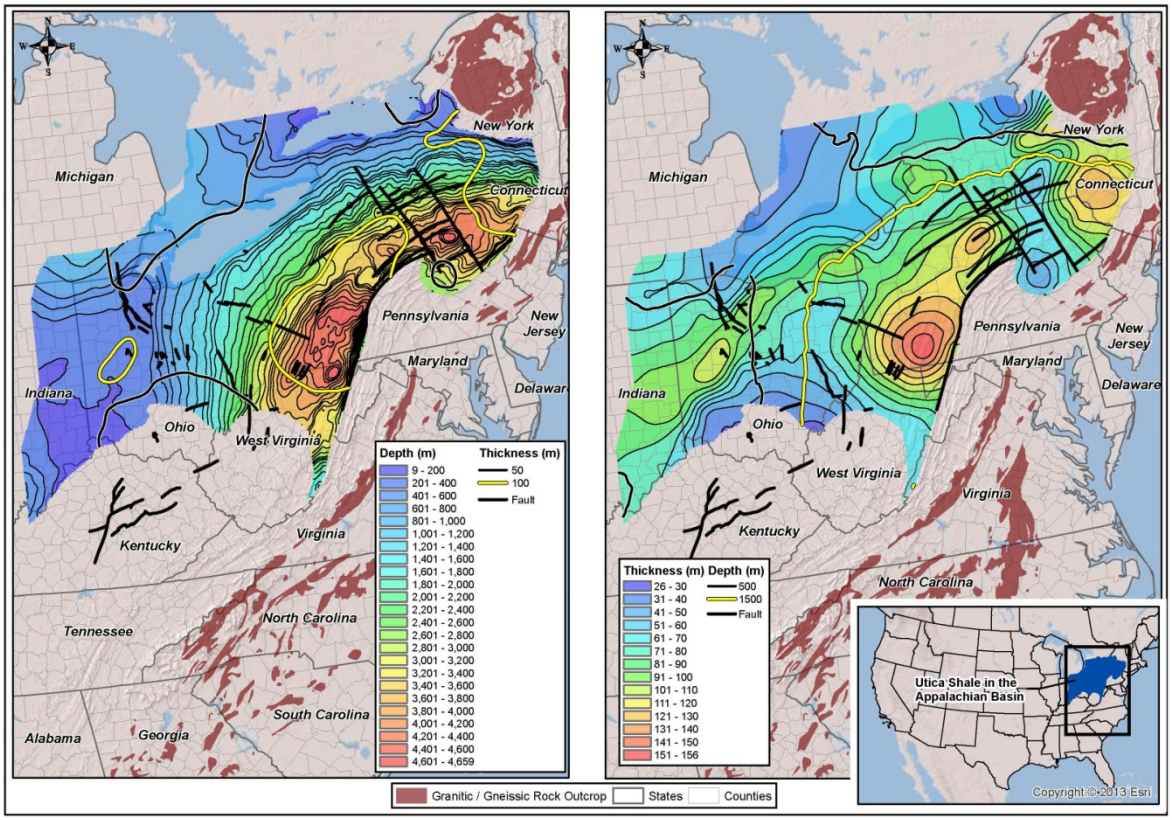


Figure 2-2. Depth and isopach maps of the Utica Shale, Appalachian Basin. Figure produced by LANL from shale data populated into the GIS database.

GIS data obtained from the Ohio Department of Natural Resources were used to generate isopach and structure maps for the Marcellus Shale (Figure 2-3). This unit has a total area of 95,000 square miles (EIA, 2011). While this unit is very extensive, and is present in Ohio, Pennsylvania, West Virginia, Virginia, western Maryland and New York, there is only a limited area (in eastern Pennsylvania) where the shale thickness is at least 100 m at depths less than 1000 m.

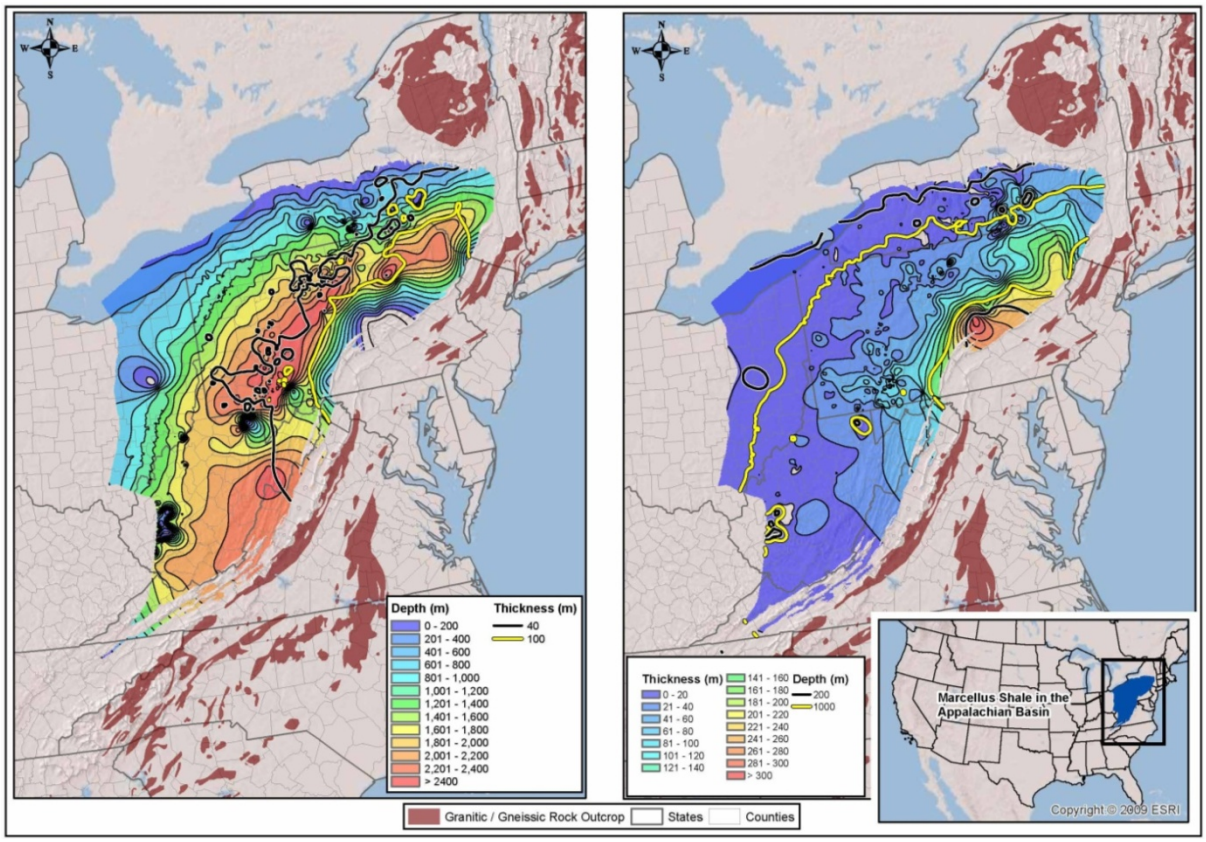


Figure 2-3. Depth and isopach maps of the Marcellus Shale, Appalachian Basin. Figure produced by LANL from shale data populated into the GIS database.

Structural top and isopach maps were also obtained for a number of additional Devonian black shale units in Ohio: the Chagrin, Cleveland and Huron members of the Ohio Shale and the Upper and Lower Olentangy Shales (Gray et al., 1982). The Ohio Shale is equivalent in age to the Chattanooga Shale, the New Albany Shale in the Illinois Basin and the Antrim Shale in the Michigan Basin (Gonzales and Johnson, 1985).

The compositions and rock properties of the Utica and Marcellus shales were evaluated in an analog assessment of their viability as a rock barrier for the migration of radionuclides as part of an evaluation of the proposed Ontario Power Generation Deep Geologic Repository at the Bruce site in Ontario for storage of low and intermediate radioactive waste (Engelder, 2011). High natural gas contents related to the burial and maturation of organic-rich shales can lead to the

development of natural hydraulic fractures, which could compromise the integrity of the shales as fluid flow barriers. The Utica Shale has a total organic carbon (TOC) content that varies from 0.28 to 4.26 wt. % (Figure 2-4), with a median value just less than 2% (Ryder et al., 1998). In contrast, the Marcellus has TOC values that generally range from 2 to 12 wt. %, with values typically between 2 and 10% (Bruner and Smosna, 2011). Organic-rich black shales are often characterized by elevated gamma signatures. Agrawal (2009) describes the depositional environment, mineralogy and TOC of the Marcellus.

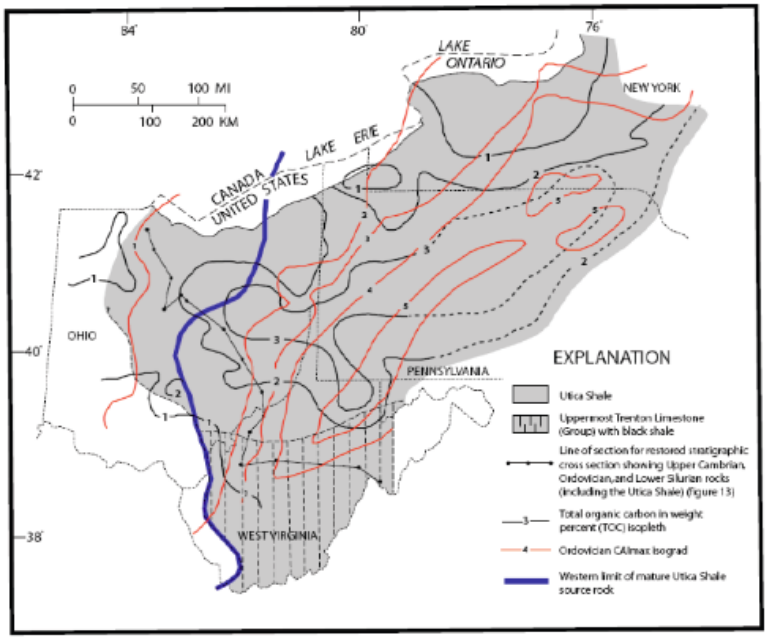


Figure 2-4. Variation in total organic carbon in the Utica Shale (Engelder, 2011)

### 2.3.2 Black Warrior Basin

The Black Warrior Basin is a Paleozoic foreland basin located in Alabama and Mississippi (Thomas, 1988). It has three major shale formations: the Devonian Chattanooga Shale, the Mississippian Floyd Shale, and shale layers in the Pennsylvanian Pottsville Formation (Pawlewicz and Hatch, 2007). These shales have been identified as the source rocks for oil and gas deposits in the basin. Pashin (2008) has created an isopach map within the state of Alabama for the Chattanooga Shale (Figure 2-5). Almost all of the mapped section of the Chattanooga in this basin has a thickness less than 30 m.

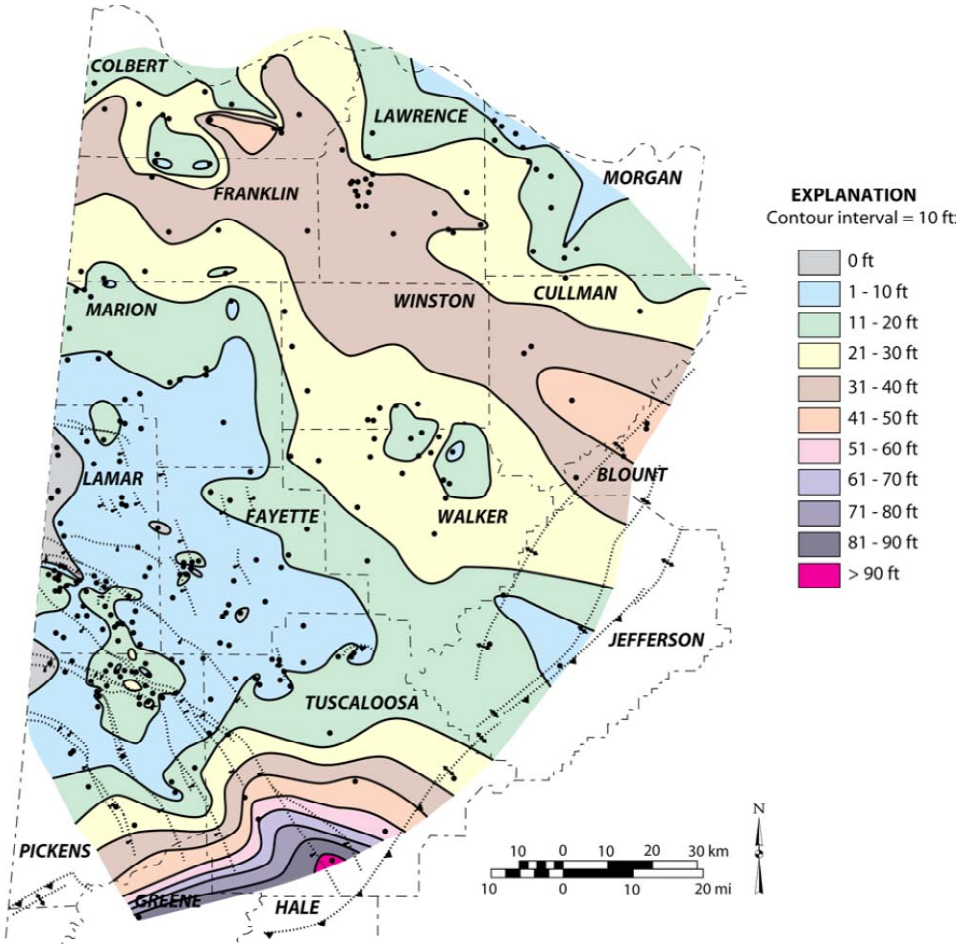


Figure 2-5. Isopach map of the Chattanooga Shale within the Alabama portion of the Black Warrior Basin (Pashin, 2008)

### 2.3.3 Illinois Basin

The Illinois Basin is filled primarily with Paleozoic age rocks, consisting of interbedded siliciclastic and carbonate sediments (Collinson et al., 1988; Swezey, 2009). The Devonian to Mississippian New Albany Shale is the most prominent shale unit in the Illinois Basin, with an areal extent of about 43,500 square miles and a thickness of 100 to 300 ft (Hasenmueller and Comer, 1994; EIA, 2011). GIS data for this unit (Figure 2-6) is available over the entire basin (Hasenmueller and Comer, 2000). In the southern portion of the Illinois Basin, there is a small section of this unit with thicknesses greater than 100 m at a depth of less than 1000 m.

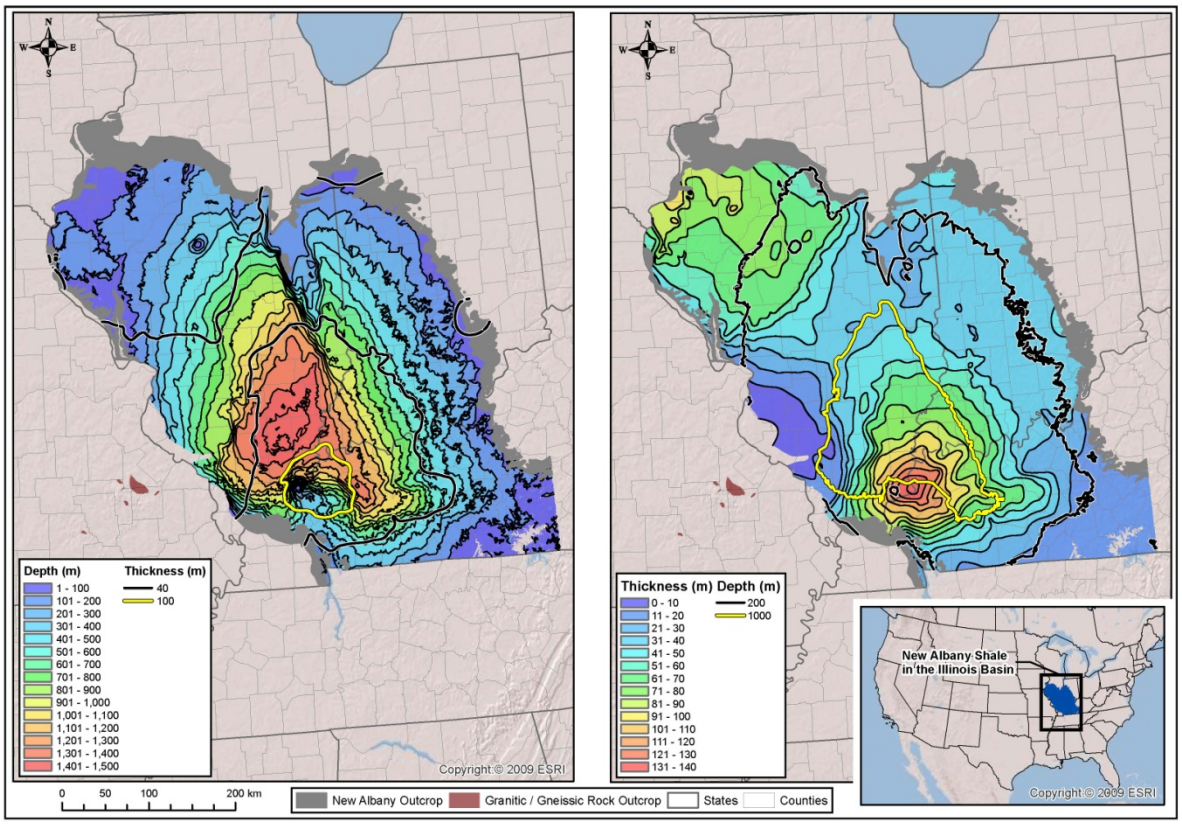


Figure 2-6. Depth and isopach maps of the New Albany Shale, Illinois Basin. Figure produced by LANL from shale data populated into the GIS database.

There are a number of studies with thickness and/or structural depth information on the Ordovician Maquoketa Shale. Bristol and Buschbach (1973) provide a plate depicting the top of the Galena Group, which represents the base of the Maquoketa Shale, for the state of Illinois. Willman et al. (1975) present a figure depicting the thickness of the Maquoketa Group, also restricted to Illinois. Collinson et al. (1988) and Kolata and Noger (1990) provide more regional depictions of the thickness of this unit. Given that this unit is older than the New Albany Shale, it is encountered at greater depths. The Illinois state data (Bristol and Buschbach (1973) and Willman et al. (1975)) were used to generate GIS maps of this unit (Figure 2-7).

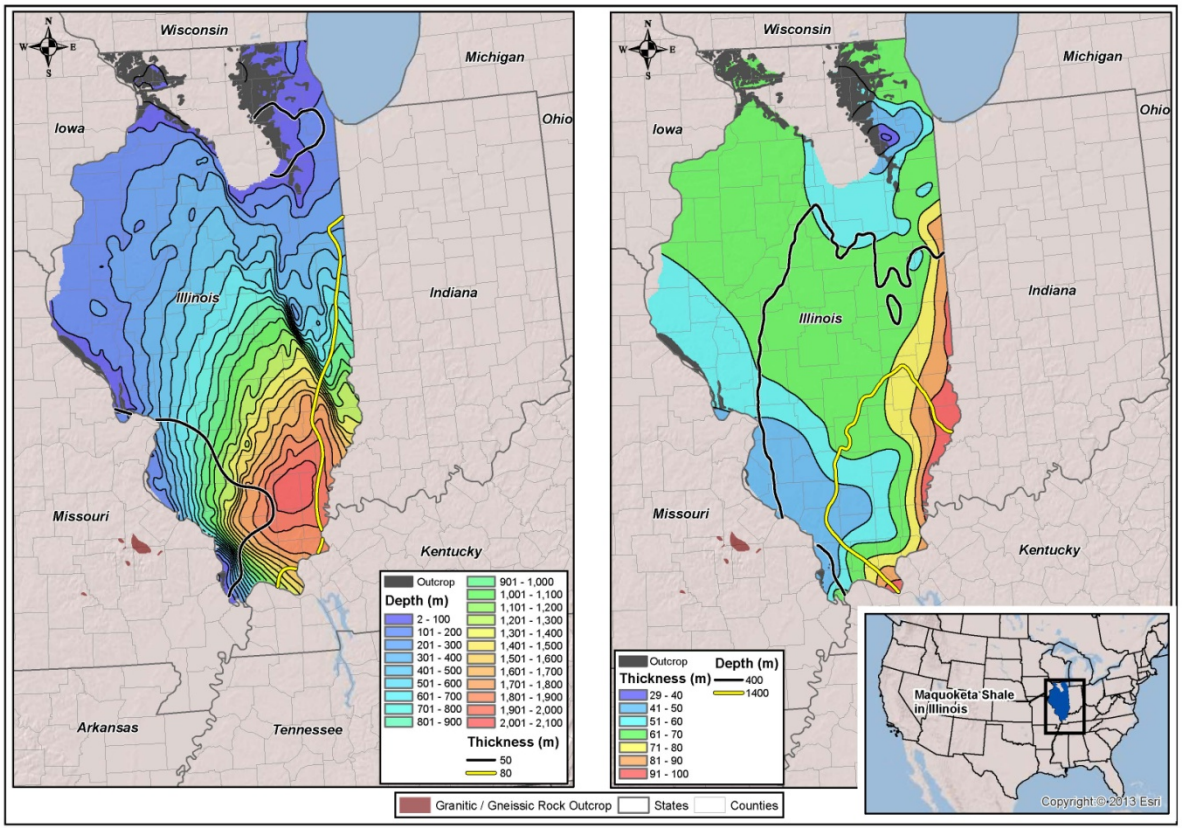


Figure 2-7. Depth and isopach maps of the Maquoketa Shale, Illinois Basin. Figure produced by LANL from shale data populated into the GIS database.

### 2.3.4 Michigan Basin

The Michigan Basin has a thick sequence of Paleozoic evaporites, carbonates, and siliciclastic sedimentary rocks (e.g., Merewether et al., 1973; Catacosinos et al., 1991; Swezey, 2008). Shale formations found in this basin include the Ordovician Utica and Collingwood Shales, the Silurian Cabot Head and Pointe aux Chenes Shales, the Devonian Antrim, Ellsworth, and Bedford Shales and the Mississippian Sunbury and Coldwater Shales. The predominant shale formation in the Michigan Basin is the Antrim Shale, a major producer of natural gas, with estimated recoverable shale gas resources of 20 trillion cubic feet (EIA, 2011). Wylie and Wood (2004; 2005) generated GIS structure and isopach maps for a number of the hydrocarbon producing units in the Michigan Basin, including the Antrim Shale (Figure 2-8). Agrawal (2009) describes the depositional environment, mineralogy and TOC of the Antrim. GIS data were generated for the Coldwater Shale (Figure 2-9) using the isopach and structure map of Gonzales and Johnson (1985).

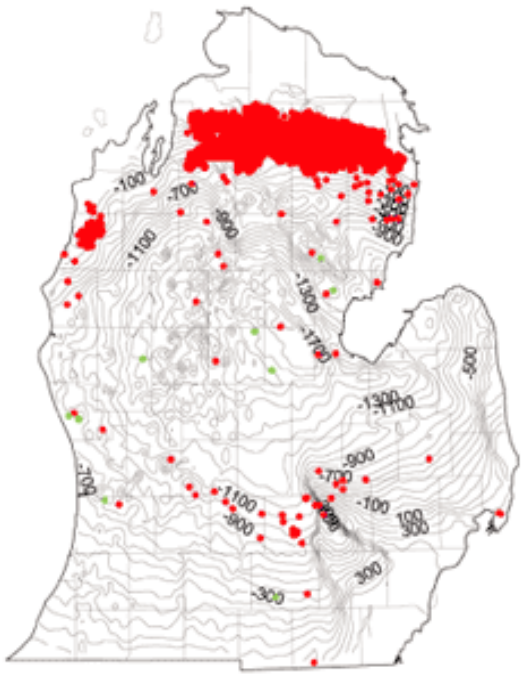


Figure 2-8. Structure map of the Antrim Shale, Michigan Basin (Wylie and Wood, 2005). Gas wells are depicted as red dots.

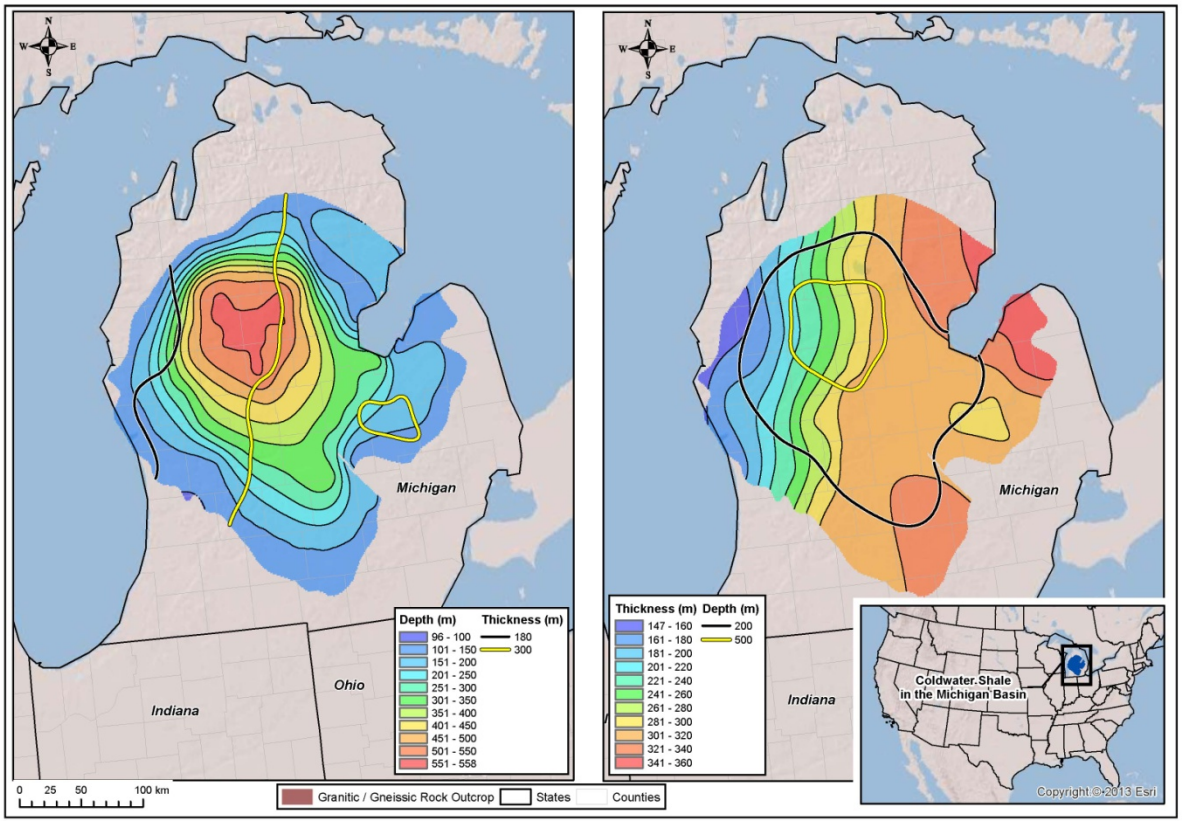


Figure 2-9. Depth and isopach maps of the Coldwater Shale, Michigan Basin. Figure produced by LANL from shale data populated into the GIS database.

### 2.3.5 Anadarko, Ardmore, and Arkoma Basins

The Anadarko, Ardmore, and Arkoma Basins, located in Oklahoma and neighboring states, are a series of fault-bounded sedimentary basins containing abundant hydrocarbon deposits. Detailed structure and isopach maps have been published for a number of the shale-bearing formations in these basins, including the Cretaceous Kiowa Formation and Graneros Shale (Macfarlane et al., 1993), the Mississippian Fayetteville Shale (Ratchford et al., 2006; Li et al., 2010), the upper Devonian/lower Mississippian Woodford Shale (e.g., Amsden, 1975; 1980; Cardott and Lambert, 1985; Rottmann, 2000; Blackford, 2007; Party et al., 2008; Cardott, 2012) and the Ordovician Sylvan Shale (Amsden, 1975).

The Hugoton Embayment of the Anadarko Basin in southwestern Kansas contains a sequence of Paleozoic, Mesozoic, and Cenozoic sedimentary rocks that reaches up to 2900 m in thickness (Macfarlane et al., 1993). In the upper portion of this basin, there are several Cretaceous shale units, including the Kiowa Formation (Figure 2-10) and the Graneros Shale (Figure 2-11), which serve as regional aquitards.

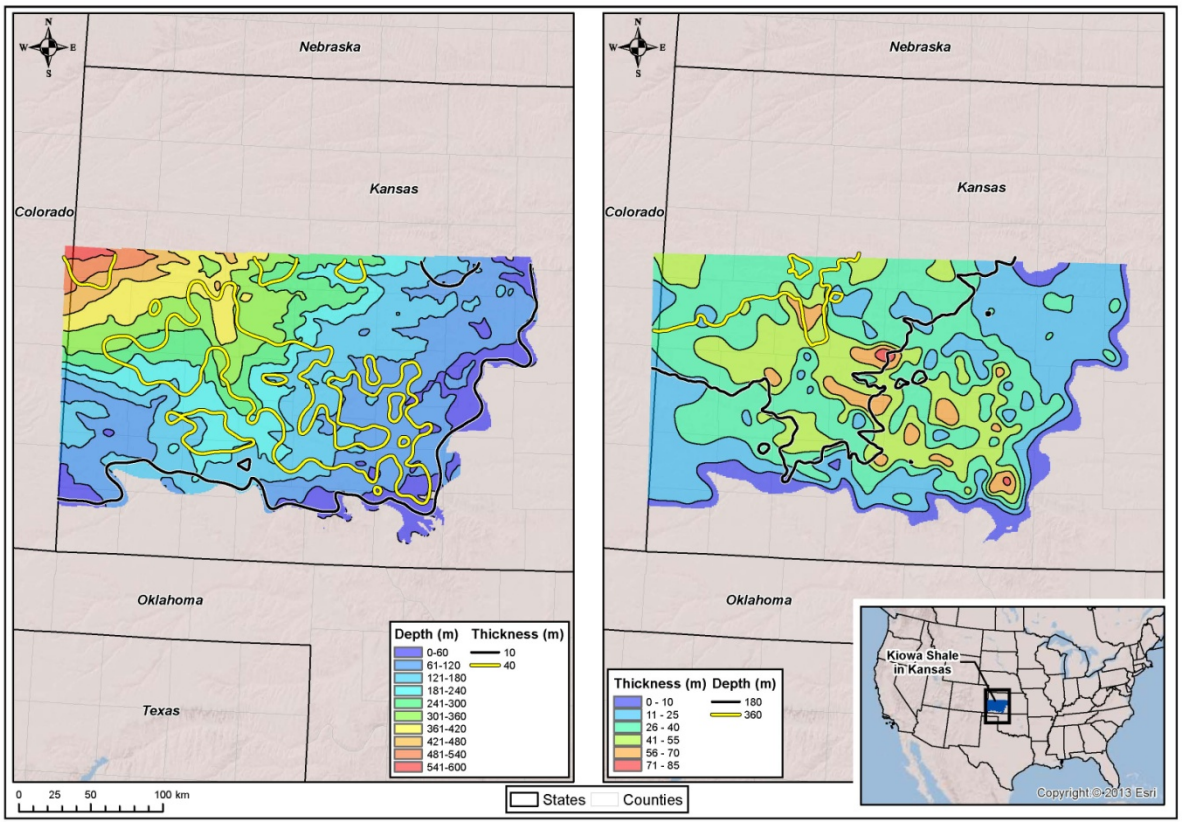


Figure 2-10. Depth and isopach maps of the Kiowa Shale, Anadarko Basin. Figure produced by LANL from shale data populated into the GIS database.

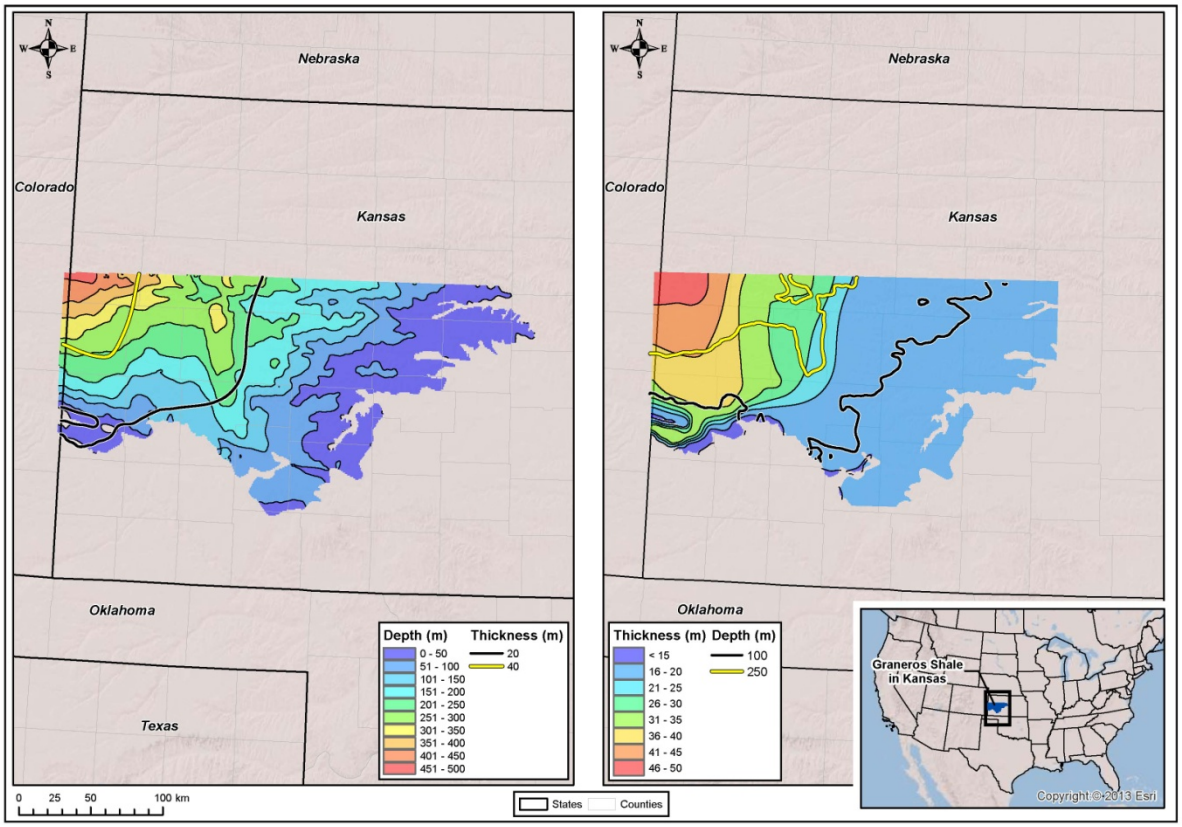


Figure 2-11. Depth and isopach maps of the Graneros Shale, Anadarko Basin. Figure produced by LANL from shale data populated into the GIS database.

Data on the Mississippian Fayetteville Shale reported by Ratchford et al. (2006) and Li et al. (2010) were used to construct structure and isopach maps for this unit in the Arkoma Basin in Arkansas (Figure 2-12). These studies also contain extensive geochemical data on the total organic carbon (TOC) and vitrinite reflectance of the shale in this basin.

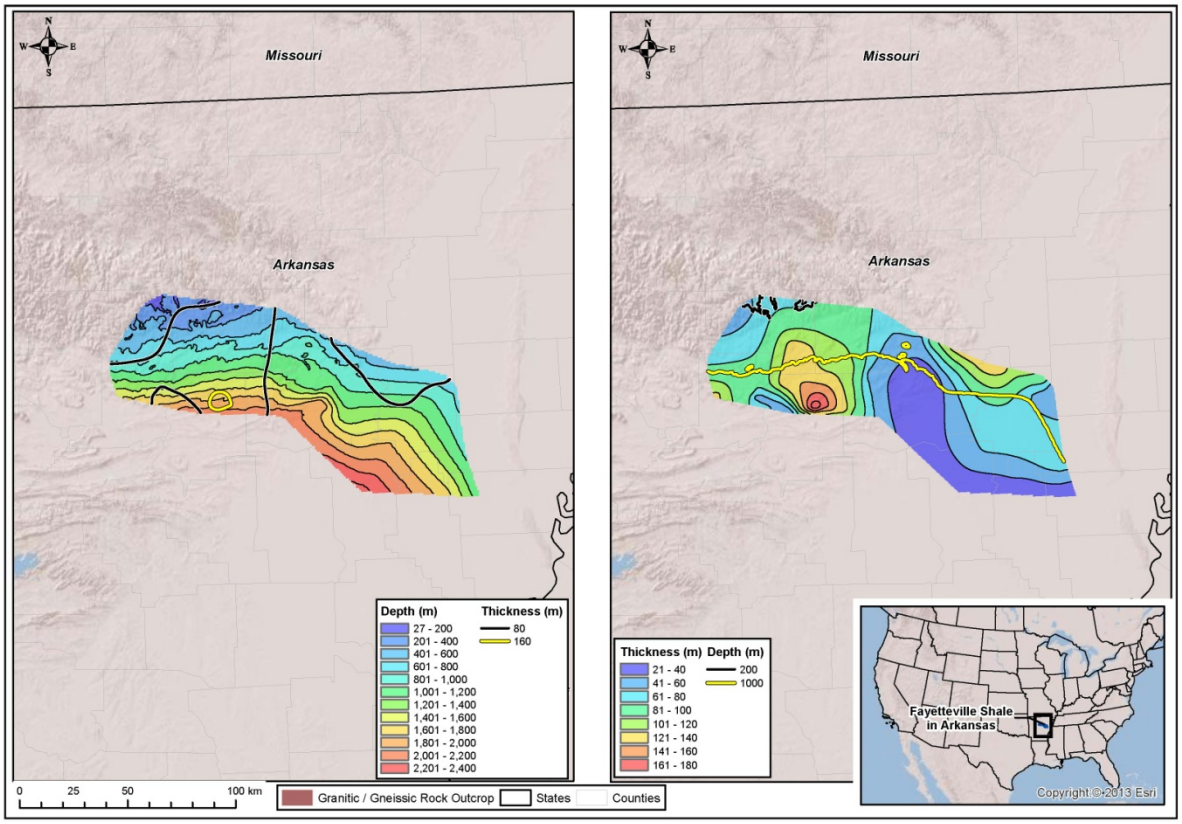


Figure 2-12. Depth and isopach maps of the Fayetteville Shale, Arkoma Basin. Figure produced by LANL from shale data populated into the GIS database.

The Upper Devonian/Lower Mississippian Woodford Shale (e.g., Amsden, 1975; 1980; Cardott and Lambert, 1985; Rottmann, 2000; Blackford, 2007; Party et al., 2008; Cardott, 2012) is a major shale gas play and hydrocarbon source rock in Oklahoma. Agrawal (2009) describes the depositional environment, mineralogy and TOC of the Woodford. GIS data for the Woodford Shale within the Anadarko and Arkoma Basins were generated from Amsden (1975; 1980) (Figure 2-13).

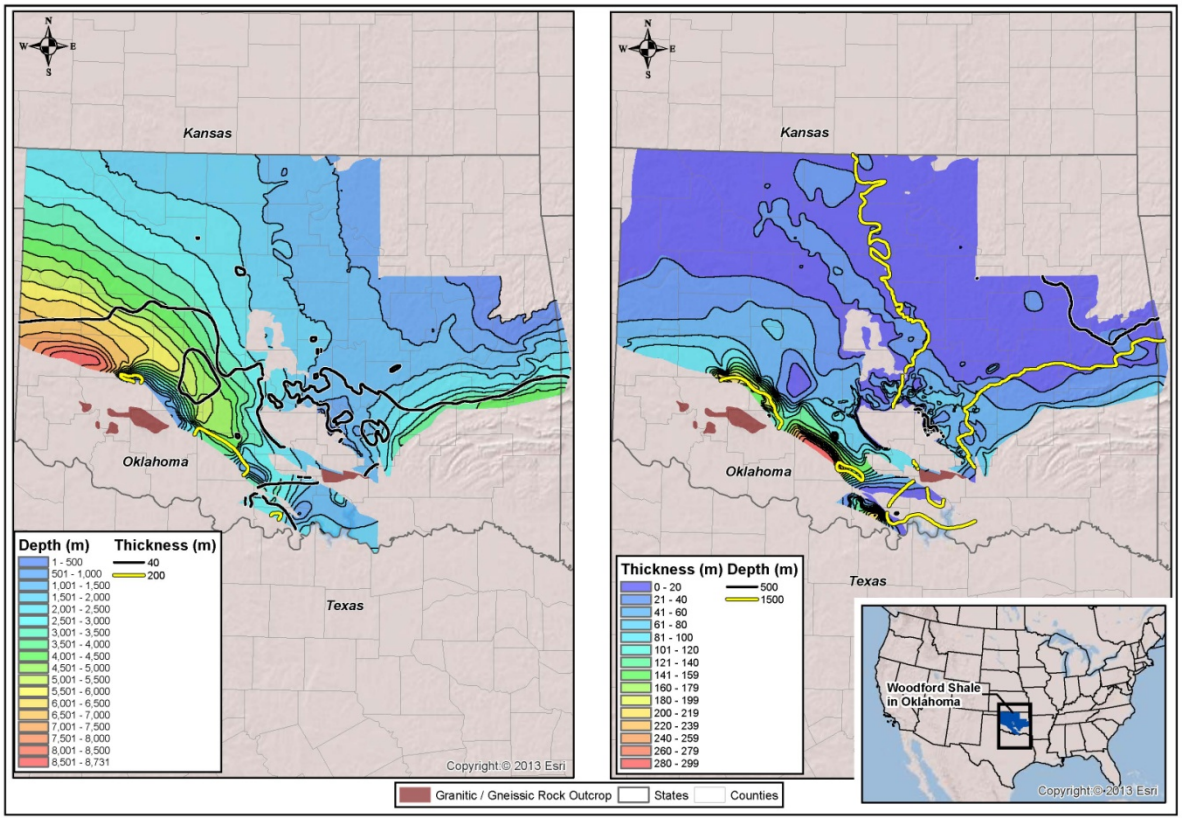


Figure 2-13. Depth and isopach maps of the Woodford Shale, Anadarko and Arkoma Basins. Figure produced by LANL from shale data populated into the GIS database.

### 2.3.6 Gulf of Mexico Basin

The Gulf of Mexico Basin contains extensive sedimentary accumulations both onshore and offshore, many of which host hydrocarbon deposits. Pitman (2008) generated a comprehensive GIS database of petroleum reservoirs and associated source rocks in Gulf of Mexico Basin, including delineation of the Upper Jurassic Smackover Formation, the Upper Cretaceous Eagle Ford Formation, and the Paleocene/Eocene Wilcox Formation. Hammes et al. (2011) presented a detailed description of the regional geology and stratigraphy of the Upper Jurassic Haynesville Shale, including isopach and structure maps of this important shale gas play unit; these maps were digitized to generate GIS data to create depth and isopach maps for this unit (Figure 2-14). Agrawal (2009) describes the depositional environment, mineralogy and TOC of the Haynesville. Surles (1987) constructed isopach maps for the entire Eagle Ford shale and its members, as well as compiled information on the amount of sand and organic matter. Harbor (2011) conducted a detailed study of the lithofacies and stratigraphy of the Eagle Ford Formation. GIS data obtained from the US EIA (EIA, 2010) was used to construct depth and isopach maps for the Eagle Ford Formation (Figure 2-15).

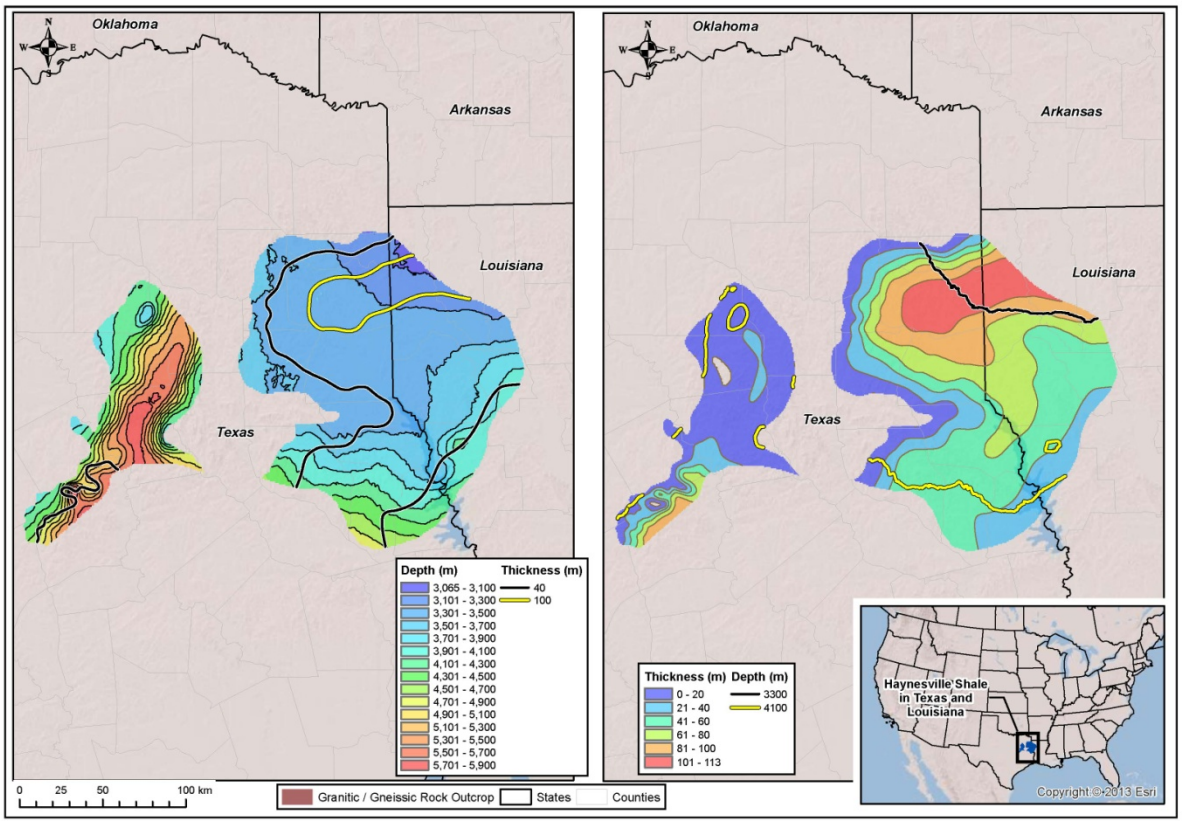


Figure 2-14. Depth and isopach maps of the Haynesville Shale, Gulf of Mexico Basin. Figure produced by LANL from shale data populated into the GIS database.

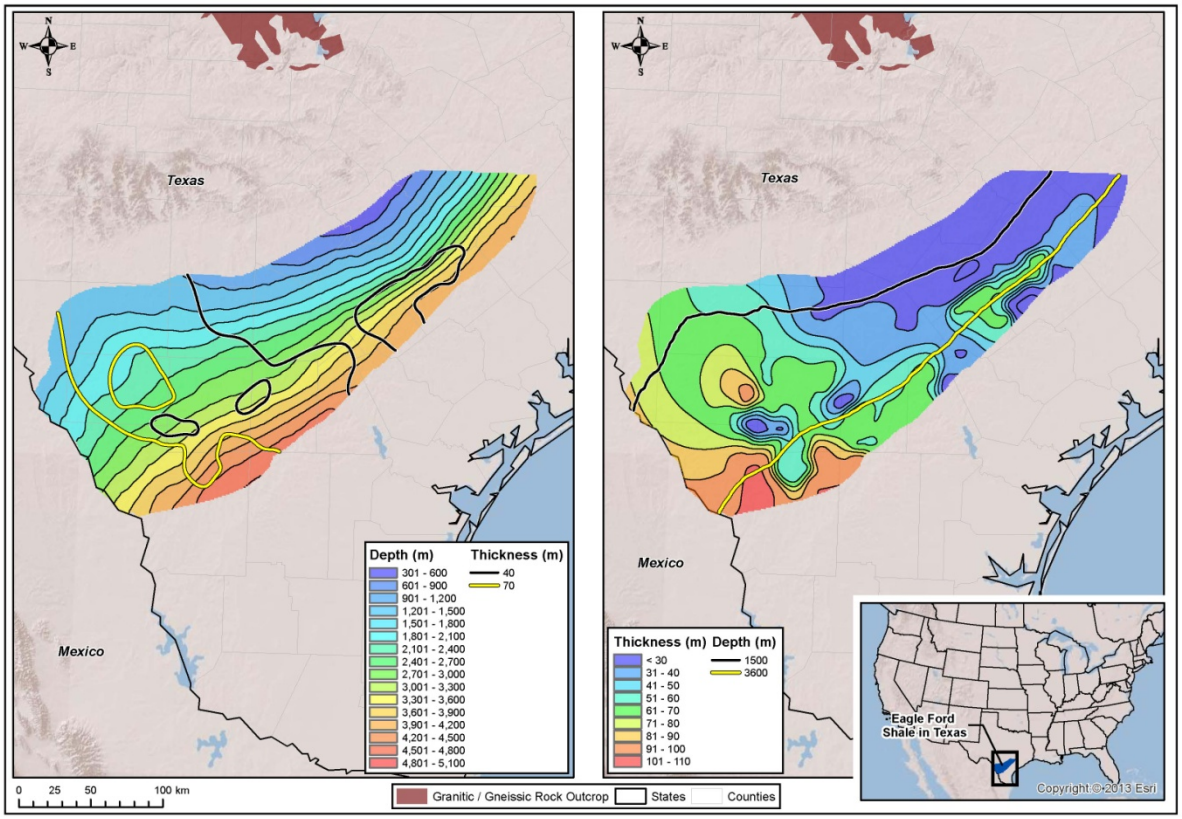


Figure 2-15. Depth and isopach maps of the Eagle Ford Formation, Gulf of Mexico Basin. Figure produced by LANL from shale data populated into the GIS database.

### 2.3.7 Fort Worth Basin

The Mississippian Barnett Shale is a major producer of shale gas in the Fort Worth Basin. Pollastro et al. (2007) conducted a detailed geologic study of this petroleum system, and generated isopach and structure maps for the Barnett Shale; these maps were digitized and integrated into the LANL GIS database (Figure 2-16). Agrawal (2009) describes the depositional environment, mineralogy and TOC of the Barnett.

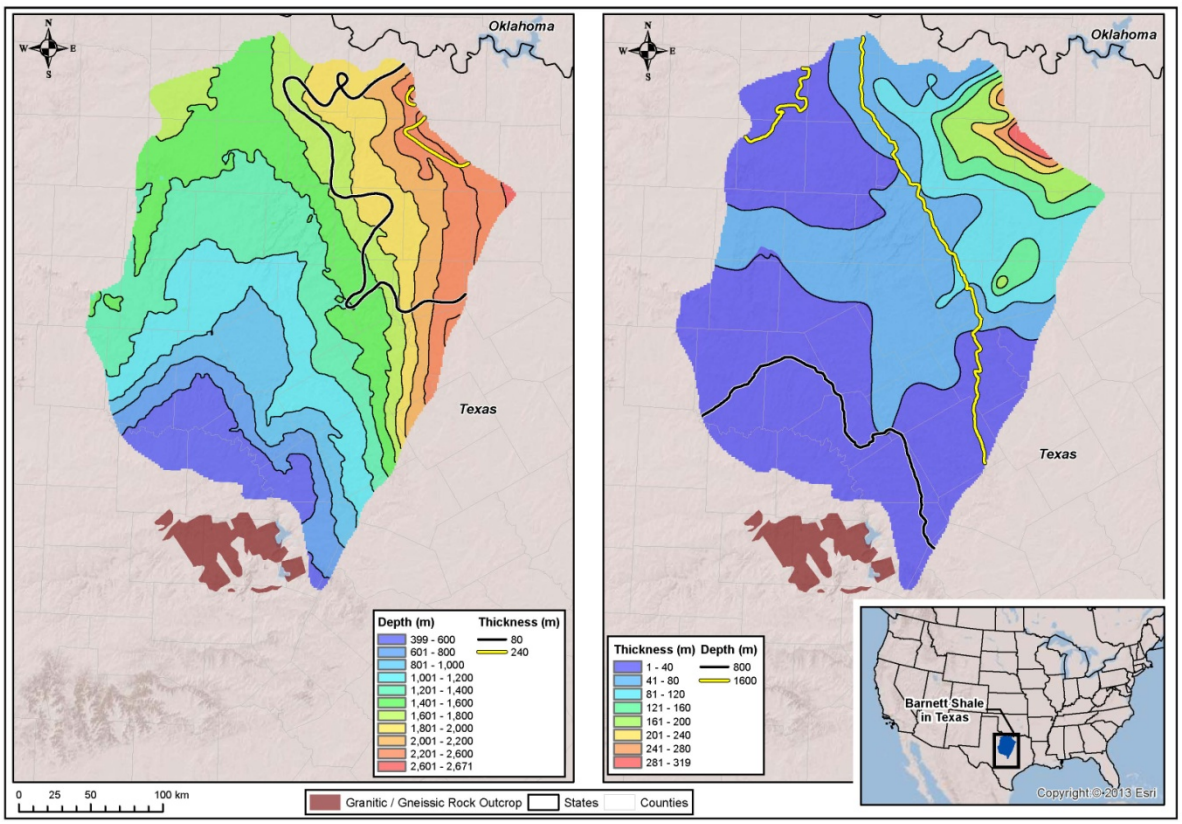


Figure 2-16. Depth and isopach maps of the Barnett Shale, Fort Worth Basin. Figure produced by LANL from shale data populated into the GIS database.

### 2.3.8 Permian Basin

While the Permian Basin is dominated by carbonate and evaporite sequences, it also hosts some siliciclastic units, such as the Woodford Shale. Broadhead (2010) conducted a detailed study of the distribution and source rock characteristics of the Woodford Shale located within the New Mexico portion of the Permian Basin. Structure and isopach maps for the Woodford Shale (Comer, 1991) were converted into GIS surfaces by Ruppel et al. (2005), and are depicted in Figure 2-17.

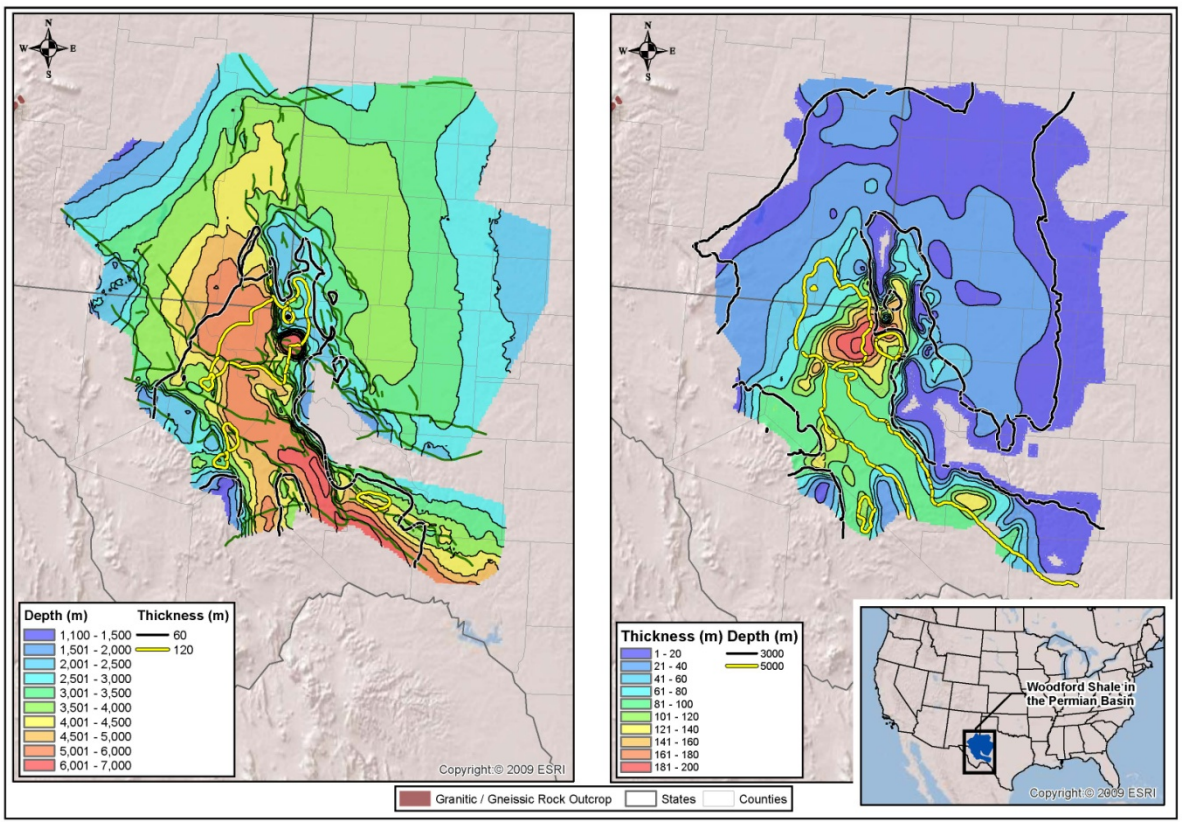


Figure 2-17. Depth and isopach maps of the Woodford Shale, Permian Basin. Figure produced by LANL from shale data populated into the GIS database.

Another major shale unit in the Permian Basin is the Mississippian Barnett Shale. Broadhead and Gillard (2007) provide detailed information on the stratigraphy, structure, and petroleum source rock characteristics, including TOC content and Rock-Eval data. Figure 2-18 depicts structural and isopach maps for the Barnett Shale in southeastern New Mexico (Broadhead and Gillard, 2007).

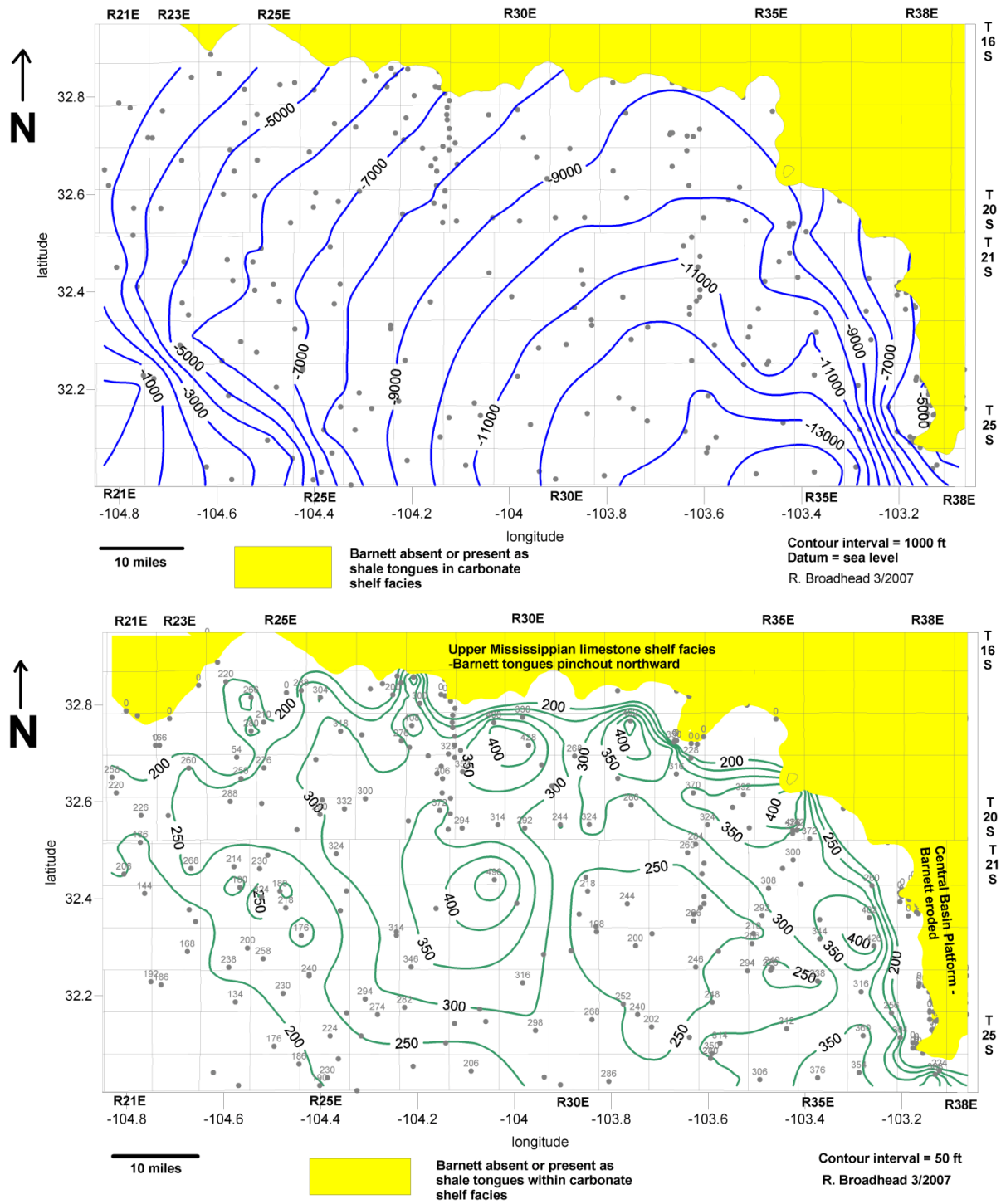


Figure 2-18. Depth (relative to sea level) and isopach maps of the Barnett Shale, Permian Basin (Broadhead and Gillard, 2007).

### 2.3.9 Williston Basin

The Williston Basin is an intercratonic basin centered in North Dakota with sedimentary rocks consisting of carbonates, evaporites, sandstones, and shales. These rocks range in age from Precambrian to Tertiary (Gerhard et al., 1982). Shale-bearing units within the Paleozoic section include the Ordovician Ice Box Formation and the Mississippian Bakken and Otter Formations. The Bakken Formation has upper and lower shale members and a middle sandstone member (Pollastro et al., 2008) and contains significant (3.59 billion barrels) reserves of oil shale (EIA, 2011). GIS data for the Bakken (Figure 2-19) are based on constraints provided by LeFever (2008) and LeFever et al. (2012).

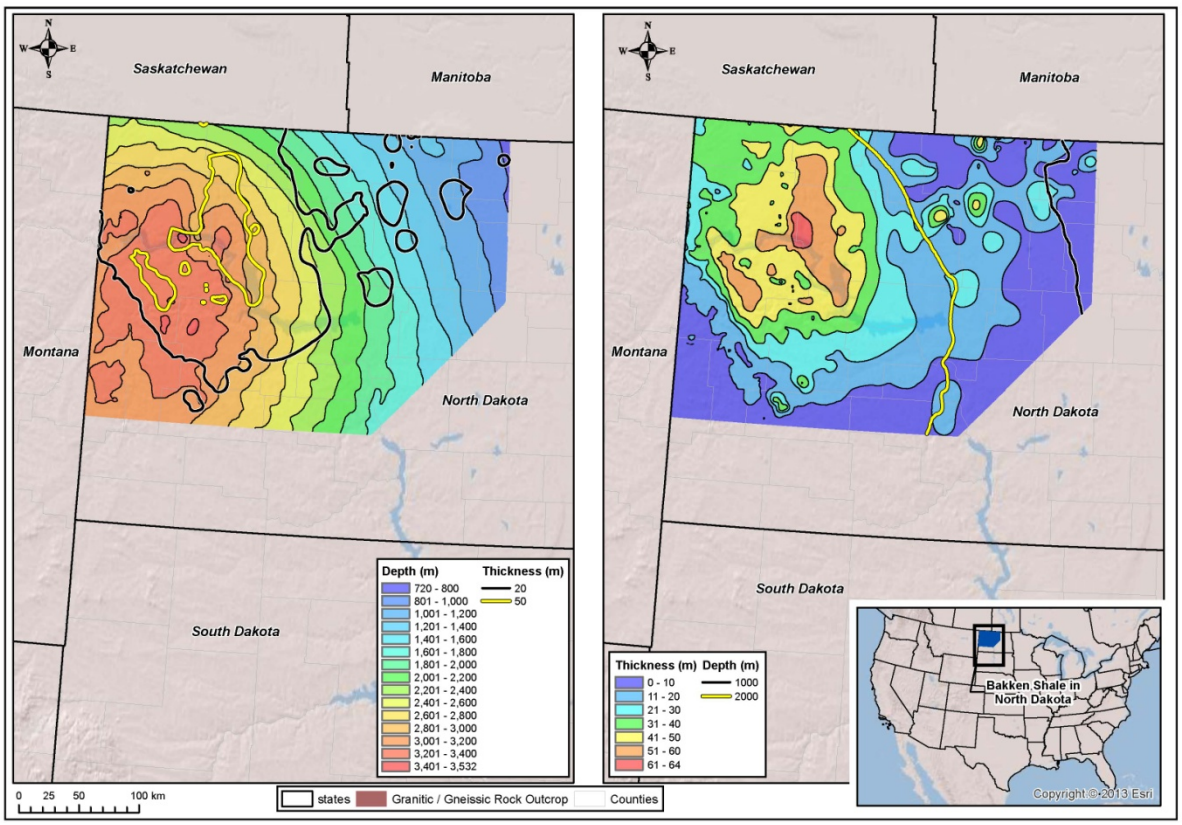


Figure 2-19. Depth and isopach maps of the Bakken Formation, Williston Basin. Figure produced by LANL from shale data populated into the GIS database.

The Williston Basin also contains a sequence of Cretaceous shales, including the Skull Creek, Mowry, Belle Fourche, Carlile, and Pierre (Bearpaw) Shales. There are a number of published isopach and structural maps of the Pierre Shale and its correlative unit, the Bearpaw, for this region (Shurr, 1977; Carlson, 1982; Smith, 1999; Condon, 2000); data from Condon (2000) for eastern Montana were used to generate GIS data for the Bearpaw (Figure 2-20).

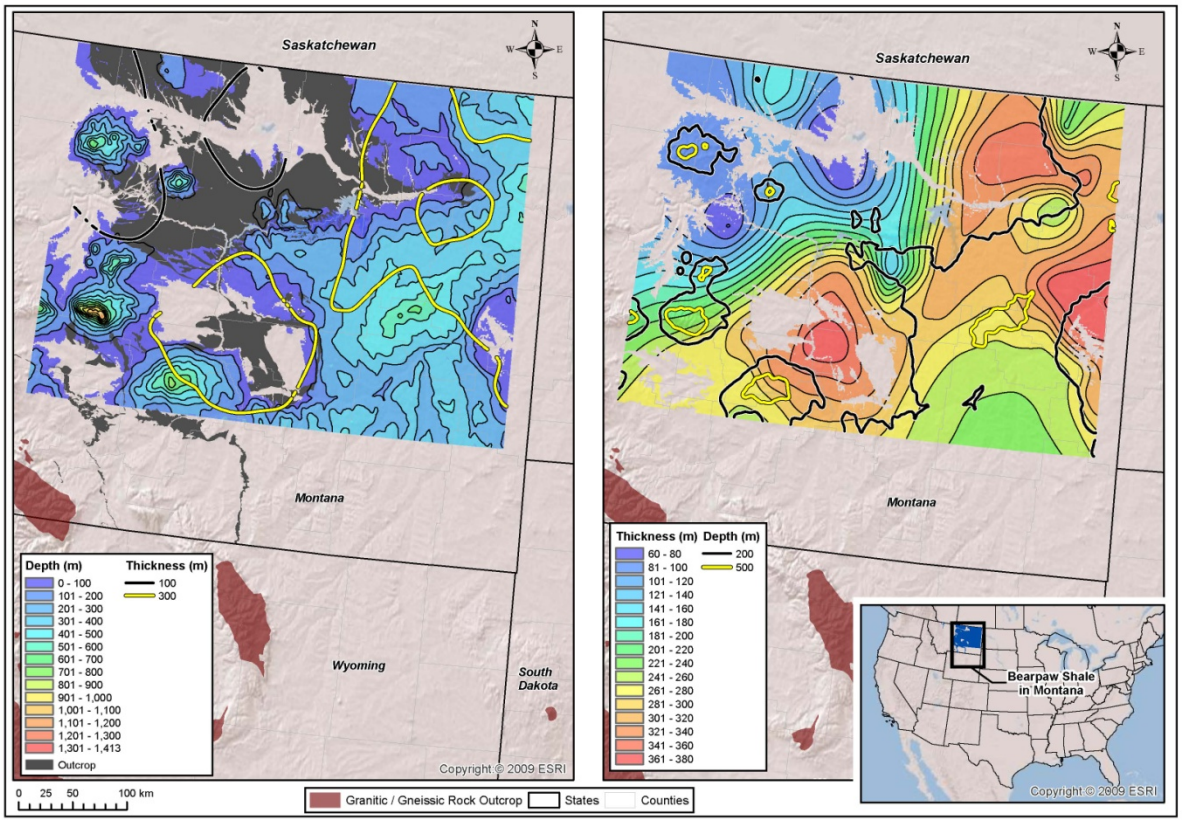


Figure 2-20. Depth and isopach maps of the Bearpaw Shale, Williston Basin. Figure produced by LANL from shale data populated into the GIS database.

### 2.3.10 Powder River Basin

The Powder River Basin contains a thick sequence of Paleozoic, Cretaceous, and Tertiary sediments (Anna, 2009), and is best known for its vast coal resources, consisting of thick deposits of subbituminous or lignite coal occurring at shallow depths. The Pierre Shale (Figure 2-21) forms part of the thick Cretaceous section of sediments (Denson et al., 1993a, b, c, d). As part of a hydrogeologic study of this basin, Lewis and Hotchkiss (1981) generated isopach and structure maps for the Lebo Shale member of the Paleocene Ft. Union Formation (Figure 2-22) and the Upper Hell Creek (or Lance) Formation, which is Upper Cretaceous in age.

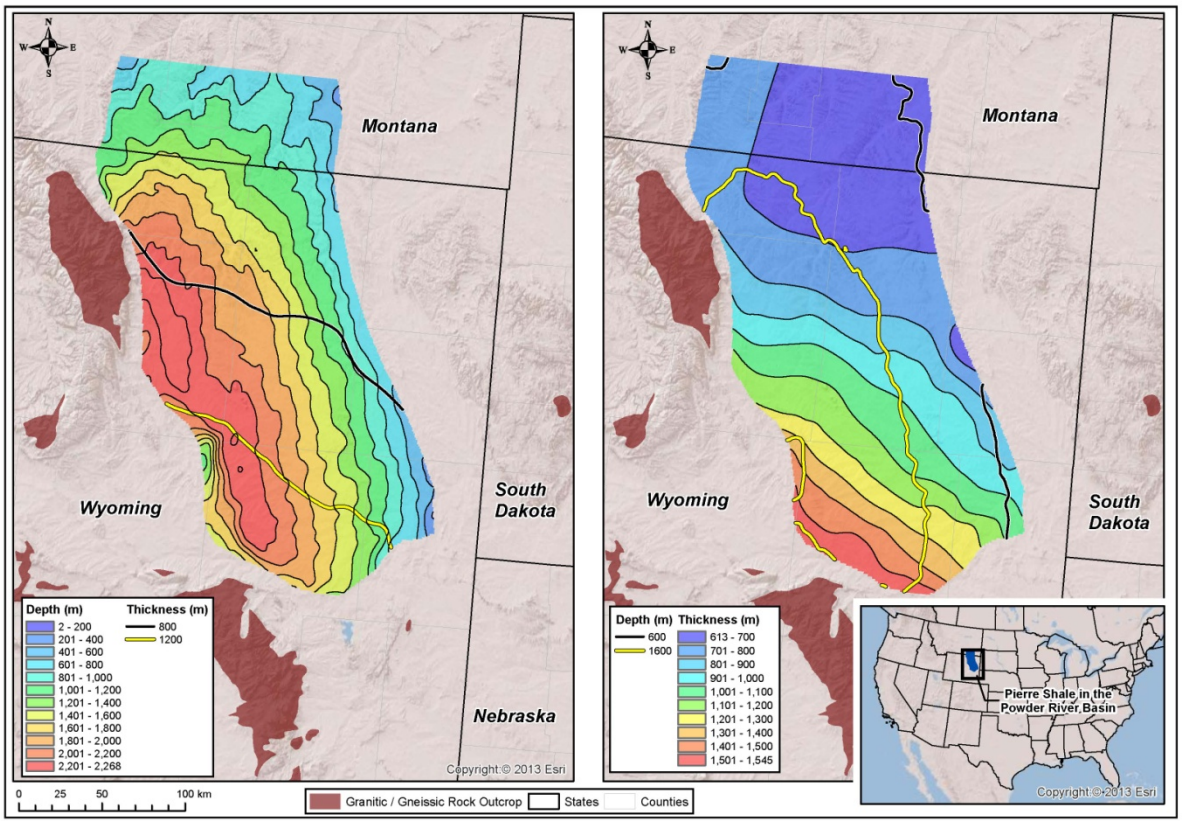


Figure 2-21. Depth and isopach maps of the Pierre Shale, Powder River Basin. Figure produced by LANL from shale data populated into the GIS database.

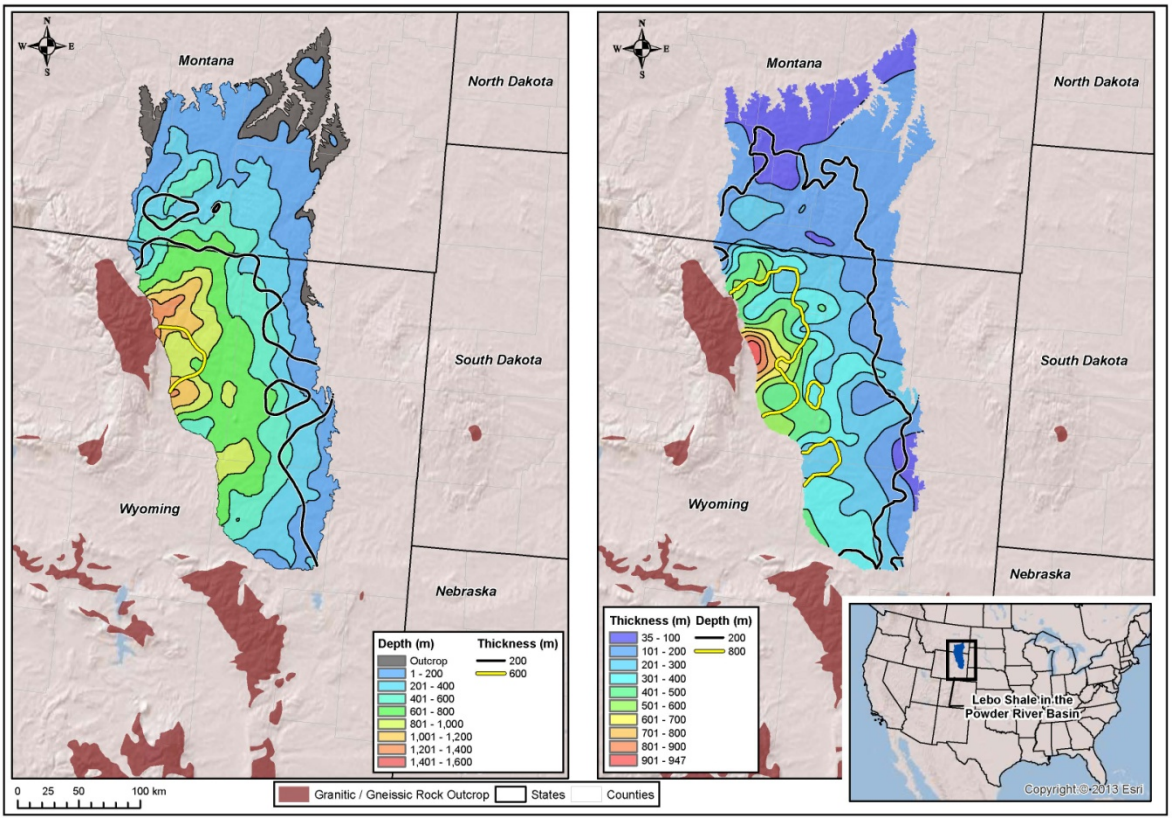


Figure 2-22. Depth and isopach maps of the Lebo Shale, Powder River Basin. Figure produced by LANL from shale data populated into the GIS database.

### 2.3.11 Denver Basin

The Denver Basin is a foreland structural basin bounded to the west by the Rocky Mountains. Most of the sediments in the basin are Cretaceous sandstones, shales, and carbonates (Higley and Cox, 2007); the shale units include the Skull Creek, Mowry, Graneros, Carlile, Niobrara (Smoky Hills Shale Member), and Pierre. The Pierre Shale is the most prominent of these units, and its distribution and thickness (Figure 2-23) has been characterized by Shurr (1977), who conducted an extensive study of this unit as a possible host for radioactive waste, and Dechesne et al. (2011).

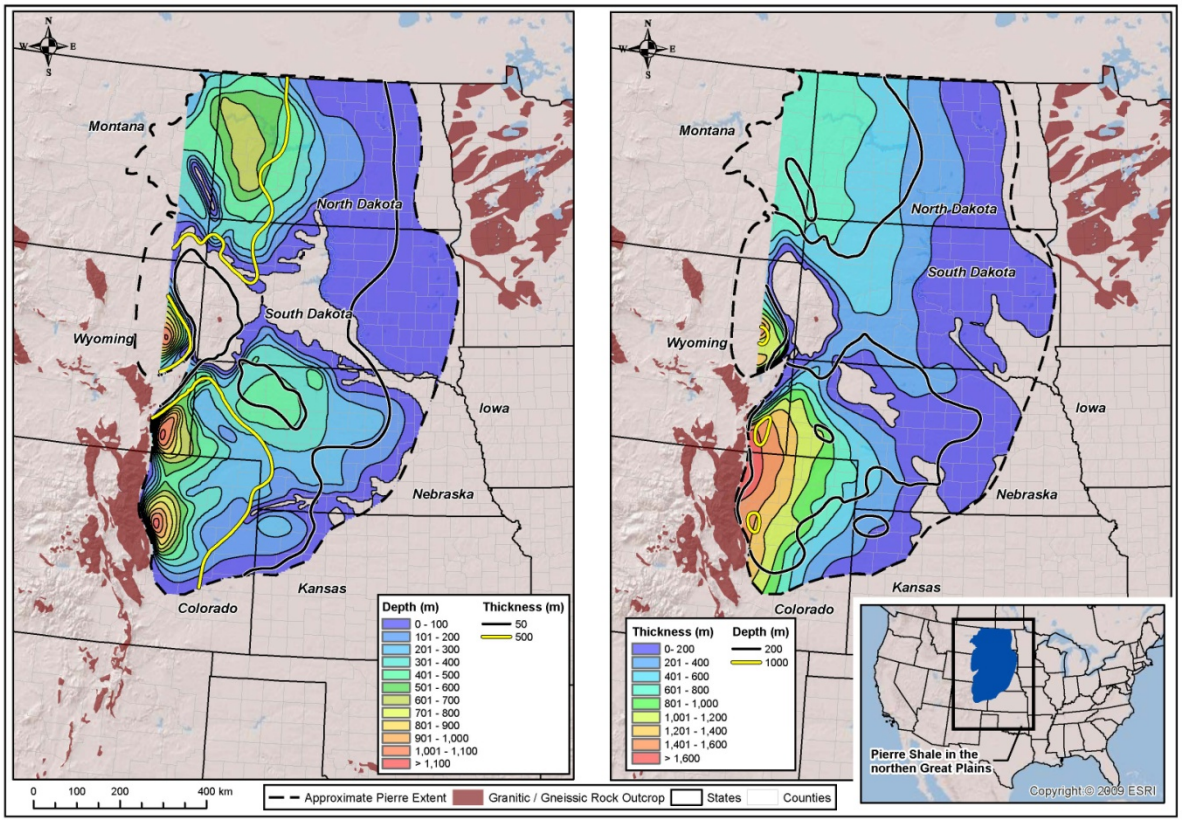


Figure 2-23. Depth and isopach maps of the Pierre Shale in the Williston and Denver Basins. Figure produced by LANL from shale data populated into the GIS database.

### 2.3.12 San Juan Basin

The San Juan Basin is located in southwestern Colorado and northwestern New Mexico. It contains a thick section of Jurassic and Cretaceous sands and shales, including the Upper Cretaceous Mancos Shale (Ridgley et al., 2013). This unit ranges in thickness from less than 30 m up to more than 600 m within the San Juan Basin, and is a source rock for hydrocarbon production in the basin. Isopach and structure maps from Ridgley et al. (2013) were used to develop GIS data for the Mancos in this basin (Figure 2-24).

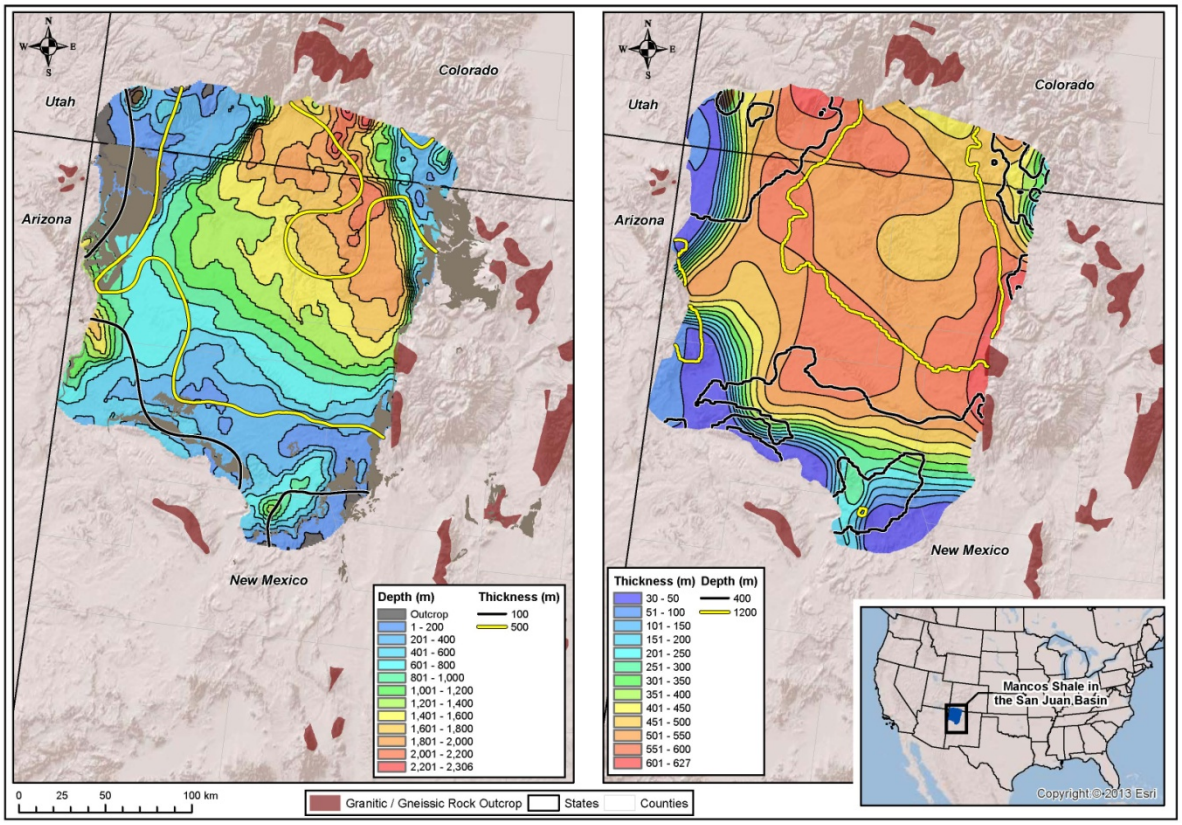


Figure 2-24. Depth and isopach maps of the Mancos Shale in the San Juan Basin. Figure produced by LANL from shale data populated into the GIS database.

### 2.3.13 Green River, Piceance, and Uinta Basins

The Greater Green River, Piceance, and Uinta Basins are located in Wyoming, Utah and Colorado. These basins contain major shale-bearing intervals (USGS Southwestern Wyoming Province Assessment Team, 2005; Dubiel, 2003; Johnson, 2003; Kirshbaum, 2003; USGS Uinta-Piceance Assessment Team, 2003; Johnson et al., 2010). The oldest of these units is the Permian Phosphoria Formation, which contains organic-rich mudstones. These basins also contain a number of shales that are Cretaceous in age, including the Baxter, Hillard, Steele, Lewis, Mancos and Mowry Shales. Present in all three of these basins is the Eocene Green River Formation, which contains the world's largest oil-shale deposit, with about 1.2 trillion barrels of oil in place (Dubiel, 2003). The Green River Formation consists of interbedded oil shales (such as the Parachute Creek Member), organic shales, evaporites, siltstones, sandstones, and mudstones. The Greater Green River Basin contains a number of sub-basins, including the Hoback Basin, the Green River Basin, the Great Divide Basin, the Washakie Basin, and the Sand Wash Basin (Self et al., 2011). The USGS has generated GIS data (Figure 2-25) that maps the thickness and structure of different members of the Green River Formation in these three basins as part of an oil shale resource assessment (Mercier et al., 2010a, b, c; Mercier and Johnson, 2012).

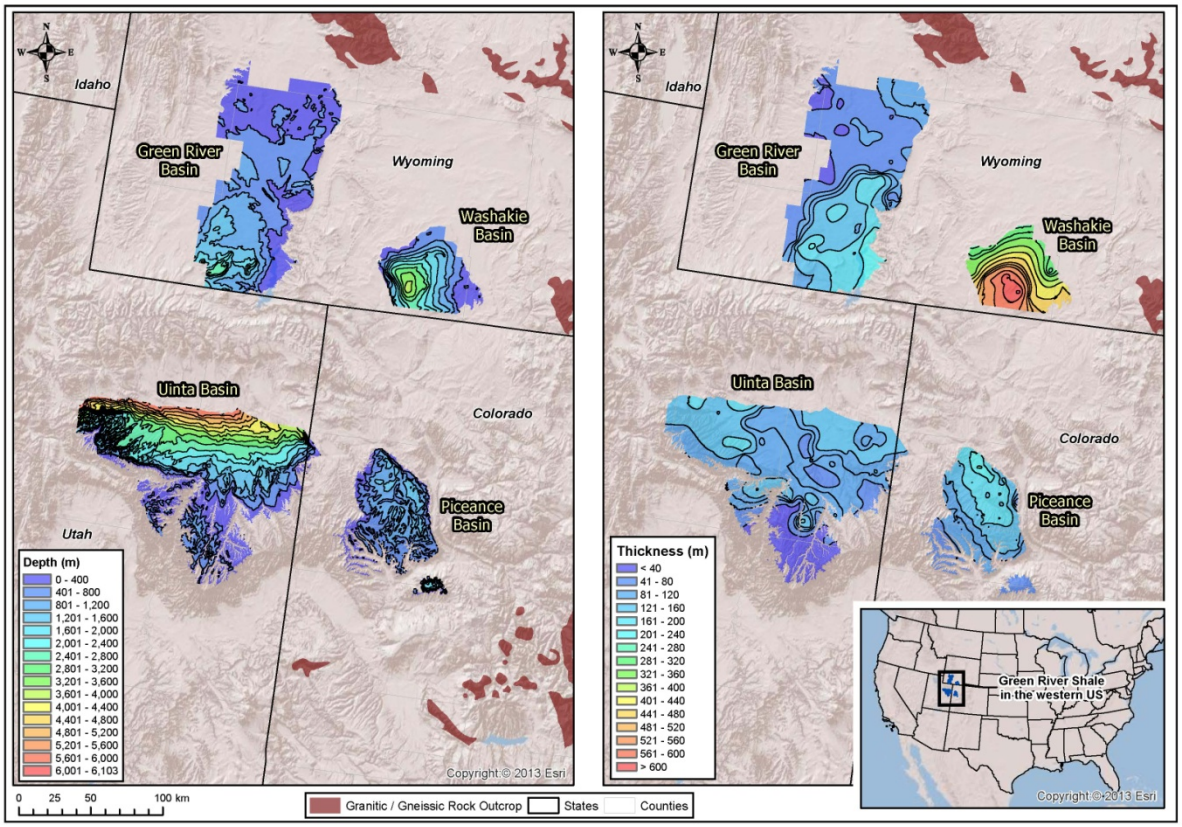


Figure 2-25. Depth and isopach maps of the Green River Shale in the Greater Green River, Uinta, and Piceance Basins. Figure produced by LANL from shale data populated into the GIS database.

### 2.3.14 San Joaquin, Santa Maria, and Cuyama Basins

There are a number of sedimentary basins in central and coastal California which contain thick sequences of siliciclastic rocks; these include the Los Angeles Basin, the San Joaquin Basin, the Ventura Basin, the Santa Maria Basin, and the Cuyama Basin. Most of these sediments are Tertiary in age. The two main shale-rich sedimentary units (which serve as major hydrocarbon source rocks) in these basins are the Miocene Monterey Formation and the Eocene Kreyenhagen Formation (Magoon et al., 2009). The Monterey Formation has a wide variety of lithologies present (Williams, 1982), including diatomite, porcelanite, siliceous, organic-rich and clay shales, chert, dolomite, calcareous siliceous sediments, and siltstones. Hosford Scheirer (2013) developed a 3-D basin model that includes isopach and structural surface maps of the Monterey Formation for the San Joaquin Basin (Figure 2-26).

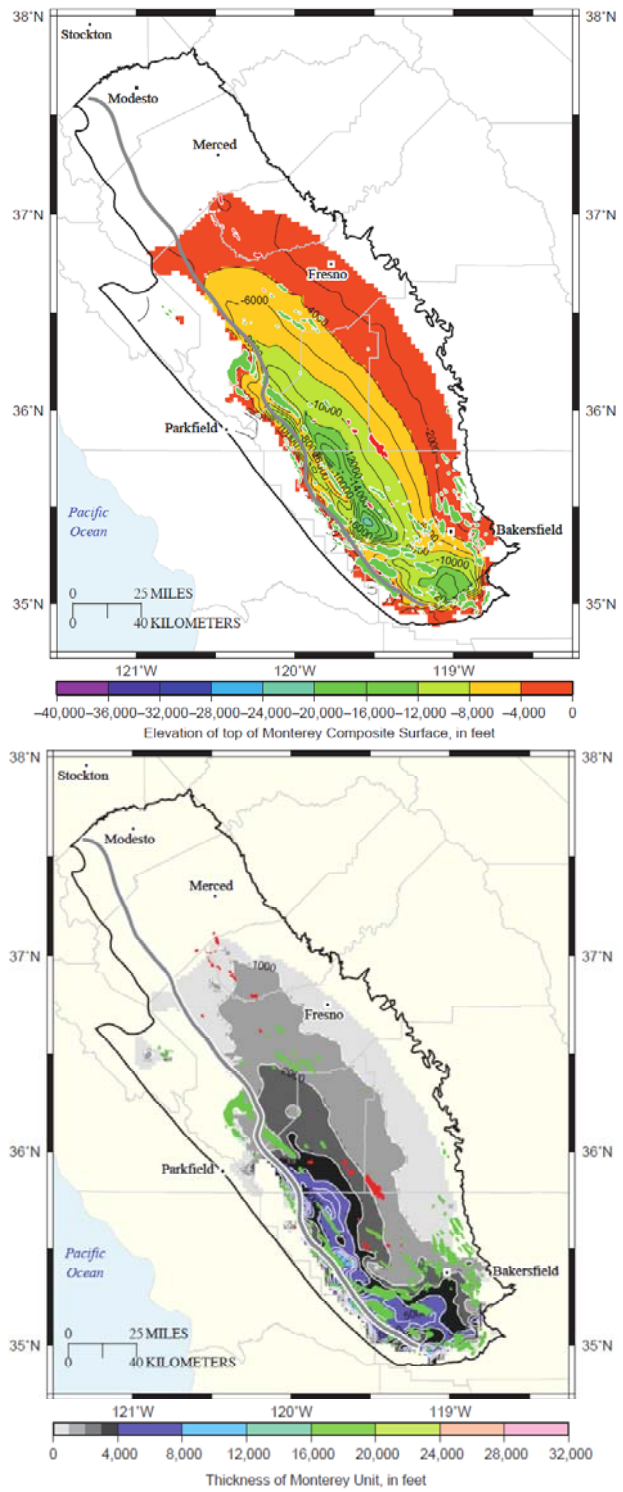


Figure 2-26. Depth and isopach maps of the Monterey Formation in the San Joaquin Basin (Hosford Scheirer, 2013).

## 2.4 CONCLUSIONS

This report serves as an update relating to the progress of obtaining shale formation extent, thickness and depth data for the LANL geologic database. GIS data have been obtained for many shale formations associated with unconventional shale oil and gas deposits, such as the Marcellus, Utica, Barnett, New Albany, Haynesville and Woodford Shales and the Bakken, Monterey, and Green River Formations; Figure 2-27 summarizes the shale formations that have been incorporated into the LANL database. Additional GIS data are in the process of being generated through the digitization of published isopach and structure maps. Continued efforts are being made to obtain additional GIS and map data for other shale formations that can be used to augment the GIS database.

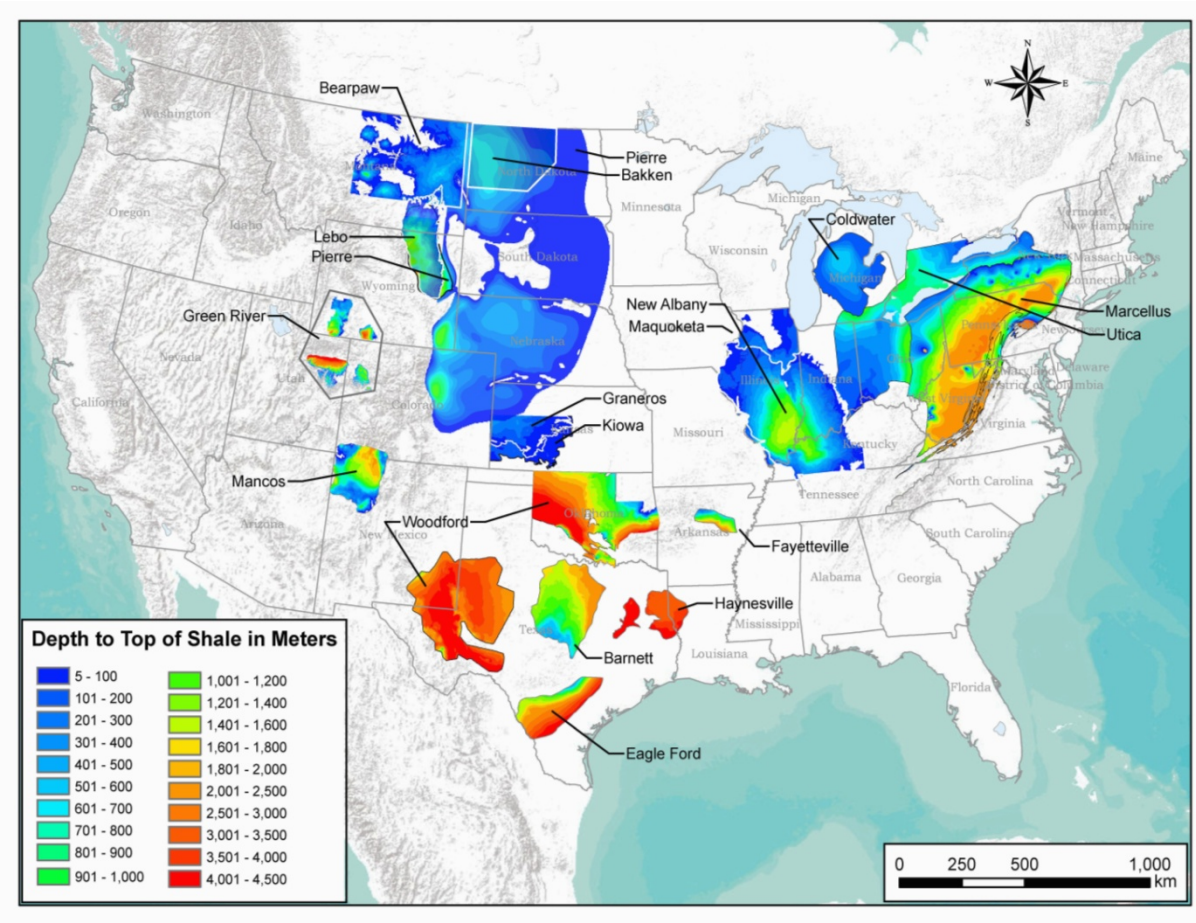


Figure 2-27. Summary of GIS data for depth to top of shale formations within major sedimentary basins in the US currently incorporated in the LANL GIS database. Figure produced by LANL from shale data populated into the GIS database.

## 2.5 REFERENCES

Agrawal, A., 2009. A technical and economic study of completion techniques in five emerging U.S. gas shale plays. M.S. thesis, Texas A&M University, 135 p.

Amsden, T.W., 1975. Hunton Group (Late Ordovician, Silurian, and Early Devonian) in the Anadarko Basin of Oklahoma. Oklahoma Geological Survey Bulletin 121, 214 p.

Amsden, T.W., 1980. Hunton Group (Late Ordovician, Silurian, and Early Devonian) in the Arkoma Basin of Oklahoma. Oklahoma Geological Survey Bulletin 129, 136 p.

Anna, L.O., 2009. Geologic assessment of undiscovered oil and gas in the Powder River Basin Province: U.S. Geological Survey Digital Data Series DDS–69–U, 93 p.

Blackford, M.A., 2007. Electrostratigraphy, thickness, and petrophysical evaluation of the Woodford Shale, Arkoma Basin, Oklahoma. Master's thesis, Oklahoma State University, 84 p.

Bristol, H.M., and Buschbach, T.C., 1973. Ordovician Galena Group (Trenton) of Illinois – Structure and oil fields. Illinois State Geological Survey, Illinois Petroleum 99, 38 p.

Broadhead, R.F., 2010. The Woodford Shale in southeastern New Mexico: distribution and source rock characteristics. New Mexico Geology, v. 32, pp. 79-90.

Broadhead, R.F., and Gillard, L., 2007. The Barnett shale in southeastern New Mexico: Distribution, thickness, and source rock characterization. New Mexico Bureau of Geology and Mineral Resources, Open-File Report 502, 56 p.

Bruner, K.R., and Smosna, R., 2011. A comparative study of the Mississippian Barnett Shale, Fort Worth Basin, and Devonian Marcellus Shale, Appalachian Basin. National Energy Technology Laboratory Report, DOE/NETL-2011/1478.

Cardott, B.J., 2012. Thermal maturity of Woodford Shale gas and oil plays, Oklahoma, USA, International Journal of Coal Geology, doi:10.1016/j.coal.2012.06.004

Cardott, B.J., and Lambert, M.W., 1985. Thermal maturation by vitrinite reflectance of Woodford Shale, Anadarko Basin, Oklahoma. American Association of Petroleum Geologists Bulletin, v. 69, pp. 1982-1998.

Carlson, C.G., 1982. Structure map on top of the Cretaceous Pierre Formation in North Dakota. North Dakota Geological Survey, Miscellaneous Map No. 23.

Catacosinos, P.A., and Daniels, P.A., Jr., 1991, Stratigraphy of middle Proterozoic to Middle Ordovician formations of the Michigan basin. Geological Society of America Special Paper 256, pp. 53–72.

Catacosinos, P.A., Harrison, W.B., III, and Daniels, P.A., Jr., 1991. Structure, stratigraphy, and petroleum geology of the Michigan Basin, Chapter 30, in Leighton, M.W., Kolata D.R., Oltz, D.F., and Eidel, J.J., eds., Interior cratonic basins: American Association of Petroleum Geologists Memoir 51, pp. 561–601.

Coleman, J.L, Jr., and Cahan, S.M., 2012. Preliminary catalog of the sedimentary basins of the United States. U.S. Geological Survey Open-File Report 2012-1111, 27 p.

Collinson, C., Sargent, M. L., and Jennings, J. R., 1988, Chapter 14: Illinois Basin region, *in* Sloss, L. L., ed., The Geology of North America, v. D-2, Sedimentary Cover—North American Craton: U.S.: Decade of North American Geology: Geological Society of America, pp. 383–426.

Comer, J.B., 1991. Stratigraphic analysis of the Upper Devonian Woodford Formation Permian Basin West Texas and Southeastern New Mexico. The University of Texas at Austin, Bureau of Economic Geology Report of Investigations No. 201, 63 p.

Condon, S.M., 2000. Stratigraphic framework of Lower and Upper Cretaceous rocks in central and eastern Montana. U.S Geological Survey Digital Data Series DDS-57, 12 p, 23 plates.

Cuadros, J., 2008. Clay as sealing material in nuclear waste repositories. Geology Today, v. 24, p. 99-103.

Dechesne, M., Raynolds, R.G., Barkmann, P.E., and Johnson, K.R., 2011. Notes on the Denver Basin geologic maps: Bedrock geology, structure, and isopach maps of the Upper Cretaceous to Paleogene strata between Greeley and Colorado Springs, Colorado. Colorado Geological Survey, 35 p.

Denson, N.M., Gibson, M.L., and Sims, G.L., 1993a. Geologic and structure map, with contours on top of the Pierre Shale, for the north half of the Powder River Basin, southeastern Montana and northeastern Wyoming. U.S. Geological Survey Miscellaneous Investigations Series Map I-2343-A.

Denson, N.M., Gibson, M.L., and Sims, G.L., 1993b. Geologic and structure map, with contours on top of the Pierre Shale, for the south half of the Powder River Basin, northeastern Wyoming. U.S. Geological Survey Miscellaneous Investigations Series Map I-2343-B.

Denson, N.M., Gibson, M.L., and Sims, G.L., 1993c. Geologic map showing thickness of the Upper Cretaceous Pierre Shale in the north half of the Powder River Basin, southeastern Montana and northeastern Wyoming. U.S. Geological Survey Miscellaneous Investigations Series Map I-2380-A.

Denson, N.M., Gibson, M.L., and Sims, G.L., 1993d. Geologic map showing thickness of the Upper Cretaceous Pierre Shale in the south half of the Powder River Basin, northeastern Wyoming and adjacent areas. U.S. Geological Survey Miscellaneous Investigations Series Map I-2380-B.

Dobson, P., 2011. Survey of clay/shale formations in the US. In: FY11 Report on Unsaturated Flow and Transport, FCRD-USED-2011-000296.

Dobson, P., 2012. Status of Shale Geology: Information on Extent, Thickness and Depth of Shale Deposits, FCRD-UFD-2012-000296.

Dubiel, R.F., 2003. Geology, depositional models, and oil and gas assessment of the Green River Total Petroleum System, Uinta-Piceance Province, Eastern Utah and Western Colorado, Chapter 5 of Petroleum systems and geologic assessment of oil and gas in the Uinta-Piceance Province, Utah and Colorado, USGS Uinta-Piceance Assessment Team, U.S. Geological Survey Digital Data Series DDS–69–B. http://pubs.usgs.gov/dds/dds-069/dds-069-b/REPORTS/Chapter_5.pdf

Energy Information Administration (EIA), 2010, Eagle Ford Shale Play, Western Gulf Basin, South Texas. Map date May 29, 2010. http://www.eia.gov/oil_gas/rpd/shaleusa9.pdf

Energy Information Administration (EIA), 2011. Review of Emerging Resources: U.S. Shale Gas and Shale Oil Plays. www.eia.gov/analysis/studies/usshalegas/pdf/usshaleplays.pdf

Engelder, T., 2011. Analogue study of shale cap rock barrier integrity. Report for the Nuclear Waste Management Organization, NWMO DGR-TR-2011-23, 108 p.

Erenpreiss, M.S., Wickstrom, L.H., Perry C.J., Riley, R.A., Martin, D.R., and others, 2011. Regional organic-thickness map of the Marcellus Shale with additional organic-rich shale beds in the Hamilton Group included for New York, Pennsylvania, and West Virginia. Ohio Department of Natural Resources, Division of Geological Survey, scale 1 inch equals 52 miles.

Ettensohn, F.R., 2008. The Appalachian foreland basin in Eastern United States. In: Miall, A.D. (ed.) The Sedimentary Basins of the United States and Canada, Vol. 5, Sedimentary Basins of the World. Elsevier, Amsterdam, pp. 105–179.

Gale, J.F.W., and Holder, J., 2010. Natural fractures in some US shales and their importance for gas production. In: Vining, B.A., and Pickering, S.C., eds., Petroleum Geology: From Mature Basins to New Frontiers. Proceedings of the 7th Petroleum Geology Conference, pp. 1131-1140.

Gerhard, L.C., Anderson, S.B., Lefever, J.A. and Carlson, C.G., 1982. Geological development, origin, and energy mineral resources of Williston Basin, North Dakota. American Association of Petroleum Geologists Bulletin v. 66, pp. 989–1020.

Gonzales, S., and Johnson, K.S., 1985. Shales and other argillaceous strata in the United States. Oak Ridge National Laboratory report 84-64794, 594 p.

Gray, J.D., Struble, R.A., Carlton, R.W., Hodges, D.A., Honeycutt, F.M., Kingsbury, R.H., Knapp, N.F., Majchszak, F.L., and Stith, D.A., 1982. An integrated study of the Devonian-age black shales in eastern Ohio. Technical Information Center, US Department of Energy, DOE/ET/12131-1399.

Hammes, U., Hamlin, H.S., and Ewing, T.E., 2011. Geologic analysis of the Upper Jurassic Haynesville Shale in east Texas and west Louisiana. AAPG Bulletin, v. 95, no. 10, pp. 1643–1666.

Harbor, R.L., 2011. Facies characterization and stratigraphic architecture of organic-rich Mudrocks, Upper Cretaceous Eagle Ford Formation, South Texas. M.S. Thesis, University of Texas, Austin, 184 p.

Hasenmueller, N.R., and Comer, J.B., eds., 1994. Gas potential of the New Albany Shale (Devonian and Mississippian) in the Illinois Basin**,** Gas Research Institute Technical Report GRI-92/0391.

Hasenmueller, N.R., and Comer, J.B., eds., 2000. GIS compilation of gas potential of the New Albany Shale in the Illinois Basin, Gas Research Institute Technical Report GRI-00/0068.

Higley, D.K. and Cox, D.O., 2007. Oil and gas exploration and development along the front range in the Denver Basin of Colorado, Nebraska, and Wyoming, in Higley, D.K., compiler, Petroleum systems and assessment of undiscovered oil and gas in the Denver Basin Province, Colorado, Kansas, Nebraska, South Dakota, and Wyoming—USGS Province 39: U.S. Geological Survey Digital Data Series DDS–69–P, ch. 2, 41 p. http://pubs.usgs.gov/dds/dds-069/dds-069-p/REPORTS/69_P_CH_2.pdf

Hosford Scheirer, A., 2013. The three-dimensional geologic model used for the 2003 National Oil and Gas Assessment of the San Joaquin Basin Province, California: Chapter 7 in Petroleum systems and geologic assessment of oil and gas in the San Joaquin Basin Province, California, U.S. Geological Survey Professional Paper 1713-7, 81 p.

Hovorka, S.D., Romero, M.L., Warne, A.G., Ambrose, W.A., Tremblay, T.A., Treviño, R.H., and Sasson, D., 2003. Technical summary: Optimal geological environments for carbon dioxide disposal in brine formations (saline aquifers) in the United States. Gulf Coast Carbon Center, University of Texas, Bureau of Economic Geology, http://www.beg.utexas.edu/gccc/finalreport.pdf

Johnson, E.A., 2003. Geologic assessment of the Phosphoria Total Petroleum System, Uinta-Piceance Province, Utah and Colorado, Chapter 9 of Petroleum systems and geologic assessment of oil and gas in the Uinta-Piceance Province, Utah and Colorado, USGS Uinta-Piceance Assessment Team, U.S. Geological Survey Digital Data Series DDS–69–B, http://pubs.usgs.gov/dds/dds-069/dds-069-b/REPORTS/Chapter_9.pdf

Johnson, R.C., Mercier, T.J., Brownfield, M.E. and Self, J.G., 2010. Assessment of in-place oil shale resources in the Eocene Green River Formation, Uinta Basin, Utah and Colorado: U.S. Geological Survey Digital Data Series DDS–69–BB, Ch. 1, 153 p. http://pubs.usgs.gov/dds/dds-069/dds-069-bb/REPORTS/69_BB_CH_1.pdf

Kirschbaum, M.A., 2003. Geologic assessment of undiscovered oil and gas resources of the Mancos/Mowry Total Petroleum System, Uinta-Piceance Province, Utah and Colorado. Chapter 6 of Petroleum Systems and Geologic Assessment of Oil and Gas in the Uinta-Piceance Province, Utah and Colorado, USGS Uinta-Piceance Assessment Team, U.S. Geological Survey Digital Data Series DDS–69–B, http://pubs.usgs.gov/dds/dds-069/dds-069-b/REPORTS/Chapter_6.pdf

Kolata, D.R., and Noger, M.C., 1990. Chapter 5: Tippecanoe I Subsequence Middle and Upper Ordovician Series. In: Interior Cratonic Basins, M.W. Leighton, D.R. Kolata, D.F. Oltz, and J.J. Eider., eds. American Association of Petroleum Geologists Memoir 51, pp. 89–99.

Lagoe, M.B., 1982. Stratigraphy and paleoenvironments of the Monterey Formation and associated rocks, Cuyama Basin, California. Ph.D. thesis, Stanford University, 216 p.

Lagoe, M.B., 1984. Paleogeography of Monterey Formation, Cuyama Basin, California. American Association of Petroleum Geologists Bulletin, v. 68, pp. 610–627.

Lash, G.G., and Engelder, T., 2011. Thickness trends and sequence stratigraphy of the Middle Devonian Marcellus Formation, Appalachian Basin: Implications for Acadian foreland basin evolution. American Association of Petroleum Geologists Bulletin v. 95, pp. 61–103.

LeFever, J.A., 2008. Structural contour and isopach maps of the Bakken Formation in North Dakota. North Dakota Geological Survey Geologic Investigations No. 59, 5 sheets.

LeFever, J.A., LeFever, R.D., and Nordeng, S.H., 2012. Extending the Bakken. Williston Basin Petroleum Conference.

Lewis, B.D., and Hotchkiss, W.R., 1981. Thickness, percent sand, and configuration of shallow hydrogeologic units in the Powder River Basin, Montana and Wyoming. U.S. Geological Survey Miscellaneous Investigations Series, Map I-1317.

Li, P., Ratchford, M.E., and Jarvie, D.M., 2010. Geochemistry and thermal maturation analysis of the Fayetteville Shale and Chattanooga Shale in the western Arkoma Basin of Arkansas. Arkansas Geological Survey Information Circular 40, 191 p.

Macfarlane, P.A., Combes, J., Turbek, S., and Kirshen, D., 1993. Shallow subsurface bedrock geology and hydrostratigraphy of southwestern Kansas. Kansas Geological Survey, Open-File Report 93-1a. (plates updated in 2010 by J.J. Woods).

Magoon, L.B., Lillis, P.G., and Peters, K.E., 2009. Petroleum systems used to determine the assessment units in the San Joaquin Basin Province, California: Chapter 8 in Petroleum systems and geologic assessment of oil and gas in the San Joaquin Basin Province, California, U.S. Geological Survey Professional Paper 1713-8, 65 p.

Mercier, T.J., Gunther, G.L., and Skinner, C.C., 2010a. The GIS project for the geologic assessment of in-place oil shale resources of the Eocene Green River Formation, Greater Green River Basin, Wyoming, Colorado, and Utah, U.S. Geological Survey Oil Shale Assessment Team, U.S. Geological Survey Digital Data Series DDS–69–DD, http://pubs.usgs.gov/dds/dds-069/dds-069-dd/REPORTS/69_DD_CH_3.pdf

Mercier, T.J., Gunther, G.L., and Skinner, C.C., 2010b. The GIS project for the geologic assessment of in-place oil shale resources of the Piceance Basin, Colorado. In: Oil shale and nahcolite resources of the Piceance Basin, Colorado, U.S. Geological Survey Oil Shale Assessment Team, U.S. Geological Survey Digital Data Series DDS–69–Y, http://pubs.usgs.gov/dds/dds-069/dds-069-y/REPORTS/69_Y_CH_4.pdf

Mercier, T.J., Gunther, G.L., and Skinner, C.C., 2010c. The GIS project for the geologic assessment of in-place oil shale resources of the Uinta Basin, Utah and Colorado. In: Oil shale resources of the Uinta Basin, Utah and Colorado, U.S. Geological Survey Oil Shale Assessment Team, U.S. Geological Survey Digital Data Series DDS–69–BB, http://pubs.usgs.gov/dds/dds-069/dds-069-bb/REPORTS/69_BB_CH_4.pdf

Mercier, T.J., and Johnson, R.C., 2012. Isopach and isoresource maps for oil shale deposits in the Eocene Green River Formation for the combined Uinta and Piceance Basins, Utah and Colorado: U.S. Geological Survey Scientific Investigations Report 2012–5076, 85 p., 1 pl., http://pubs.usgs.gov/sir/2012/5076/SIR12-5076.pdf

Merewether, E.A., Sharps, J.A., Gill, J.R., and Cooley, M.E., 1973. Shale, mudstone, and claystone as potential host rocks for underground emplacement of waste. U.S. Geological Survey Open-File Report 73-184, 44 p.

Party, J.M., Wipf, R.A., Byl, J.M., Lawton, J., and Hill, J.M., 2008. Woodford Shale, Ardmore Basin, Oklahoma: A developing shale play. Oklahoma Geological Survey, Gas Shales Workshop, 51 slides. http://www.ogs.ou.edu/pdf/GSPartyS.pdf.

Pashin, J.C., 2008. Gas shale potential of Alabama. 2008 International Coalbed and Shale Gas Symposium, Paper 808.

Patchen, D.G., Hickman, J.B., Harris, D.C., Drahovzal, J.A., Lake, P.D., Smith, L.B., Nyahay, R., Schulze, R., Riley, R.A., Baranoski, M.T., Wickstrom, L.H., Laughrey, C.D., Kostelnik, J., Harper, J.A., Avary, K.L., Bocan, J., Hohn, M.E., and McDowell, R., 2006. A Geologic play book for Trenton-Black River Appalachian Basin exploration. DOE Award DE-FC26-03NT41856, http://www.wvgs.wvnet.edu/www/tbr/docs/41856R06.pdf

Pawlewicz, M.J. and Hatch, J.R., 2007. Petroleum assessment of the Chattanooga Shale/Floyd Shale - Paleozoic Total Petroleum System, Black Warrior Basin, Alabama and Mississippi, in Hatch, J.R., and Pawlewicz, J.J., compilers, Geologic assessment of undiscovered oil and gas resources of the Black Warrior Basin Province, Alabama and Mississippi. U.S. Geological Survey Digital Data Series DDS-69-I, chap. 3, 23 p. http://pubs.usgs.gov/dds/dds-069/dds-069-i/REPORTS/69_I_CH_3.pdf

Perry, F.V., Dobson, P.F., and Kelley, R.E., 2013. Assessment of alternative host-rock distribution in the U.S. using GIS. Proceedings, International High-Level Waste Management Conference 2013, Albuquerque, N.M., April 28-May 2, 2013, American Nuclear Society, pp. 85–93.

Perry, F.V., Kelley, R., and Dobson, P., 2012. Regional geology: Distribution of alternative host rock formations and description of siting factors that potentially influence siting and site characterization. FCRD-USED-2012-27013.

Perry, F., Kelley, R., and Woldegabriel, G., 2011. Regional geology and tectonic hazards – FY 2011 Status Report. FCRD-USED-2012-000002.

Peterson, J.A., 1984. Geology and hydrology of the Madison Limestone and associated rocks in parts of Montana, Nebraska, North Dakota, South Dakota, and Wyoming. U.S. Geological Survey Professional Paper 1273A, 34 p.

Pitman, J.K., 2008. Reservoirs and Petroleum Systems of the Gulf Coast. AAPG Datapages GIS Open-File website. http://www.datapages.com/AssociatedWebsites/GISOpenFiles/ReservoirsandPetroleumSystemsoftheGulfCoast.aspx

Pollastro, R.M., Jarvie, D.M., Hill, R.J., and Adams, C.W., 2007. Geologic framework of the Mississippian Barnett Shale, Barnett-Paleozoic total petroleum system, Bend Arch–Fort Worth Basin, Texas. American Association of Petroleum Geologists Bulletin v. 91, pp. 405–436.

Pollastro, R.M., Roberts, L.N.R., Cook, T.A. and Lewan, M.D., 2008. Assessment of undiscovered technically recoverable oil and gas resources of the Bakken Formation, Williston Basin, Montana and North Dakota, 2008: U.S. Geological Survey Open-File Report 2008–1353, 3 sheets.

Ratchford, M.E., Bridges, L.C., Jordan, D., Dow, W.G., Colbert, A., and Jarvie, D.M., 2006. Organic geochemistry and thermal maturation analysis within the Fayetteville Shale study area – Eastern Arkoma Basin and Mississippi embayment regions, Arkansas. Arkansas Geological Survey Information Circular 37, DFF-OG-FS-EAB/ME 008, 12 p.

Rechard, R.P., Perry, F.V., and Cotton, T.A., 2011. Site selection, characterization, and research and development for spent nuclear fuel and high-level waste disposal. International High-Level Radioactive Waste Management Conference 2001, Albuquerque, NM, April 10-14, 2011, American Nuclear Society, pp. 174-181.

Ridgley, J.L., Condon, S.M., and Hatch, J.R., 2013. Geology and oil and gas assessment of the Mancos-Menefee Composite Total Petroleum System, San Juan Basin, New Mexico and Colorado, chap. 4 *of* U.S. Geological Survey San Juan Basin Assessment Team, Total petroleum systems and geologic assessment of undiscovered oil and gas resources in the San Juan Basin Province, exclusive of Paleozoic rocks, New Mexico and Colorado. U.S. Geological Survey Digital Data Series 69–F, p. 1–97.

Rottmann, K., 2000. Isopach map of Woodford Shale in Oklahoma and Texas Panhandle. In: Hunton play in Oklahoma (including northeast Texas panhandle): Oklahoma Geological Survey Special Publication 2000-2, plate 2.

Ruppel, S.C., Jones, R.H., Breton, C.L, and Kane, J.A., 2005. Preparation of maps depicting geothermal gradient and Precambrian structure in the Permian Basin: unpublished contract report prepared for the U. S. Geological Survey, 21 p. plus data CD.

Ryder, R.T., Burruss, R.C. and Hatch, J.R., 1998. Black shale source rocks and oil generation in the Cambrian and Ordovician of the central Appalachian Basin, USA. AAPG Bulletin 82, pp. 412-441.

Self, J.G., Ryder, R.T., Johnson, R.C., Brownfield, M.E., and Mercier, T.J., 2011. Stratigraphic cross sections of the Eocene Green River Formation in the Green River Basin, southwestern Wyoming, northwestern Colorado, and northeastern Utah, in U.S. Geological Survey Oil Shale Assessment Team, ed., Oil shale resources in the Eocene Green River Formation, Greater Green River Basin, Wyoming, Colorado, and Utah. U.S. Geological Survey Digital Data Series DDS–69–DD, chap. 5, 7 p., 24 plates.

Shurr, G.W., 1977. The Pierre Shale, Northern Great Plains; A potential isolation medium for radioactive waste. U.S. Geological Survey Open File Report 77-776, 27 p.

Smith, L.N., 1999. Structure contour map on the top of the Upper Cretaceous Pierre (Bearpaw) Shale, east-central Montana. Montana Bureau of Mines and Geology, Montana Ground-Water Assessment Open-File Report 13, Revision 1.1.

Surles, M.A., Jr., 1987. Stratigraphy of the Eagle Ford Group (Upper Cretaceous) and its source-rock potential in the East Texas Basin. Baylor Geological Studies Bulletin No. 45, 57 p.

Sweetkind, D.S., Tennyson, M.E., Langenheim, V.E., and Shumaker, L.E., 2010. Digital tabulation of stratigraphic data from oil and gas wells in the Santa Maria Basin and surrounding areas, central California coast. U.S. Geological Survey Open-File Report 2010-1129, 11 p.

Sweetkind, D.S., Bova, S.C., Langenheim, V.E., Shumaker, L.E., and Scheirer, D.S., 2013. Digital tabulation of stratigraphic data from oil and gas wells in Cuyama Valley and surrounding areas, central California. U.S. Geological Survey Open-File Report 2013-1084, 44 p.

Swezey, C.S., 2008. Regional stratigraphy and petroleum systems of the Michigan Basin, North America. U.S. Geological Survey Scientific Investigations Map 2978, 1 sheet. http://pubs.usgs.gov/sim/2978/sim2978MichChart.pdf

Swezey, C.S., 2009. Regional stratigraphy and petroleum systems of the Illinois Basin, U.S.A. U.S. Geological Survey Scientific Investigations Map 3068, 1 sheet. http://pubs.usgs.gov/sim/3068/illinoisbasin.pdf

Thomas, W.A., 1988. The Black Warrior Basin. In: Sloss, L.L., ed., The Geology of North America, v. D-2, Sedimentary Cover—North American Craton: U.S.: Decade of North American Geology: Geological Society of America, pp. 471–492.

USGS Southwestern Wyoming Province Assessment Team, 2005. The Southwestern Wyoming Province — Introduction to a geologic assessment of undiscovered oil and gas resources, U.S. Geological Survey Digital Data Series DDS–69–D, Chapter 2, 34 p. http://pubs.usgs.gov/dds/dds-069/dds-069-d/REPORTS/69_D_CH_2.pdf

USGS Uinta-Piceance Assessment Team, 2003. Petroleum systems and geologic assessment of oil and gas in the Uinta-Piceance Province, Utah and Colorado: U.S. Geological Survey Digital Data Series DDS–69–B, Ch. 2. http://pubs.usgs.gov/dds/dds-069/dds-069-b/REPORTS/Chapter_2.pdf

Williams, L.A., 1982. Lithology of the Monterey Formation (Miocene) in the San Joaquin Valley of California. In: Williams, L.A., and Graham, S.A., eds., Monterey Formation and associated coarse clastic rocks, central San Joaquin Basin, California. Pacific Section, Society of Economic Paleontologists and Mineralogists Annual Field Trip Guidebook, pp. 17-35.

Willman, H.B., Atherton, W., Buschbach, T.C., Collinson, C., Frye, J.C., Hopkins, M.E., and Lineback, J.A., 1975. Handbook of Illinois stratigraphy, Illinois Geological Survey Bulletin 95, 261 p.

Wylie, A.S., Jr., and Wood, J.R., 2004. Map views of the producing formations in Michigan, the Michigan Basin, U.S. American Association of Petroleum Geologists Eastern Section Meeting, Columbus, OH, Oct. 3-6, 2004.

Wylie, A.S., and Wood, J.R., 2005. Historical production trends suggest remaining upside for E&D in Michigan. Oil and Gas Journal, vol. 103, issue 23.

# 3. ROCK PROPERTIES AND IN-SITU CONDITIONS FOR SHALE ESTIMATED FROM SONIC VELOCITY MEASUREMENTS

Data for assessing the properties of shale formations for nuclear waste disposal are often limited by a lack of direct measurements, either performed in-situ or on laboratory samples taken from the formation. Here we use the term "shale" as a general term describing any fine-grained argillaceous, or clay-rich, clastic rock, including mudstones, claystones, and argillites. The USGS definitions indicate that mudstone is a term that encompasses claystones, shales, argillites, and siltstones (USGS 2013), and might be a more suitable generic term for rock type studied here. In this section, correlations for estimating hydrological and geomechanical formation properties and in-situ conditions from sonic velocities are developed from data on shale formations that lie outside of the United States. The advantage of using correlations based on sonic velocity is that properties can be estimated from geophysical logs. This information is often more readily available than direct property measurements on core that would otherwise be required. Furthermore, geophysical logs typically provide a continuous readout along wells that can be more readily used to characterize spatial variability in properties. The correlations developed are then used to assess properties and conditions in several shale formations of interest within the United States.

## 3.1 DATA USED TO DEVELOP THE CORRELATIONS

Data used for developing the correlations are given in Tables 3-1 through 3-3. Table 3-1 is based on formations reported on by Boisson (2005), who documented characteristics of shale formations being investigated for high-level nuclear waste disposal. The data are generally presented in terms of a maximum, minimum, and "best" value for each parameter. Table 3-1 presents the "best" values, or in cases where only a maximum and minimum were presented, the average is used as "best". Furthermore, the porosity data are averaged over different types of porosity measurements that were reported (e.g., as determined by water content and grain density, or by mercury injection). Clay content is the mass of all clay mineral types divided by the total rock mass. Permeabilities are converted from reported hydraulic conductivities measured either in-situ or on core samples in the laboratory. The uniaxial compressive strength and permeabilities were reported in terms of directional values for some of the formations, but in many cases orientation is not known. In addition, more recent and/or more complete information for some parameters and formations was found from other sources, as indicated in Table 3-1.

Additional types of properties data for some of the same formations reported on by Boisson (2005) but taken from a variety of other sources are given in Table 3-2. This table provides bulk density, Young's modulus, shear strength, cohesive strength, friction angle, and tensile strength. For the Opalinus Clay-Mont Terri, Opalinus Clay-Benken, Callovo-Oxfordian, and Tournemire argillite, directional values of Young's modulus are available. Similarly, for the Opalinus Clay-Mont Terri, Opalinus Clay-Benken, and Callovo-Oxfordian Clay, cohesive strength, and tensile strength have directional information related to the parameters.

Table 3-1. Data from Boisson (2005) (except as noted)

| formation | sonic velocity (m/s) | porosity | clay content | uniaxial compressive strength (MPa) | depth (m) | maximum burial depth (m) | permeability (in-situ, $m^2$) | permeability (lab, $m^2$) |
|---|---|---|---|---|---|---|---|---|
| Boom Clay | 1710[1] (1970)[1] | 0.38[6] | 0.600 | 2.21* | 176 | 176 | 2.31E-19 (4.78E-19) | 3.34E-19 (7.27e-19) |
| Oxford Clay | 1776[2] (1798)[2] | 0.42[7] | 0.560 | 2.21* | 265 | - | - | - |
| Ypresian Clay | 1805* | 0.422[8] | 0.605 | 1.47* | 324 | 471 | 3.78E-17* | 6.74E-19[8] (8.03e-19)[8] |
| Opalinus Clay – Mont Terri | 2620[3] (3350)[3] | 0.137[3] | 0.597 | 15[3] (11)[3] | 235 | 1353 | 4.19E-21 (1.94E-20) | 7.14E-21[3] (2.04E-20)[3] |
| Spanish Reference Clay | 2642* | 0.290 | 0.775 | 2.94* | 147 | 265 | 1.29E-19* | 1.92E-18* |
| Callovo-Oxfordian Clay | 2900[4] (3400)[4] | 0.16[4] | 0.450 | 21[4] | 412 | - | 3.39E-22* | 7.90E-21[4] (1.02e-20)[4] |
| Konrad mine – lower Cretaceous Claystone | 2925* | - | 0.583 | - | 250 | - | - | - |
| Konrad mine – lower Cretaceous Claystone – Albian | 2972* | - | 0.496 | - | 250 | - | 1.02E-17 | - |
| Opalinus Clay – Zurich Weinland | 3030[4] (4030)[4] | 0.124[4] | 0.533 | 29.4 (27.9) | 544 | 1588 | 2.91E-21* (1.08E-20) | 1.92E-21 (9.90E-21) |
| Tournemire argillite | 4434[5] (3799)[5] | 0.090[9] | 0.550 | 32.4 | 250 | 1000 | 2.00E-21[10] 6.00E-21[10] | 1.05E-21* |
| Konrad mine – lower Cretaceous Claystone – Callovo | 3774* | 0.099 | 0.517 | 73.5 | 912 | 912 | 1.15E-18 | - |
| Palfris formation – Wellenberg | 4586* | 0.013 | 0.430 | 47.1 (52.9) | 397 | > 3000 | 3.32E-19* | 6.50E-21[11]* |
| Boda claystone | 5094* | 0.012 | 0.400 | 115 | 294 | >3000 | 9.62E-20* | - |

Note: for directionally-sensitive parameters (sonic velocity, uniaxial compressive strength, permeability) values for both normal and parallel to bedding are shown where available; first values are for orientation normal to bedding followed by numbers in parentheses for values parallel to bedding. Single values are for normal to bedding unless marked with * indicating orientation is unknown.

Sources other than Boisson (2005): [1] Dehandshutter et al. (2005a); [2] Kerner et al. (1989); [3] Bock (2009); [4] Wenk et al. (2008); (5) Zinszer et al. (2002); [6] Shaw (2010); [7] Midttøme et al. (1998); [8] Piña-Diaz (2011); [9] Matray et al. (2007); [10] Millard and Rejeb (2008); [11] Fedor et al. (2008)

Table 3-2. Additional Properties of Some Formations from Table 1.

| formation | saturated bulk density ($kg/m^3$) | Young's modulus (GPa) | shear modulus (GPa) | Poisson's Ratio | cohesive strength (MPa) | friction angle (degrees) | tensile strength (MPa) |
|---|---|---|---|---|---|---|---|
| Boom Clay | 2050[1] | 0.35*[9] | 0.04*[15] | 0.4*[19] | 0.24*[15] | 18*[15] | 0.1*[17] |
| Oxford Clay | 1940[2] | 0.1*+[10] | 0.034*$[10][20] | 0.47*[20] | 0.17*+[10] | 20.3*[17] | - |
| Ypresian Clay | 2000[1] | 0.042*[11] | 0.017*$[11] | 0.25*[11] | 0.36*[11] | 10.6*[11] | - |
| Opalinus Clay – Mont Terri | 2430[3] | 4[3] (10)[3] | 2.4$@ [3] | 0.29@[3] | 3[3] (4)[3] | 22[3] | 0.6[3] (1.2)[3] |
| Callovo-Oxfordian Clay | 2480[4] | 4.0[12] (5.6)[12] | 2.4*[16] | 0.3*[12] | 3.0[12] (7.0)[12] | 22.5*[12] | 2.6*[18] |
| Opalinus Clay – Zurich Weinland | 2520[4] | 5.0[13] (10.5)[13] | 2.0$[13] | 0.25[13] | 1.6[13] (7.6)[13] | 22*[13] | 1.2[13] (2.7)[13] |
| Tournemire argillite | 2551#[5] | 7.0[14] (22.0)[14] | 2.0[14] | 0.16[21] | - | - | - |
| Konrad mine – lower Cretaceous Claystone – Callovo | 2585#[6] | - | - | - | - | - | - |
| Palfris formation - Wellenberg | 2629#[7] | - | - | - | - | - | - |
| Boda claystone | 2803##[8] | - | - | - | - | - | - |

Note: for directionally-sensitive parameters (all of the above with the exception of bulk density) values for both normal and parallel to bedding are shown where available; first values are for orientation normal to bedding followed by numbers in parentheses for values parallel to bedding. Single values are for normal to bedding unless marked with * indicating orientation is unknown.

# saturated bulk density based on porosity and grain density

## saturated bulk density based on porosity and dry bulk density

+ extrapolated to zero confining stress

$ computed using Poisson ratio and Young's modulus

[@] computed from approximation reported by Bock (2009) $\frac{1}{G_n} = \frac{1}{E_n} + \frac{1}{E_p} + \frac{2\upsilon_p}{E_p}$, where $G_n$ is the shear modulus normal to bedding, $E_n$ is Young's modulus normal to bedding, $E_p$ is Young's modulus parallel to bedding, and $\upsilon_p$ is Poisson's ratio parallel to bedding. Bock (2009) gives a value of 0.35 for $\upsilon_p$.

Sources: [(1)] Lima et al. (2012); [(2)] Midttøme et al. (1998); [(3)] Bock (2009); [(4)] Wenk et al. (2008); [(9)] Matray et al. (2007); [(6)] EAEC (1984); [(7)] Baeyens and Bradbury (1994); [(8)] Fedor et al. (2008); [(9)] Shaw (2010); [(10)] Kutschke and Vallejo (2012); [(11)] Piña-Diaz (2011); [(12)] Charlier et al. (2013); [(13)] Volckaert (2004); [(14)] Giraud et al. (2007); [(15)] Dehandshutter et al. (2005b); [(16)] Jougnot et al. (2010); [(17)] Burland et al. (1977); [(18)] Ghorbani et al. (2009); [(19)] Bastiens et al. (2007); [(20)] Kerner et al. (1989); [(21)] Niandou et al. (1997)

Similar data are available from Horsrud (2001), who also developed several correlations between sonic velocity and petrophysical parameters. These data are mainly from formations in the North Sea that are of interest for petroleum resource development. The data presented by Horsrud (2001) are given in Table 3-3.

Table 3-3. Horsrud (2001) Properties Data

| formation | sonic velocity (m/s)* | porosity | clay content | uniaxial compressive strength (MPa)* | Young's modulus (GPa)* | shear modulus (GPa)* | depth (m) |
|---|---|---|---|---|---|---|---|
| Mo Clay | 1706 | 0.72 | 0.25 | 1.67 | 0.30 | 0.19 | 0 |
| Smectite | 1757 | 0.57 | 0.99 | 2.08 | 0.22 | 0.10 | 0 |
| London Clay | 1796 | 0.45 | 0.65 | 1.67 | 0.07 | 0.10 | 0 |
| Tertiary Miocene | 1886 | 0.55 | 0.53 | 6.25 | 0.81 | 0.29 | 1370 |
| Tertiary Paleocene-3 | 2143 | 0.31 | 0.52 | 7.92 | 1.04 | 0.42 | 1940 |
| Tertiary Paleocene-2 | 2413 | 0.34 | 0.56 | 12.92 | 1.93 | 0.71 | 1870 |
| Tertiary Paleocene-1 | 2439 | 0.31 | 0.34 | 12.50 | 1.63 | 0.71 | 1720 |
| Upper Jurassic-1 | 2529 | 0.3 | 0.32 | 7.92 | 1.11 | 0.42 | 3160 |
| Upper Jurassic-3 | 2966 | 0.17 | 0.47 | 18.33 | 2.59 | 1.01 | 2550 |
| Triassic | 3018 | 0.15 | 0.65 | 13.33 | 2.00 | 0.91 | 2440 |
| Upper Jurassic-2 | 3185 | 0.1 | 0.58 | 27.08 | 3.85 | 1.36 | 2630 |
| Middle Jurassic | 4818 | 0.03 | 0.49 | 77.50 | 12.22 | 5.39 | 4870 |

* normal to bedding

As can be seen from Tables 3-1 and 3-3, the formations reported on by Boisson (2005) are at depths less than 1000 m whereas the formations selected by Horsrud (2001) are mainly at depths greater than 1000 m. However, the maximum burial depths of several of the Boisson (2005) formations were at some time in the past greater than 1000 m. Although the Horsrud (2001) measurements were made normal to bedding, Horsrud (2001) reports that velocities parallel to bedding ranged from 0 to 25% larger than the normal-to-bedding velocities. The Mo Clay data in Table 3-3 show a high porosity of 0.72 and a low clay content of 0.25. Based on information from the "Geosites in Denmark" website (see references), the Mo Clay is a diatomite. The data

for this formation were not used in the correlations given below because of the low clay content and the substantially different hydro-mechanical character of diatomite as compared with most shales.

## 3.2 THE DEVELOPMENT OF CORRELATIONS TO ASSESS FORMATION PROPERTIES AND CONDITIONS

### 3.2.1 Treatment of Anisotropic Sonic Velocities

The sonic velocity data show in several cases that the compressional sonic velocity, $V_p$, is different normal and parallel to bedding. The effects of anisotropy have to be considered in order to use sonic velocity as an independent variable to correlate with rock properties. Certain properties, such as porosity and bulk density, are not directional. If one formation has isotropic behavior and a single value of $V_p$ and another formation having the same porosity is anisotropic with two different values of $V_p$ depending on direction, which velocity from the anisotropic formation should be used in the correlation? The selection of a single velocity from an anisotropic system appears to be ambiguous. A pragmatic selection that has been found to be suitable is the geometric mean of the parallel, $V_{pp}$, and normal, $V_{pn}$, sonic velocities, $V_{pm} = \sqrt{V_{pn}V_{pp}}$. For anisotropic properties, it could be argued that the velocity and property directions should be used consistently, i.e., the correlation for a property normal to bedding should use the velocity normal to bedding. However, there does not seem to be much advantage to this method over using the geometric mean velocity. Instead, estimates for property values for an orientation parallel to bedding use a scaling factor called the anisotropy factor. The anisotropy factor is computed as the ratio of the velocity parallel and normal to bedding ($V_{pr} = V_{pp}/V_{pn}$) raised to a power that is determined empirically. A property value for a parallel-to-bedding orientation is then computed by multiplying the normal-to-bedding property value by the anisotropy factor.

To implement the approach outlined above requires a means of estimating the bedding-parallel velocities for cases in Tables 3-1 where these data do not exist and for all cases in Table 3-3. Only six of the formations have measurements of sonic velocity normal and parallel to bedding in Table 3-1. A plot of the velocity ratio against the normal velocity is shown in Figure 3-1.

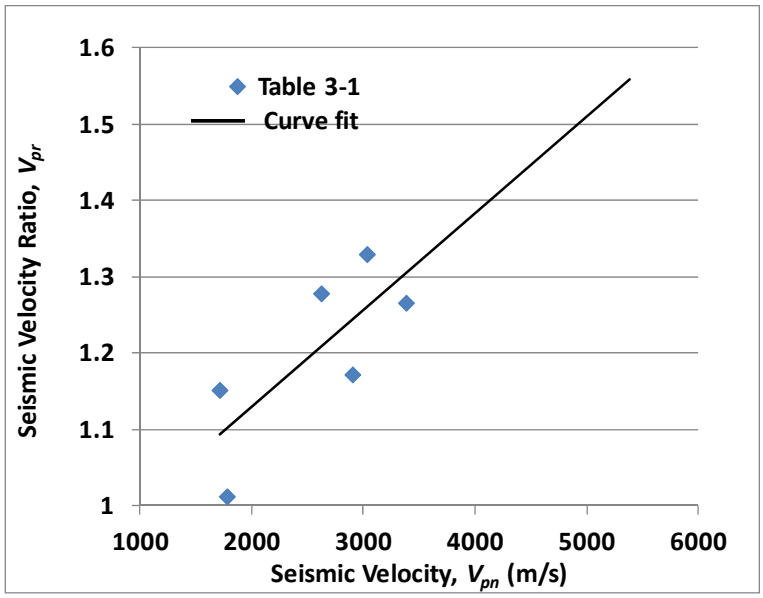


Figure 3-1. Velocity ratio plotted against the sonic velocity normal to bedding.

The values in Table 3-3 are all normal to bedding, but Horsrud (2001) stated that velocities parallel to bedding ranged from 1 to 1.25 times the normal velocity. The normal velocities measured by Horsrud include one sample with a normal velocity of 4818 m/s. Given that this sample has a velocity ratio of 1.25 (or smaller), it seems that the steadily increasing velocity ratio out to 5000 m/s in the normal velocity is not reasonable. To represent this (somewhat fuzzy) information in the correlation, a point is added at 5000 m/s with a velocity ratio of 1.3. Furthermore, the correlation is performed using transformed variables to help account for limiting behavior, similar to that used by Ingram and Urai (1999). The velocity limits are set to a minimum of 1500 m/s, which corresponds to the sonic velocity in water and a maximum of 7000 m/s, which was found to be a suitable upper limit by inspection. The log-transformed variable used as the independent variable for the velocity ratio is $V_{pnt} = -\log\left(\frac{V_{pn}-1500}{7000-V_{pn}}\right)$, which approaches infinity as the velocity goes to 1500 m/s and negative infinity as velocity goes to 7000 m/s. For the velocity ratio itself, the transformed variable is $V_{prt} = -\log\left(\frac{V_{pr}-1}{1.4-V_{pr}}\right)$, which goes to infinity as $V_{pr}$ tends to 1 and to negative infinity as $V_{pr}$ tends to 1.4, which acts as an upper limit for the velocity ratio. The correlation of the velocity ratio with the normal velocity is shown in Figure 3-2. The correlation equation is given in Equation (3-1), which has a root-mean-square error of 0.068 in the velocity ratio. A plot of the correlation in terms of physical variables is shown in Figure 3-3.

$$V_{prt} = 0.4482\, V_{pnt}^2 + 0.3298\, V_{pnt} - 0.4825 \tag{3-1}$$

The correlation was then applied to the values in Tables 3-1 and 3-3 to provide parallel velocities for cases in which a parallel velocity was not available. A normal orientation is assumed for those cases in Table 3-1 in which the orientation of the sonic velocity measurement was not

identified. Given the small data set available to develop the correlation and the weak correlation that has been demonstrated, it is clearly preferable to have measurements for velocities both normal and parallel to bedding rather than relying on the correlation.

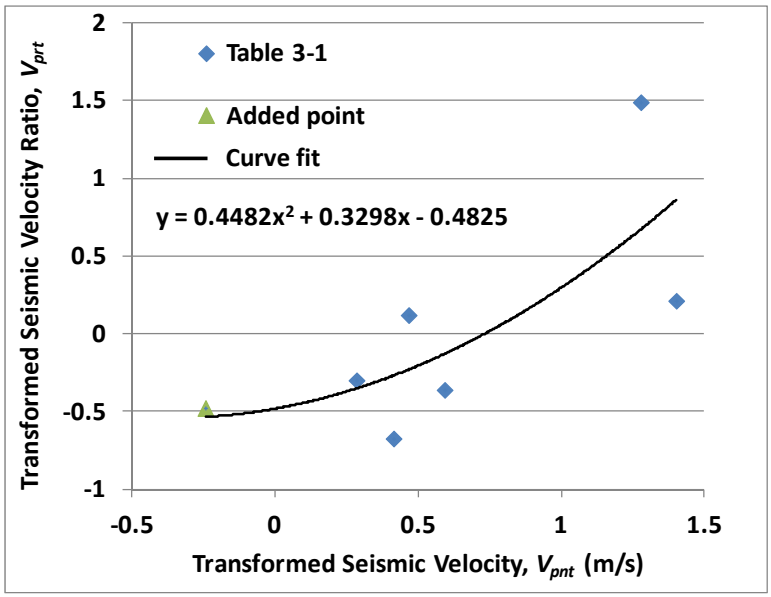


Figure 3-2. Seismic velocity ratio correlation with normal sonic velocity using transformed variables.

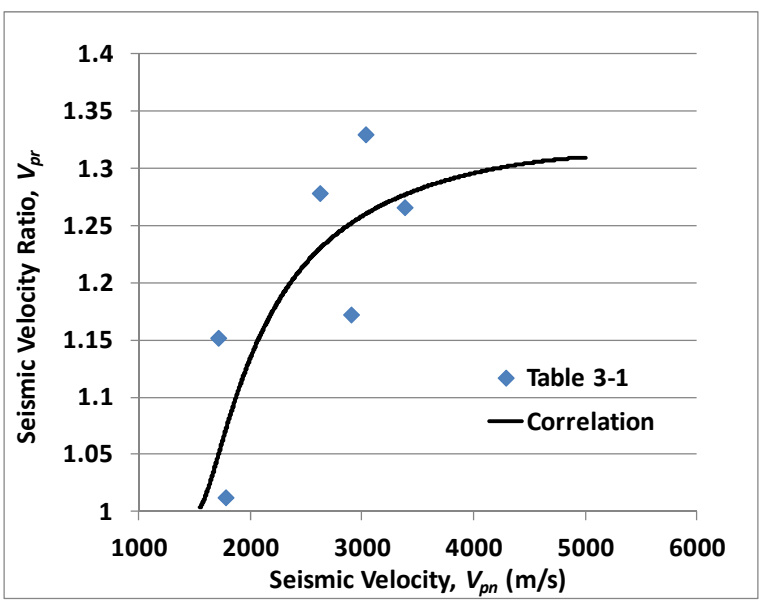


Figure 3-3. Seismic velocity ratio correlation with normal sonic velocity using physical variables.

### 3.2.2 The Porosity – Seismic Velocity Correlation

The relationship between porosity ($\phi$) and $V_p$ was originally investigated by Wyllie et al. (1956; 1958). The correlation was further investigated by Han et al. (1986) for sandstones accounting for the influence of clay content. Horsrud (2001) presented a correlation between $\phi$ and $V_p$ for shales. A similar transformed sonic velocity is used for the porosity correlation as used in Section 3.2.1; however, here the geometric mean of the normal and parallel sonic velocities, $V_{pm}$, is used. The transformed sonic velocity is given by $V_{pmt} = \log\left(\frac{V_{pm}-1500}{7000-V_{pm}}\right)$. The transformed variable used for $\phi$ is $\phi_t = \log\left(\frac{1-\phi}{\phi}\right)$, which goes to negative infinity as porosity goes to 1 and to infinity as porosity goes to 0. The correlation for the transformed porosities and sonic velocities using data from Tables 3-1 and 3-3 is shown in Figure 3-4.

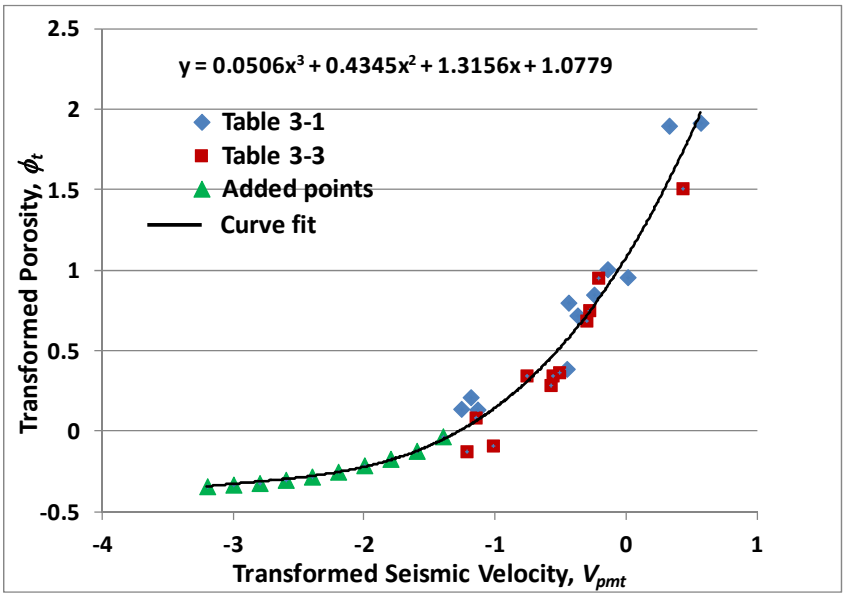


Figure 3-4. Porosity and sonic velocity correlation using transformed variables.

The polynomial correlation tends to result in unreasonable results beyond the limit of the data, and in particular will generate reversals in the velocity-porosity curve at low values of the velocity. The green points in Figure 3-4 are used such that the polynomial correlation remains reasonable for extrapolations at low values of $V_{pmt}$ (which is also for low values of $V_{pm}$) beyond the range of the existing data.

The correlation is given in Equation (3-2), which has a root-mean-square error (RMSE) of 0.056.

$$\phi_t = 0.0506\, V_{pmt}^3 + 0.4345\, V_{pmt}^2 + 1.3156\, V_{pmt} + 1.0779 \qquad (3\text{-}2)$$

The comparison of the correlation with the data using the physical variable is shown in Figure 3-5. The data point from Table 3-3, not used for the correlation shown in Figure 3-5, is for the Mo Clay, as discussed in Section 3.1. The Horsrud (2001) correlation, which is based on the Table 3-3 data, predicts higher values of porosity, particularly at the extremes of the velocity spectrum.

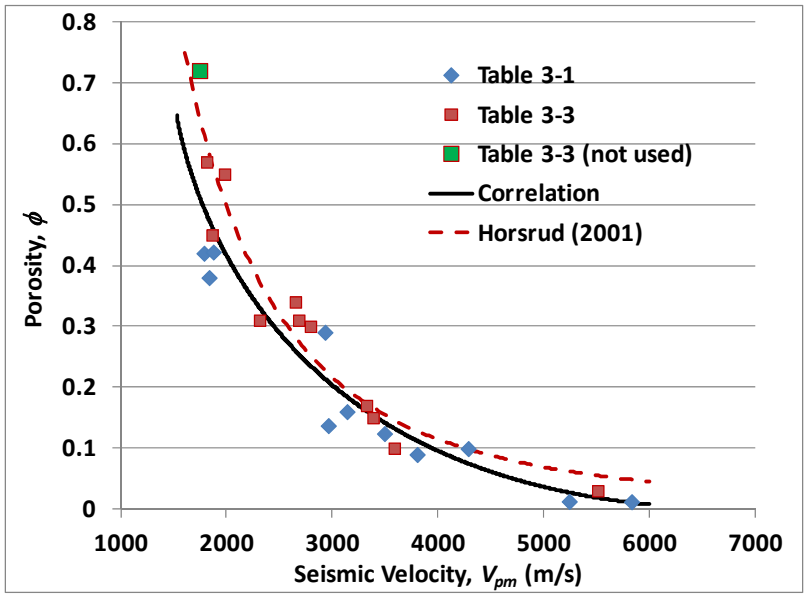


Figure 3-5. Porosity and sonic velocity correlation using physical variables.

### 3.2.3 The Bulk Density – Seismic Velocity Correlation

After finding the relatively strong correlation between $\phi$ and $V_{pm}$, it is reasonable to expect a correlation between the saturated bulk density, $\rho_b$, and $V_{pm}$. The correlation uses the transformed velocity, $V_{pmt}$, described in Section 3.2.2 and a transformed bulk density, $\rho_{bt} = \log\left(\frac{\rho_b - 1000}{2900 - \rho_b}\right)$, where 1000 kg/m$^3$ represents the minimum bulk density (equal to that of water for a porosity of 1) and 2900 kg/m$^3$ represents a maximum bulk density. The data and correlation are shown in Figure 3-6 and the correlation equation is given in Equation (3-3), which has an RMSE of 33 kg/m$^3$ for $\rho_b$. Given the bulk density and the porosity, the grain density, $\rho_g$, may be computed by $\rho_g = \frac{\rho_b - \phi\rho_w}{1-\phi}$, where $\rho_w$ is the density of the resident fluid that saturates the pore space.

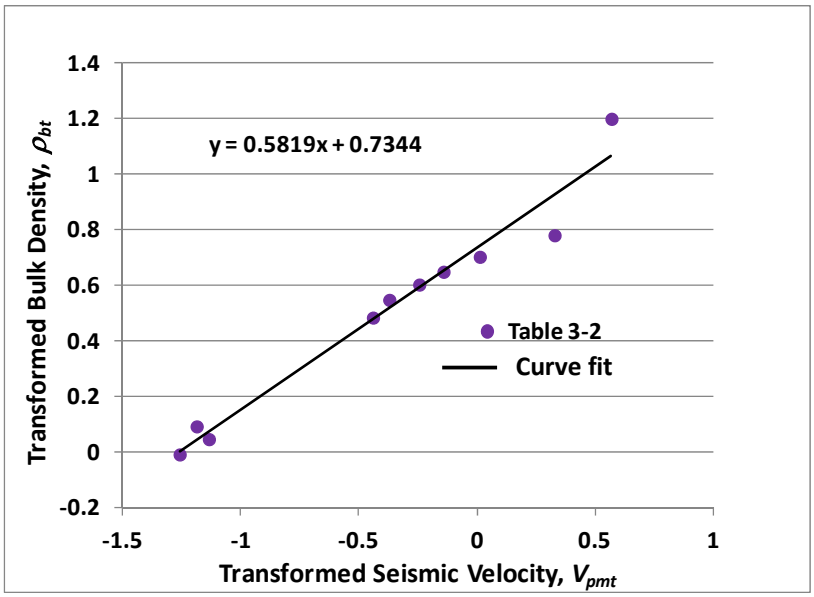


Figure 3-6. Bulk density and sonic velocity correlation using transformed variables.

$$\rho_{bt} = 0.5819\, V_{pmt} + 0.7344 \tag{3-3}$$

The correlation comparison with the data in physical variables is shown in Figure 3-7.

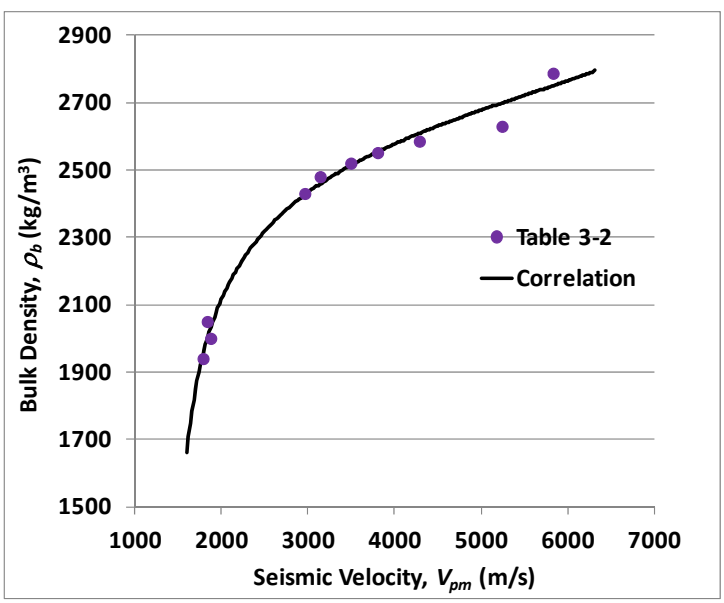


Figure 3-7. Bulk density and sonic velocity correlation using physical variables.

### 3.2.4 The Clay Content – Seismic Velocity Correlation

The behavior of shale formations with respect to compaction and permeability is affected by the clay content of the rock (Yang and Aplin, 2004; 2010). Thus, it is important to establish clay content to carry out additional parameter estimation. This correlation uses the transformed sonic velocity, $V_{pmt}$, described in Section 3.2.2 and the clay content mass fraction, $X$, as shown in Figure 3-8. The correlation function in Equation (3-4) has an RMSE of 0.098. A correlation plot in terms of the physical variables is shown in Figure 3-9. The data point from Table 3-3 that is not used for the correlation shown in Figure 3-9, is for the Mo Clay, as discussed in Section 3.1.

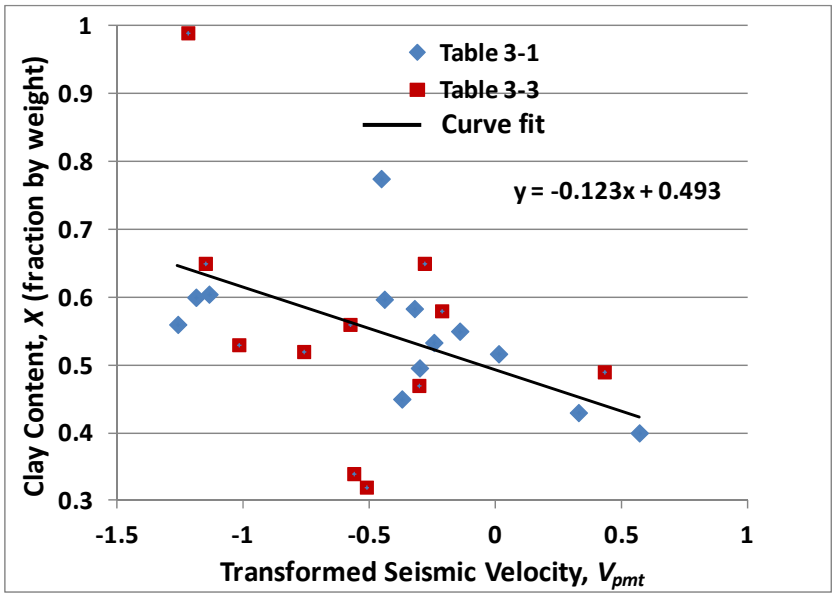


Figure 3-8. Clay content and sonic velocity correlation using transformed sonic velocity.

$$X = -0.123\, V_{pmt} + 0.493 \tag{3-4}$$

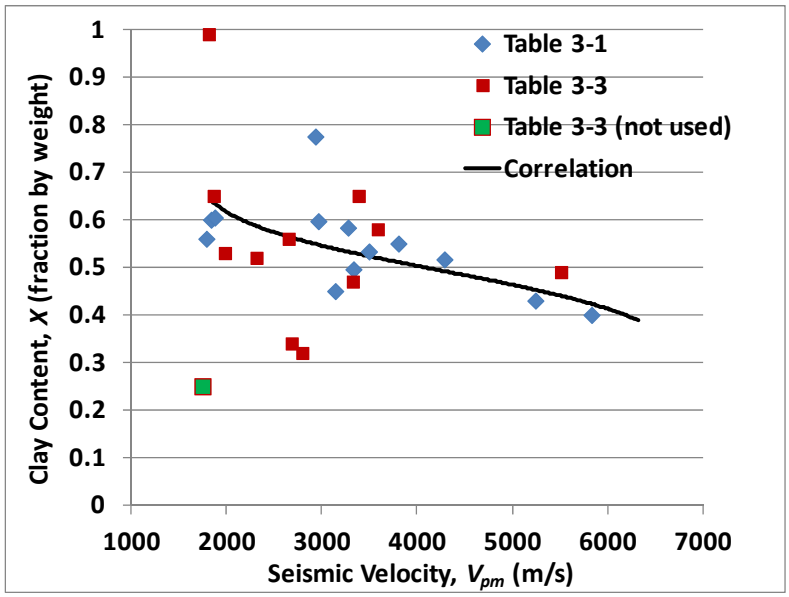


Figure 3-9. Clay content plotted against the physical sonic velocity.

As shown in Figure 3-9, the clay content correlation with sonic velocity is weak. This is expected based on the weak correlation found by Yang and Aplin (2010) between porosity and clay content. On the other hand, more than 85% of the values for clay content fall within the range of 0.4 to 0.65. Another question concerning the correlation is that the clay content values given in Tables 3-1 and 3-3 are the mass fractions of clay minerals, whereas Yang and Aplin (2010) defined the clay content as the mass fraction for grain sizes less than 2μm. Yang and Aplin (2010) demonstrated that the clay mass fraction correlates much more strongly with the Atterberg liquid limit. However, there is some question as to whether this attribute is applicable to stiff clays and shales (Bock 2001).

### 3.2.5 The Permeability – Porosity - Clay Content Correlation

Yang and Aplin (2010) have published a correlation relating bedding-normal permeability ($k$) with $\phi$ and $X_c$ for marine mudstones, where $X_c$ is the mass fraction of grains less than 2 microns in size. The correlation is supported by a large data set of 376 data points covering a wide range of porosity and clay content. The correlation is given by Equation (3-5),

$$\ln(k) = -69.59 - 26.7\,X_c + 44.07\,X_C^{0.5} + (-53.61 - 80.03\,X_c + 132.78\,X_C^{0.5})e + (86.61 + 81.91\,X_c - 163.61\,X_C^{0.5})e^{0.5} \quad (3\text{-}5)$$

where $k$ is the permeability in m$^2$ and $e$ is the void ratio given by $e = \phi/(1-\phi)$. Given limited information concerning $X_c$, the clay mineral mass fraction, $X$, from Section 2.3 is used as a proxy for the clay-size mass fraction, $X_c$.

Permeability estimates from a known value of $V_{pm}$ can be computed using Equation (3-5) by using Equations (3-2) and (3-4) for porosity and clay content, respectively. The results compared with the Table 3-1 bedding-normal permeability data is shown in Figure 3-10.

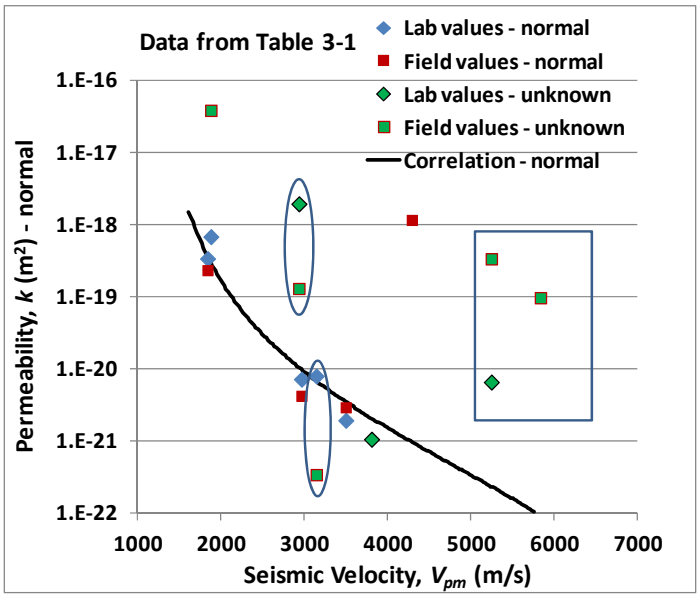


Figure 3-10. Permeability correlation normal to bedding (using Equations 3-2, 3-4, and 3-5) compared with measurements. Note: see text near end of this section concerning ovals and rectangle.

The labeling "normal" and "unknown" in the legend of Figure 3-10 refers to the orientation of the permeability measurement relative to bedding. For quantities like permeability that range over a factor of 10 or more in magnitude, it is better to describe the correlation error in terms of the logarithm of the variable because the magnitude of the error typically scales with the value of the permeability. The RMSE range of the correlation for log permeability relative to the laboratory data normal to bedding is ± 0.21. The RMSE range for $\log(k)$, $\log(k)$ ± 0.21, is equivalent to a range in permeability in which permeability is multiplied by a factor of 1.6 and divided by a factor of 1.6.

The correlation is extended to provide permeability parallel to bedding by scaling the normal to bedding permeability by an anisotropy factor, $A_f$, given by Equation 3-6,

$$A_f = V_{pr}^{\omega} \tag{3-6}$$

where $\omega$ is the empirical anisotropy coefficient and $V_{pr}$ is the parallel to normal sonic velocity ratio. The calibrated value of $\omega$ is 4.6. The RMSE of the correlation for log permeability relative to the laboratory data parallel to bedding is 0.15, or a factor of 1.4 for the permeability. The results are shown in Figure 3-11.

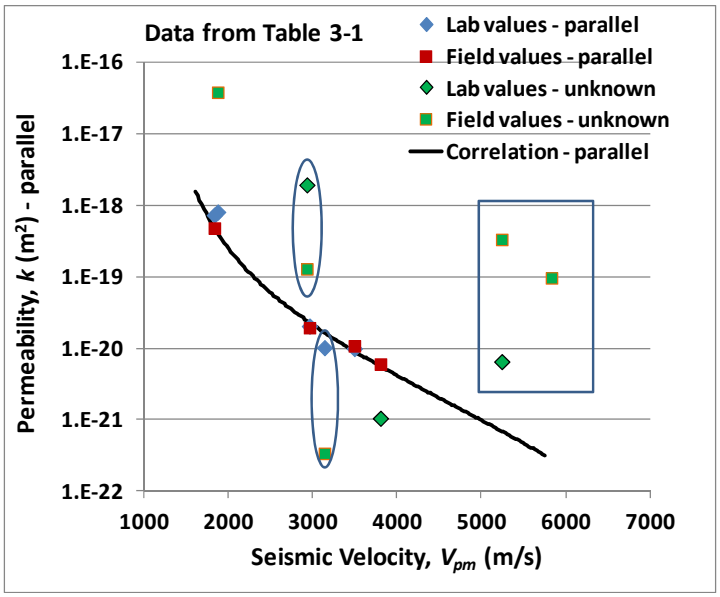


Figure 3-11. Permeability correlation parallel to bedding (using Equations 3-2, 3-3, and 3-4 and 3-6) compared with measurements. Note: see text near end of this section concerning ovals and rectangle.

In Figures 3-10 and 3-11, the estimated permeabilities are close to the lab measurements, with two exceptions: the Spanish Reference Clay and the Palfris Formation at Wellenberg. The points outlined by the blue rectangle are for the Palfris Formation at Wellenberg and the Boda Claystone. These have porosities of approximately 0.01, which lies outside the range of values (0.04 to 0.78) investigated by Yang and Aplin (2010). Four other in-situ measurements also fall far off the correlation line. In-situ measurements can be affected by larger-scale features of the formation and would generally lead to higher permeabilities (Neuzil, 1994). However, two cases circled on Figure 3-10, the Callovo-Oxfordian Clay (the lower oval) and the Spanish Reference Clay (the upper oval), are found to have in-situ permeabilities that are significantly less than the laboratory values. The reason for this behavior is not known. The same two ovals are shown in Figure 3-11. The laboratory value in Figure 3-11 with unknown orientation at a velocity of 3800 m/s is for the Tournemire argillite. This value falls off the correlation line by about a factor of 4; however, it is also shown in Figure 3-10 and appears to be roughly consistent with a normal-to-bedding orientation.

### 3.2.6 The Porosity–Maximum Effective Stress–Clay Content Correlation

With estimates for $\phi$ and $C$, the maximum effective stress ($\sigma_v'$) experienced by the formation can be estimated using the results of Yang and Aplin (2004). Their correlation representing the physical burial compaction of mudstones relates $\phi$, $X_c$, and $\sigma_v'$ is given in Equation (3-7),

$$e = 0.3024 + 1.6867\,X_c + 1.9505\,X_C^2 - (0.0407 + 0.2479\,X_c + 0.3684\,X_C^2)\ln\left(\frac{\sigma_v'}{100}\right) \qquad (3\text{-}7)$$

where $\sigma_v' = \sigma_v - p$ is the maximum effective stress in kPa experienced by the formation, $\sigma_v$ is the total stress, $p$ is the pore-fluid pressure, and $e = \phi/(1-\phi)$ is the void ratio. As for their permeability correlation discussed in Section 2.5, the correlation covers a wide range of $\phi$ and

$X_c$ and is based on a large laboratory data set of 200 values and a much larger data set based on wireline log interpretations consisting of about 3600 data points. The effective stress is evaluated for values up to 40 MPa. As for permeability in Section 2.5, the clay mineral fraction, $X$, is used as a proxy for $X_c$.

Equation (3-7) cannot be compared directly with the data presented in Section 3.1. However, by using Equation (3-7), it is possible to estimate the present-day pore fluid pressure. Pore fluid pressure is a difficult condition to measure in very low permeability formations characteristic of shale rock (Neuzil, 1993). Pore fluid pressures are important for shale rock, however, because they are frequently "abnormal", i.e., not hydrostatic. Abnormal overpressures can mean that the formation is more vulnerable to mechanical damage by fracture. In order to estimate pore fluid pressure, a correlation for the uniaxial compressive strength and its relationship with the overconsolidation ratio are also needed. These correlations and how they can be combined with Equation (3-7) to estimate pore fluid pressure are described in the next two sections.

#### *3.2.6.1 The Uniaxial Compressive Strength – Seismic Velocity Correlation*

The uniaxial compressive strength (UCS) is the compressive load placed on an unconfined rock sample required to cause fracture. A strong correlation has been noted between the UCS and $V_p$ by both Ingram and Urai (1999) and Horsrud (2001) for mudrocks and shales. The correlation is computed using the transformed sonic velocity, $V_{pmt}$, described in Section 3.2.2 and a log-transformed uniaxial compressive strength, $\log(UCS)$. The correlation plot using transformed variables is shown in Figure 3-12. The correlation equation is given by Equation (8) and has an RMSE of 0.13 for $\log(UCS)$, or a factor of 1.3 for $UCS$.

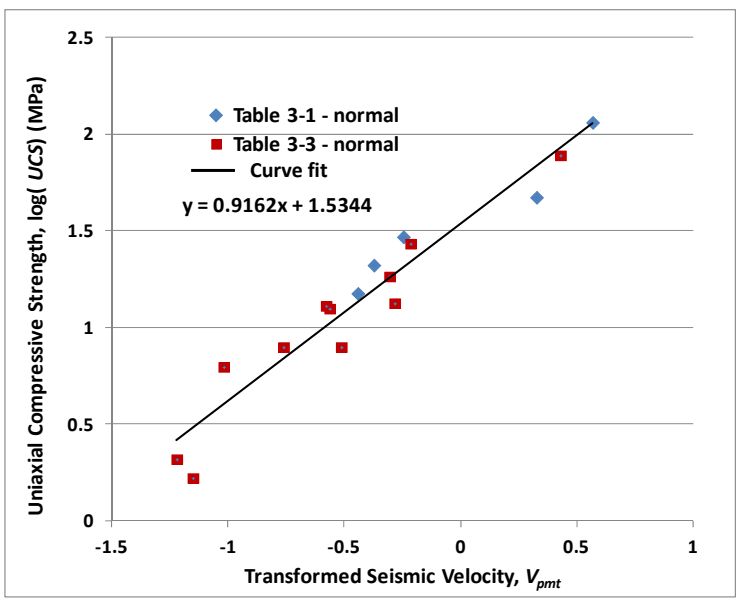


Figure 3-12. Uniaxial compressive strength normal to bedding and sonic velocity correlation using transformed variables.

$$\log(\mathrm{UCS}) = 0.9162\, V_{pmt} + 1.5344 \tag{3-8}$$

The correlation comparison with the data in physical variables is shown in Figure 3-13. In addition to the measured uniaxial compressive strength normal to bedding, data in which the orientation of the measurement is unknown or parallel to bedding are also shown, although these were not used to develop the correlation. The results suggest that anisotropy in uniaxial compressive strength is not strong. The normal value not used from Table 3-3 is for the Mo Clay as discussed in Section 3.1. Correlation plots based on correlations developed by Horsrud (2001) and Ingram and Urai (1999) are also presented in Figure 3-13. The correlation developed here is closer to the Horsrud (2001) correlation, but has some of the character of the Ingram and Urai (1999) correlation at the extremes of the velocity spectrum.

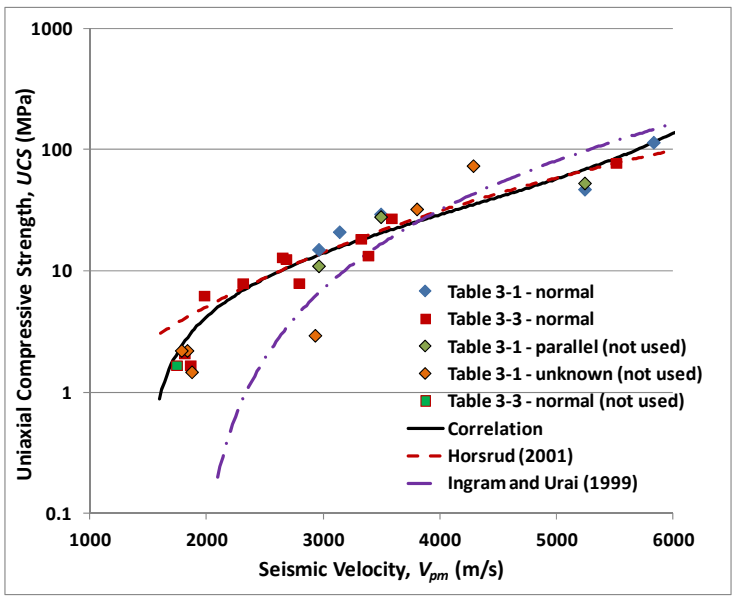


Figure 3-13. Uniaxial compressive strength and sonic velocity correlation using physical variables.

#### *3.2.6.2 Linking the Overconsolidation Ratio to Seismic Velocity*

The overconsolidation ratio (OCR) is the maximum effective stress experienced by a formation divided by the present-day effective stress. Ingram and Urai (1999) proposed the following brittleness index (BRI) for mudrocks,

$$\mathrm{BRI} = \frac{\mathrm{UCS}}{\mathrm{UCS_{NC}}} \tag{3-9}$$

where $\mathrm{UCS_{NC}}$ is the uniaxial compressive strength for a normally-consolidated rock. Normal consolidation means that the present-day effective stress is the maximum effective stress. Ingram and Urai (1999), based on results from Horseman et al. (1986), suggest that $\mathrm{UCS_{NC}}$ can be estimated from the following,

$$\mathrm{UCS_{NC}} = 0.5\sigma_{NC} \tag{3-10}$$

where $\sigma_{NC}$ is the effective stress for normal consolidation at the present-day depth. Using the definitions of bulk density and effective stress, the value of $\sigma_{NC}$ may be computed from the following,

$$\sigma_{NC} = \rho_b g D - p_{hs} \tag{3-11}$$

where $p_{hs}$ is the hydrostatic pressure equal to $\rho_w g D$, $\rho_w$is the density of the pore fluid, $D$ is the present-day burial depth, and $g$ is the acceleration of gravity. This is based on the approximation that the entire stratigraphic column can be represented by the formation bulk density, $\rho_b$, and that the pore fluid density is known or can be reasonably approximated. Therefore, using Equations (3-8), (3-10) and (3-11), the brittleness index in Equation (3-9) may be computed. Nygård et al. (2006) proposed that the brittleness index could be related to the overconsolidation ratio by the following:

$$\mathrm{OCR} = \mathrm{BRI}^{\kappa} \tag{3-12}$$

Nygård et al. (2006) found a value of ω of about 1.1, however, evaluations conducted here have found a value of 0.7 is better suited for the determination of pore pressure. Using Equation (3-12) to compute the OCR and Equation (3-7) to compute the maximum effective stress, $\sigma_v'$, the present-day effective stress, $\sigma_{pd}$, is,

$$\sigma_{pd} = \frac{\sigma_v'}{\mathrm{OCR}} \tag{3-13}$$

The present-day effective stress is also given by,

$$\sigma_{pd} = \rho_b g D - p \tag{3-14}$$

Equation (3-14) may be used to determine the present-day pore fluid pressure, $p$. The pore fluid overpressure, $p_{op} = p - p_{hs}$, is the difference between the pore fluid pressure and the hydrostatic pressure.

BRI is also important for evaluating whether the rock is subject to brittle or ductile failure. Ingram and Urai (1999) determined that the failure mode is expected to be brittle for a BRI greater than 2 and is expected to behave as a ductile material at lower values of the BRI.

### 3.2.7 Young's Modulus - Seismic Velocity Correlations

Data for Young's modulus normal to bedding ($E_n$) and parallel to bedding ($E_p$) are given in Tables 3-2 and 3-3. The plot of the log-transformed $E_n$ against the transformed sonic velocity, $V_{pmt}$, described in Section 3.2.2 is shown in Figure 3-14. The polynomial correlation tends to estimate unreasonable results beyond the limit of the data, and in particular will generate reversals in the velocity-Young's modulus curve at high values of the velocity. The green points in Figure 3-15 are used such that the polynomial correlation remains reasonable for extrapolations at high values of $V_{pmt}$ (which is also for high values of $V_{pm}$) beyond the range of the existing data. The correlation is given in Equation (3-15) and has an RMSE of 0.25 for $\log(E_n)$ or a factor of 1.8 for $E_n$.

$$\log(E_n) = 0.111\, V_{pmt}^3 - 0.3395\, V_{pmt}^2 + 0.8125\, V_{pmt} + 0.8228 \qquad (3\text{-}15)$$

The correlation is shown in physical variables along with the data in Figure 3-15. The "not used" data point from Table 3-3 is the Mo Clay as discussed in Section 3.1. Figure 3-15 also presents the correlation developed by Horsrud (2001). The correlation given by Equation (3-15) lies close to the Horsrud (2001) correlation, except at the low end of the velocity spectrum.

The correlation for Young's modulus parallel to bedding is developed using the anisotropy coefficient as described in Section 2.5 for permeability. The calibrated anisotropy coefficient, $\omega$, is 4.8. The resulting comparison with data is shown in Figure 3-16. The RMSE for the parallel Young's modulus correlation is 0.49 for $\log(E_n)$ or a factor of 3.1 for $E_p$. The large error in this case is driven mainly by the large relative errors incurred at low values of Young's modulus where the correlation curve becomes steep.

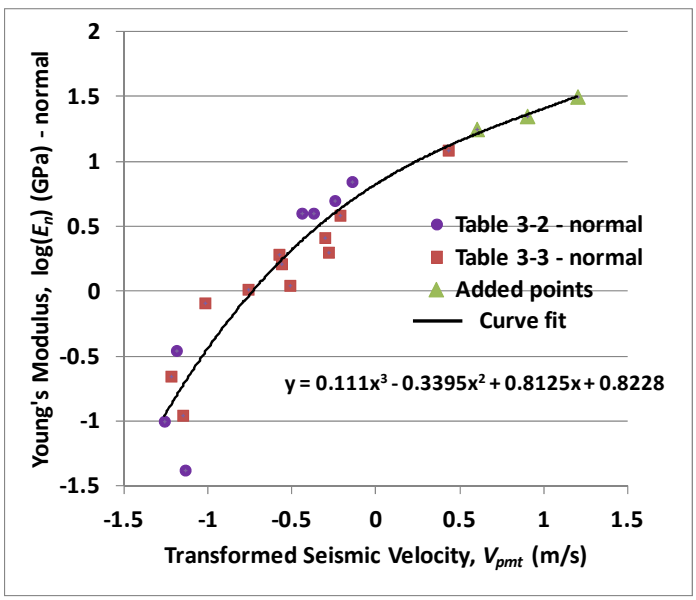


Figure 3-14. Correlation for Young's modulus normal to bedding with sonic velocity using transformed variables.

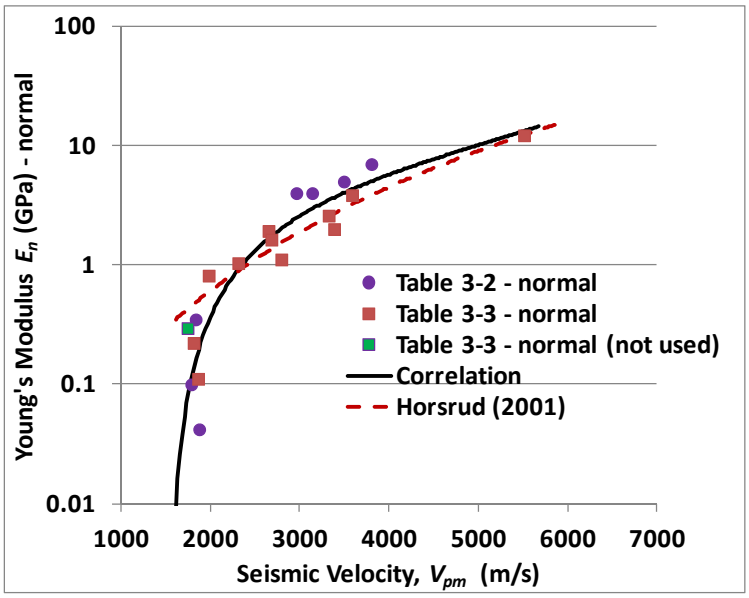


Figure 3-15. Correlation for Young's modulus normal to bedding with sonic velocity using physical variables.

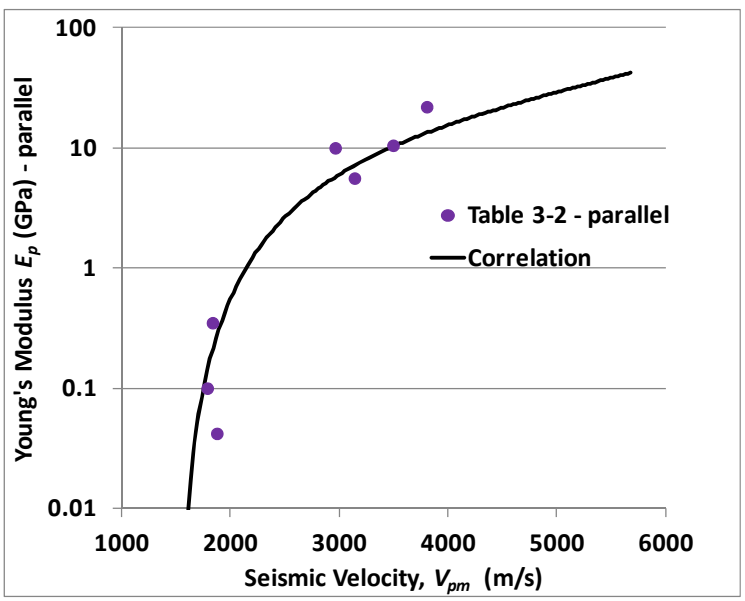


Figure 3-16. Correlation for Young's modulus parallel to bedding with sonic velocity.

### 3.2.8 Shear Modulus – Seismic Velocity Correlation

Data for shear modulus ($G$) are given in Tables 3-2 and 3-3. Insufficient data were available to assess anisotropic effects, with data limited to either normal-to-bedding or unknown orientation. The plot of the log-transformed $G$ against the transformed sonic velocity, $V_{pmt}$, described in

Section 3.2.2, is shown in Figure 3-17. The polynomial correlation tends to result in unreasonable results beyond the limit of the data, and in particular will generate reversals in the velocity-shear modulus curve at high values of the velocity. The green points in Figure 3-17 are used such that the polynomial correlation remains reasonable for extrapolations to high values of $V_{pmt}$ (which is also for high values of $V_{pm}$) beyond the range of the existing data. The correlation is given in Equation (3-16) and has an RMSE of 0.25 for $\log(G)$ or a factor of 1.8 for $G$.

$$\log(G) = 0.1556\, V_{pmt}^3 - 0.4077\, V_{pmt}^2 + 0.7162\, V_{pmt} + 0.4279 \qquad (3\text{-}16)$$

The correlation is shown in physical variables along with the data in Figure 3-18. The "not used" data point from Table 3 is the Mo Clay as discussed in Section 3.1. As for Young's modulus, the correlation developed here lies close to the Horsrud (2001) correlation, except at the low end of the velocity spectrum.

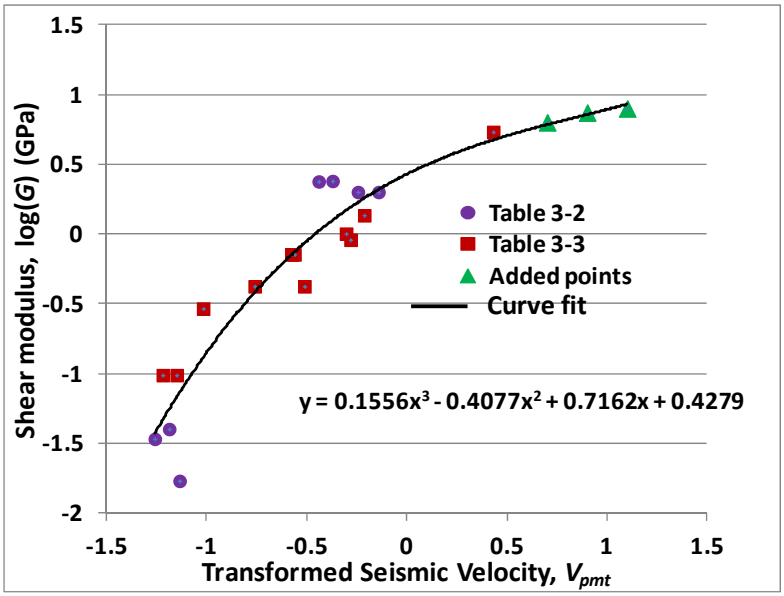


Figure 3-17. Correlation for shear modulus with sonic velocity using transformed variables.

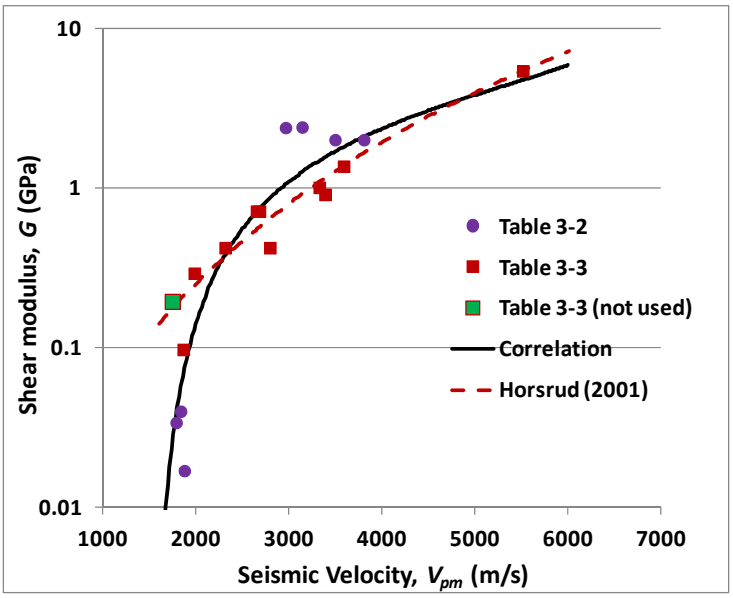


Figure 3-18. Correlation for shear modulus with sonic velocity using physical variables.

### 3.2.9 Poisson's Ratio - Seismic Velocity Correlation

Data for Poisson's ratio are given in Table 3-2. Insufficient data were available to assess anisotropic effects. Furthermore, orientation information was generally unavailable; therefore, the data and results are treated as effectively isotropic. The plot of the transformed Poisson's ratio, $\upsilon_t = \log\left(\frac{0.5-\upsilon}{\upsilon}\right)$, against the transformed sonic velocity, $V_{pmt}$, as described in Section 3.2.2, is shown in Figure 3-19. The correlation equation is given in Equation (3-19) and has an RMSE of 0.077 for $\upsilon$. The correlation did not include the value for the Ypresian Clay from Table 3-2. The plot of the correlation with the data using physical variables in Figure 3-20 shows that the Ypresian Clay (indicated by the light green-filled symbol) deviated significantly from the trend of the other formations. It is possible that the discrepancy is caused by the measurement method. The Ypresian Clay Poisson's ratio was determined from a uniaxial compression test (Piña-Diaz 2011) that would not maintain undrained conditions. This contrasts with the measurement reported for the Boom Clay ($\upsilon$ = 0.425), also at a low sonic velocity similar to the Ypresian Clay, which was for undrained conditions.

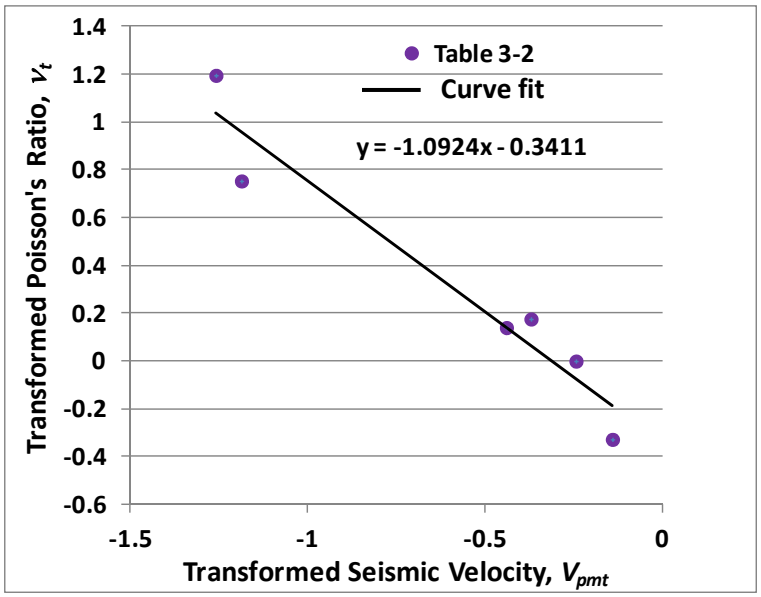


Figure 3-19. Correlation for Poisson's ratio with sonic velocity using transformed variables.

$$v_t = -1.0924\, V_{pmt} - 0.3411 \tag{3-17}$$

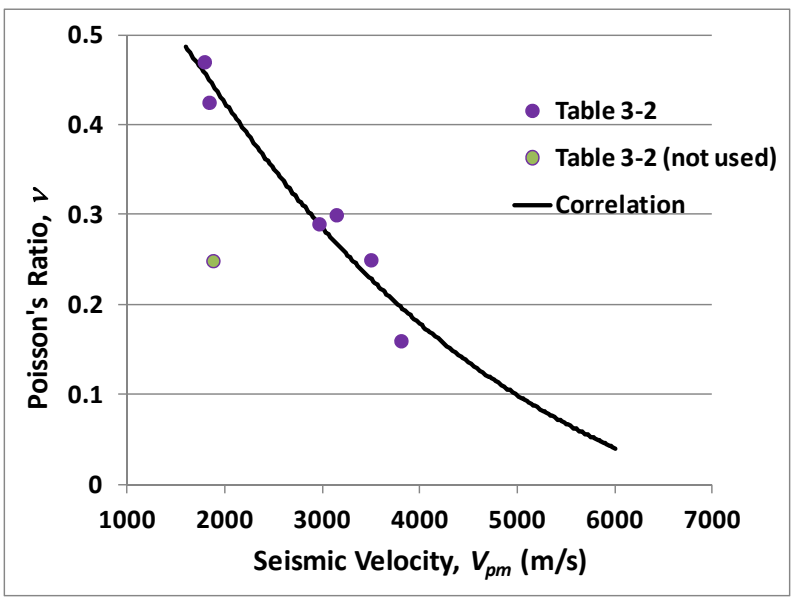


Figure 3-20. Correlation for Poisson's ratio with sonic velocity using physical variables.

### 3.2.10 Cohesive Strength - Seismic Velocity Correlations

Cohesive strength is a parameter in the Mohr-Coulomb model for rock failure under shear stress. Data for cohesive strength ($c$) are given in Table 3-2. The plot of the log-transformed cohesive strength normal to bedding, $\log(c_n)$ against the transformed sonic velocity $V_{pmt}$, as described in

Section 3.2.2, is shown in Figure 3-21. The correlation given in Equation (3-18) has an RMSE for $\log(c_n)$ of 0.16, or a factor of 1.5 for $c_n$.

$$\log(c_n) = 1.1461\, V_{pmt} + 0.7737 \tag{3-18}$$

The correlation for cohesive strength normal to bedding against sonic velocity using physical variables is shown in Figure 3-22. The cohesive strength parallel to bedding was developed by using the anisotropy factor discussed in Section 3.2.5. The calibrated anisotropy parameter,, is 3.5. The correlation for cohesive strength parallel to bedding is shown in Figure 3-23 and has an RMSE of for $\log(c_p)$ of 0.14, or a factor of 1.4 for $c_p$. Although the data are limited for these correlations, Wong and Kenter (1993) have also suggested that cohesive strength and the sonic velocity may be correlated. However, further work is needed to better establish these correlations.

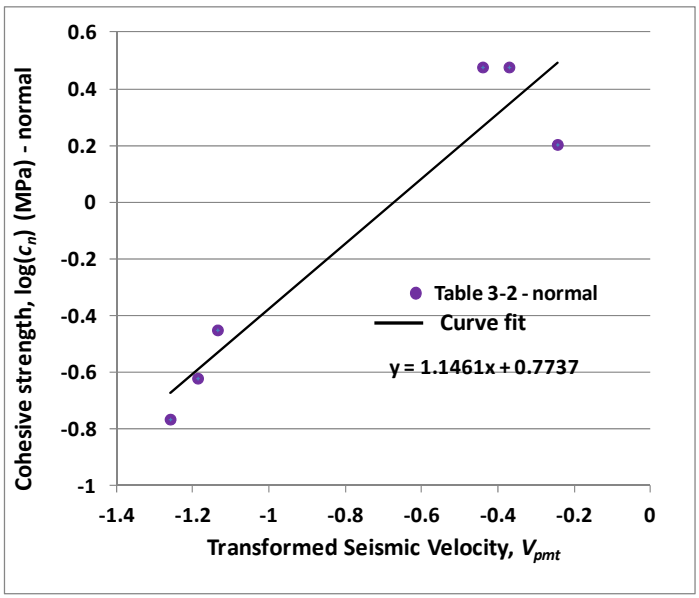


Figure 3-21. Correlation for cohesive strength normal to bedding with sonic velocity using transformed variables.

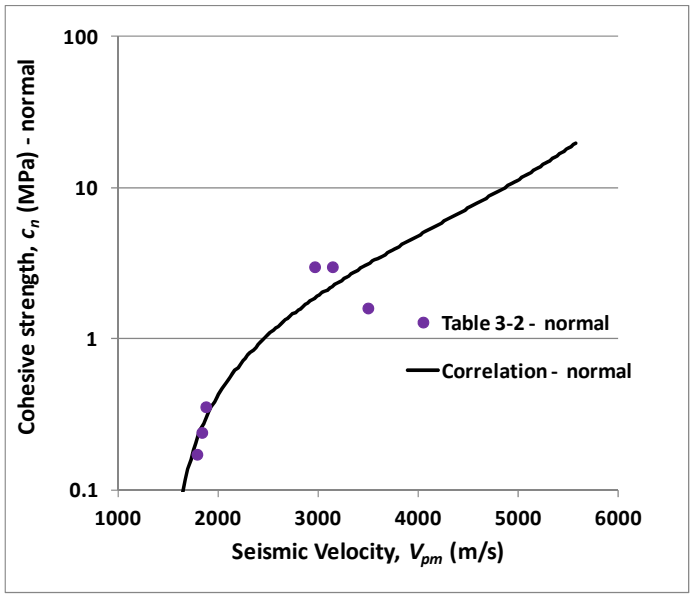


Figure 3-22. Correlation for cohesive strength normal to bedding with sonic velocity using physical variables.

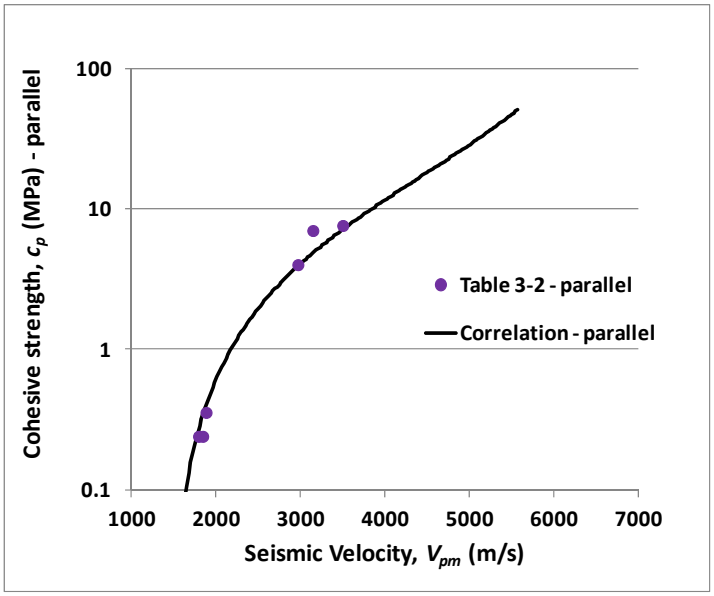


Figure 3-23. Correlation for cohesive strength parallel to bedding with sonic velocity.

### 3.2.11 Friction Angle - Seismic Velocity Correlation

Friction angle is a parameter in the Mohr-Coulomb model for rock failure under shear stress. Data for friction angle ($\varphi$) are given in Table 3-2. Insufficient data were available to assess anisotropic effects. Furthermore, orientation information was generally unavailable; therefore, the results are treated as effectively isotropic. The plot of $\varphi$ against the transformed sonic

velocity $V_{pmt}$, as described in Section 3.2.2, is shown in Figure 3-24. The correlation given in Equation (3-19) has an RMSE of 0.85 degrees for $\varphi$.

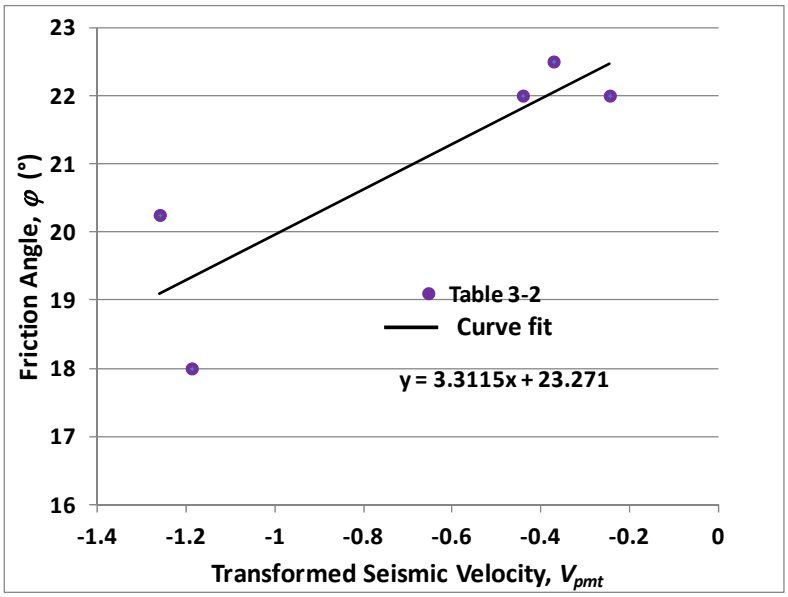


Figure 3-24. Correlation for friction angle with sonic velocity using transformed variables.

$$\varphi = 3.3115\, V_{pmt} + 23.271 \tag{3-19}$$

The correlation for cohesive strength normal to bedding against sonic velocity using physical variables is shown in Figure 3-25. As in Section 3.2.9 for Poisson's ratio, the Ypresian Clay is an outlier that was not used in the friction angle correlation. It is shown as the point not used in Figure 3-25. This appears to be in a range of sonic velocities where friction angle changes rapidly, making an assessment of the friction angle problematic at velocities below 2000 m/s. Horsrud (2001) developed a correlation with friction angle but did not present any of the data behind the correlation. Horsrud's (2001) observation that the friction angle of shale tends to lie between 45° and 60° is not consistent with the available data found to develop the correlation in this report. Further work is needed to establish the friction angle correlation with sonic velocity, however, Wong and Kenter (1993) also suggested that friction angle and the sonic velocity may be correlated.

It is interesting to note that Ingram and Urai (1999) found a correlation between the specific surface area of shale and the friction angle. The specific surface area is a measure of the total hydratable surface in a rock. If the friction angle correlation with velocity is found to hold more generally, then it may be possible to obtain surface area from the sonic velocity. This is useful for geochemical models involving reactions with the rock surface.

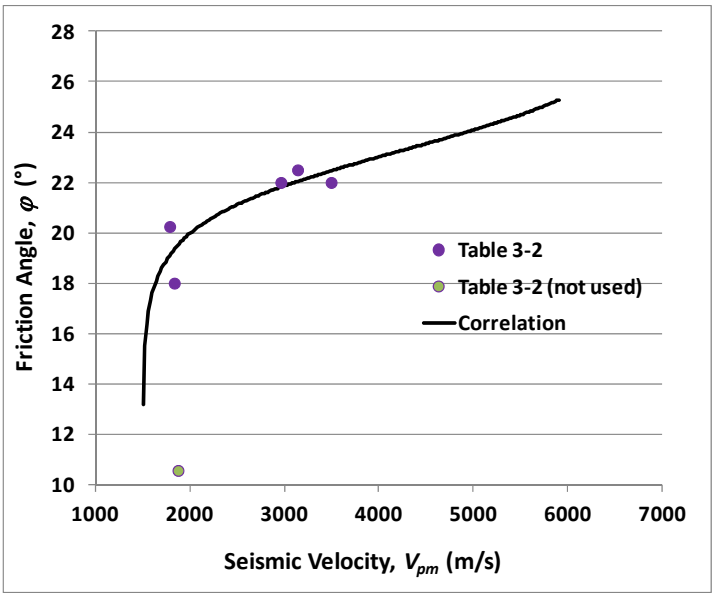


Figure 3-25. Correlation for friction angle with sonic velocity using physical variables.

### 3.2.12 Tensile Strength – Seismic Velocity Correlations

Data for tensile strength ($\tau$) are given in Table 3-2. The plot of the log-transformed tensile strength normal to bedding, $\log(\tau_n)$ against the transformed sonic velocity, $V_{pmt}$, as described in Section 3.2.2, is shown in Figure 3-26. The correlation given in Equation (3-20) has an RMSE for $\log(\tau_n)$ of 0.034, or a factor of 1.1 for $\tau_n$.

$$\log(\tau_n) = 1.1166\, V_{pmt} + 0.3164 \tag{3-20}$$

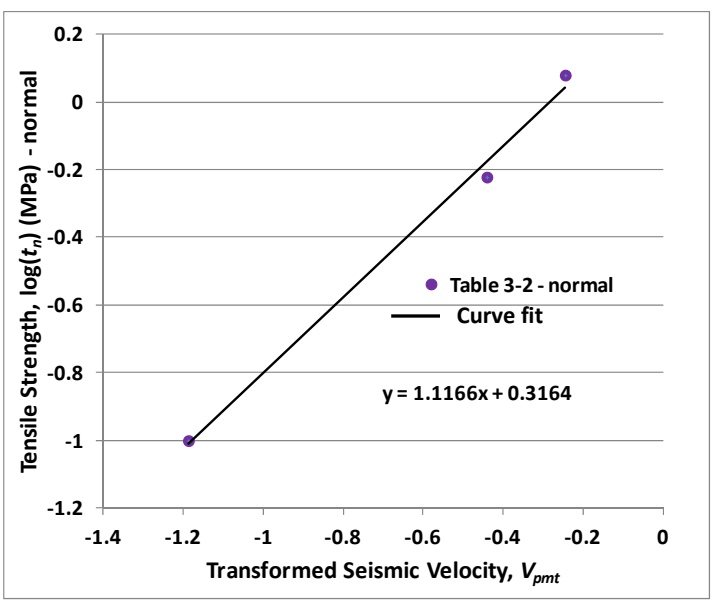


Figure 3-26. Correlation for tensile strength normal to bedding with sonic velocity using transformed variables.

The correlation for tensile strength normal to bedding against sonic velocity using physical variables is shown in Figure 3-27. The tensile strength parallel to bedding was developed by using the anisotropy factor discussed in Section 3.2.5. The calibrated anisotropy parameter,, is 3.3. The correlation for cohesive strength parallel to bedding is shown in Figure 3-28 and has an RMSE for $\log(\tau_p)$ of 0.19, or a factor of 1.5 for $\tau_p$.

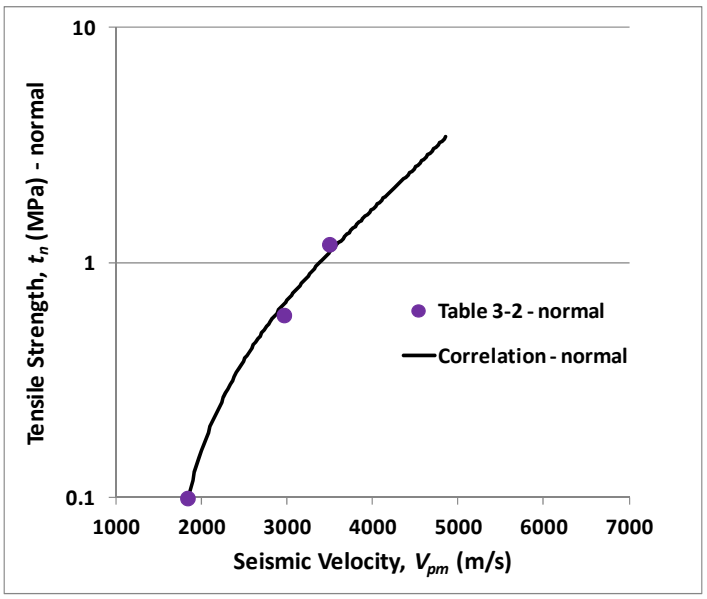


Figure 3-27. Correlation for tensile strength normal to bedding with sonic velocity using physical variables.

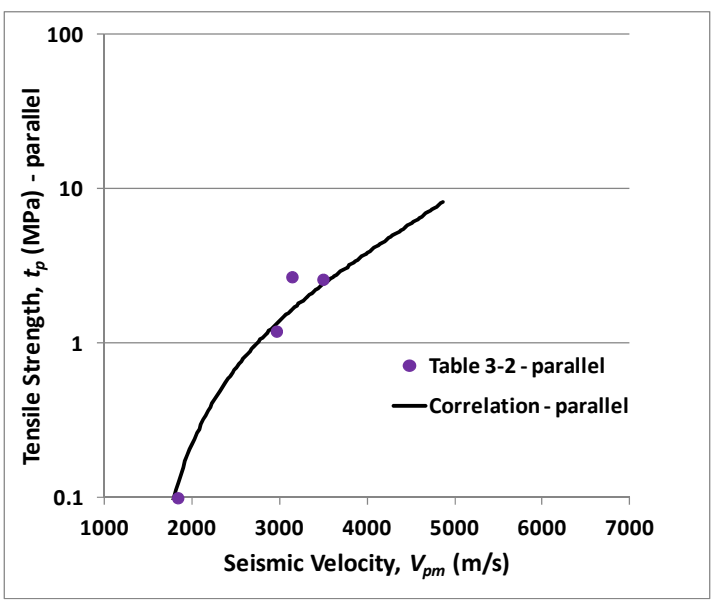


Figure 3-28. Correlation for tensile strength parallel to bedding with sonic velocity.

## 3.3 APPLICATION TO US SHALE FORMATIONS

The correlations developed in Section 3.2 are now applied to evaluate properties of specific sites in the United States. The formations analyzed are the Barnett shale, Haynesville shale, Pierre shale, New Albany, Antrim, Eagle Ford, Marcellus, Woodford, and Monterey. The locations of the various shale formations are shown in Figure 3-29.

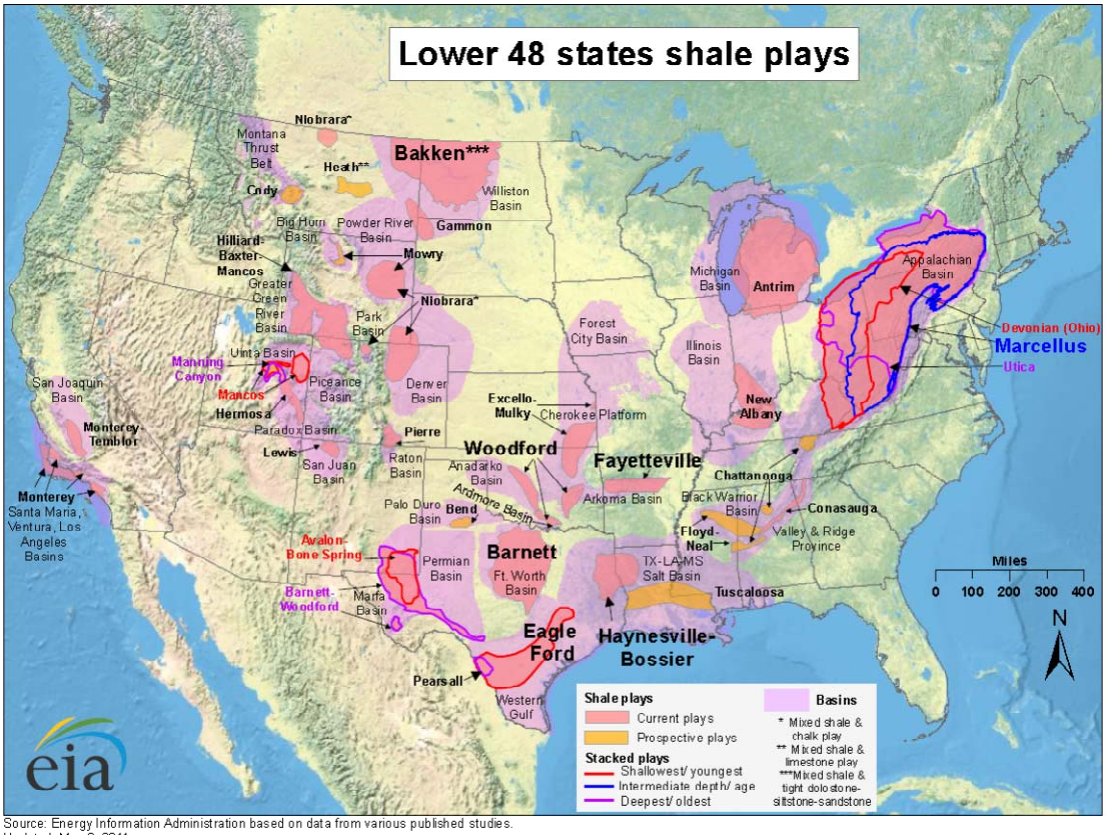


Source: Energy Information Administration based on data from various published studies.
Updated: May 9, 2011

Figure 3-29. Map of U.S. shale gas and shale oil plays (EIA 2011).

### 3.3.1 Inputs

The correlation inputs are the normal and parallel sonic velocities and an average formation depth. As for the development of correlations described in Section 3.2, if the velocity parallel to bedding is not available, it is estimated using the velocity ratio correlation given by Equation (3-1). Table 3-4 gives the requisite inputs for the formations. The formation water density is also an input, however, for the current analysis, a fresh water density of 1000 kg/m$^3$ was assumed.

Table 3-4. Inputs for Properties Estimation.

| Formation | $V_{pn}$ (m/s) | $V_{pp}$ (m/s) | $D$ (m) |
|---|---|---|---|
| Barnett Shale | 4031[1] | NA | 1000[2] |
| Haynesville Shale | 3628[1] | NA | 3000[3] |
| Pierre Shale (1) | 2164[4] | 2243[4] | 152[4] |
| Pierre Shale (2) | 3140[5] | 3768[5] | 1520[5] |
| New Albany Shale | 3600[6] | 4500[6] | 520[7] |
| Antrim Shale | 3174[8] | 4057[8] | 328[8] |
| Eagle Ford Shale | 4016[9] | 4083[9] | 3234[9] |
| Marcellus Shale | 3500[10] | NA | 1920[10] |
| Woodford Shale | 4008[11] | NA | 1220[11] |
| Monterey Shale | 4844[12] | 5310[12] | 2.7[12] |

Sources: [1] Montaut (2012); [2] Bruner and Smosna (2011); [3] Nunn (2012); [4] McDonal et al. (1958); [5] Tosaya (1982); [6] Johnston and Christensen (1995); [7] CNX/GTI (2008); [8] Liu (1997); [9] Sondhi (2011); [10] Hardage (2013); [11] Verma et al. (2013); [12] Liu (1994)

### 3.3.2 Correlations Results

With the sonic velocities from Section 3.3.1, the correlations from Section 3.2 may be used to compute hydrological and geomechanical parameters. These results are shown in Table 3-5. Outputs shaded in blue are rock parameters, while outputs shaded in rose are formation conditions (e.g., effective stress, brittleness index, and overconsolidation ratio) that lead to the estimation of pore pressure.

Table 3-5. Estimated Parameters Using Seismic Velocity Correlations from Section 3.2.

| Parameters | Barnett Shale | Haynesville Shale | Pierre Shale (1) | Pierre Shale (2) | New Albany Shale |
|---|---|---|---|---|---|
| **Inputs** (from Table 4) | | | | | |
| $V_{pn}$ (m/s) | 4031 | 3628 | 2164 | 3140 | 3600 |
| $V_{pp}$ (m/s) | NA | NA | 2243 | NA | 4500 |
| $D$(m) | 1000 | 3000 | 152 | 1524 | 518 |
| **Outputs** | | | | | |
| $V_{pp}$ (m/s) | 5226 | 4665 | 2530 | 3975 | 4626 |
| $\phi$ | 0.055 | 0.084 | 0.36 | 0.13 | 0.094 |
| $e$ | 0.059 | 0.092 | 0.56 | 0.15 | 0.103 |
| $\rho_b$ (kg/m$^3$) | 2640 | 2590 | 2220 | 2530 | 2580 |
| $\rho_{bd}$ (kg/m$^3$) | 2580 | 2510 | 1860 | 2400 | 2490 |
| $\rho_g$ (kg/m$^3$) | 2640 | 2600 | 2410 | 2550 | 2590 |
| $X$ (fraction) | 0.48 | 0.50 | 0.60 | 0.52 | 0.50 |
| $k_n$(m$^2$) | 6.0E-22 | 1.2E-21 | 7.4E-20 | 2.9E-21 | 1.4E-21 |
| $k_p$(m$^2$) | 1.8E-21 | 3.6E-21 | 8.6E-20 | 8.8E-21 | 3.6E-21 |
| UCS (MPa) | 43 | 32 | 5.9 | 22 | 29 |
| $E_n$ (GPa) | 8.1 | 6.3 | 0.70 | 4.3 | 5.8 |
| $E_p$ (GPa) | 24 | 18 | 0.81 | 12.8 | 14 |
| $G$ (GPa) | 3.2 | 2.5 | 0.29 | 1.7 | 2.4 |
| $\upsilon$ | 0.13 | 0.17 | 0.39 | 0.22 | 0.18 |
| $c_n$ (MPa) | 8.0 | 5.5 | 0.66 | 3.4 | 4.9 |
| $c_p$ (MPa) | 20 | 14.0 | 0.7 | 8.8 | 11 |
| $\varphi$ (degrees) | 24 | 23 | 21 | 23 | 23 |
| $\tau_n$ (MPa) | 2.8 | 1.9 | 0.24 | 1.2 | 1.7 |
| $\tau_p$ (MPa) | 6.6 | 4.6 | 0.27 | 2.9 | 3.6 |
| $\sigma'_v$ (MPa) | 48 | 41 | 9.3 | 33 | 40 |
| $\sigma_{NC}$ (MPa) | 16 | 47 | 1.8 | 23 | 8.0 |
| $UCS_{NC}$ (MPa) | 8.0 | 23 | 0.9 | 11 | 4.0 |
| BRI | 5.4 | 1.4 | 6.5 | 1.9 | 7.3 |
| OCR | 3.3 | 1.2 | 3.7 | 1.6 | 4.0 |
| $\sigma_{pd}$ (MPa) | 15 | 33 | 2.5 | 21 | 10 |
| $p$ (MPa) | 11 | 43 | 0.79 | 17 | 3 |
| $p_{hs}$ (MPa) | 9.8 | 29 | 1.5 | 15 | 5.1 |
| $p_{op}$ (MPa) | 1.45 | 14 | -0.70 | 2.0 | -1.8 |

Table 3-5 (continued). Estimated Parameters Using Seismic Velocity Correlations from Section 3.2.

| Parameters | Antrim Shale | Eagle Ford Shale | Marcellus Shale | Woodford Shale | Monterey Shale |
|---|---|---|---|---|---|
| **Inputs** (from Table 4) | | | | | |
| $V_{pn}$ (m/s) | 3174 | 4016 | 3500 | 4008 | 4844 |
| $V_{pp}$ (m/s) | 4057 | 4843 | NA | NA | 5310 |
| $D$(m) | 328 | 3234 | 1920 | 1219 | 2.7 |
| **Outputs** | | | | | |
| $V_{pp}$ (m/s) | 4024 | 5206 | 4485 | 5195 | 6339 |
| $\phi$ | 0.13 | 0.067 | 0.10 | 0.057 | 0.033 |
| $e$ | 0.15 | 0.071 | 0.11 | 0.060 | 0.035 |
| $\rho_b$ (kg/m$^3$) | 2530 | 2620 | 2580 | 2640 | 2680 |
| $\rho_{bd}$ (kg/m$^3$) | 2390 | 2550 | 2480 | 2580 | 2650 |
| $\rho_g$ (kg/m$^3$) | 2550 | 2630 | 2590 | 2640 | 2680 |
| $X$ (fraction) | 0.52 | 0.49 | 0.50 | 0.48 | 0.46 |
| $k_n$(m$^2$) | 2.9E-21 | 8.0E-22 | 1.5E-21 | 6.2E-22 | 3.0E-22 |
| $k_p$(m$^2$) | 8.1E-21 | 1.7E-21 | 4.5E-21 | 1.8E-21 | 4.4E-22 |
| UCS (MPa) | 22 | 38 | 29 | 43 | 60 |
| $E_n$ (GPa) | 4.3 | 7.3 | 5.7 | 8.0 | 10.4 |
| $E_p$ (GPa) | 11 | 15 | 17 | 23 | 15 |
| $G$ (GPa) | 1.8 | 2.9 | 2.3 | 3.1 | 3.9 |
| $\upsilon$ | 0.22 | 0.14 | 0.18 | 0.13 | 0.094 |
| $c_n$ (MPa) | 3.4 | 6.8 | 4.8 | 7.8 | 12 |
| $c_p$ (MPa) | 8.0 | 13 | 12.5 | 20 | 17 |
| $\varphi$ (degrees) | 23 | 23 | 23 | 24 | 24 |
| $\tau_n$ (MPa) | 1.2 | 2.4 | 1.7 | 2.7 | 4.1 |
| $\tau_p$ (MPa) | 2.7 | 4.4 | 4.1 | 6.5 | 5.6 |
| $\sigma'_v$ (MPa) | 33 | 45 | 39 | 47 | 53 |
| $\sigma_{NC}$ (MPa) | 4.9 | 51 | 30 | 20 | 0.045 |
| $UCS_{NC}$ (MPa) | 2.5 | 26 | 15 | 9.8 | 0.023 |
| BRI | 8.9 | 1.5 | 2.0 | 4.4 | 2700 |
| OCR | 4.6 | 1.3 | 1.6 | 2.8 | 250.0 |
| $\sigma_{pd}$ (MPa) | 7 | 34 | 25 | 17 | 0.21 |
| $p$ (MPa) | 1.01 | 49 | 24 | 15 | -0.14 |
| $p_{hs}$ (MPa) | 3.2 | 32 | 19 | 12 | 0.027 |
| $p_{op}$ (MPa) | -2.2 | 17 | 5.2 | 2.7 | -0.17 |

**$V_{pn}$: compressional sonic velocity normal to bedding; $V_{pp}$: compressional sonic velocity parallel to bedding; $D$: present-day formation depth; $\phi$: porosity; $e$: void ratio; $\rho_b$: brine-saturated bulk density; $\rho_{bd}$: dry bulk density; $\rho_g$: grain density; $X$: mass fraction of clay minerals; $k_n$: brine permeability normal to bedding; $k_p$: brine permeability parallel to bedding; UCS: uniaxial compressive strength normal to bedding; $E_n$: Young's modulus normal to bedding; $E_p$: Young's modulus parallel to bedding; $G$: shear modulus normal to bedding;**

**$\boldsymbol{v}$: Poisson's ratio (isotropic); $\boldsymbol{c_n}$: cohesive strength normal to bedding; $\boldsymbol{c_p}$: cohesive strength parallel to bedding; $\boldsymbol{\varphi}$: friction angle (isotropic); $\boldsymbol{\tau_n}$: tensile strength normal to bedding; $\boldsymbol{\tau_p}$: tensile strength parallel to bedding; $\boldsymbol{\sigma'_v}$: maximum effective stress experienced by the formation; $\boldsymbol{\sigma_{NC}}$: effective stress at the present-day depth for normal consolidation at hydrostatic pore pressure; $\mathbf{UCS_{NC}}$: uniaxial compressive strength for normal consolidation at present-day depth; BRI: brittleness index; OCR: overconsolidation ratio; $\boldsymbol{\sigma_{pd}}$: present-day effective stress; $\boldsymbol{p}$: present-day pore-fluid pressure; $\boldsymbol{p_{hs}}$: hydrostatic pressure at present-day depth; $\boldsymbol{p_{op}}$: pore-fluid overpressure (or underpressure if negative) $(\boldsymbol{p - p_{hs}})$.**

At this point, the bulk of the output values in Table 3-5 have not been independently verified and should be treated as initial estimates. In particular, the correlations for Poisson's ratio, cohesive strength, friction angle, and tensile strength were built from a small number of measured values. The following four subsections provide some independent comparisons for some of the parameter estimates for the Barnett, Haynesville, Pierre, and Monterey Shales.

### 3.3.3 Barnett Shale

Bruner and Smosna (2011) give an average porosity of 0.06 for Barnett shale, which is reasonably close to the correlation value of 0.055 in Table 3-5. Parshall (2008) cites a range of $10^{-19}$ m$^2$ to $10^{-21}$ m$^2$ for Barnett Shale permeability. The correlation is on the low end of this range with 6.0 x $10^{-22}$ m$^2$ for normal to bedding and 1.8 x $10^{-21}$ m$^2$ parallel to bedding. It is anticipated that permeability computed from the correlation will generally tend to the low end of the range because the correlation represents undisturbed matrix permeability and damage (e.g., fracturing) would lead to higher values. The pore pressure is found to be slightly overpressured, consistent with observations reported by Bruner and Smosna (2011).

### 3.3.4 Haynesville Shale

Pope et al. (2010) give a porosity range of 0.06 to 0.12 for the Haynesville Shale, which is consistent with the correlation value of 0.084. The permeability computed from the correlation is 1.2 x $10^{-21}$ m$^2$ normal to bedding and 3.6 x $10^{-21}$ m$^2$ parallel to bedding. Wang and Hammes (2010) give a range of roughly $10^{-19}$ m$^2$ to $10^{-21}$ m$^2$ for Haynesville Shale permeability. Pressure gradients in the Haynesville Shale range from about 0.67 to 0.9 psi/ft (0.0152 to 0.0204 MPa/m) Wang and Hammes (2010). At a depth of 3000 m, this corresponds to pressures of 45 to 61 MPa, while the estimated pore pressure in Table 3-5 is 43 MPa. For a static water pressure of 29 MPa, this gives an overpressure of 16 to 32 MPa, with the Table 3-5 estimate at 14 MPa.

### 3.3.5 Pierre Shale

The Pierre shale is evaluated at two depths, 152 m and 1524 m. The estimated porosities from Table 3-5 are 0.36 and 0.13, respectively. Porosities reported by Nichols (1992) at depths ranging from 123 to 181 m was 0.36 and for 1500 m depth, Tosaya (1982) reports a porosity of 0.145. For porosity in the range of 0.3 to 0.4, Neuzil reports permeabilities for the Pierre Shale range from 2 x $10^{-21}$ to 5 x $10^{-19}$ m$^2$, a range covering both normal and parallel to bedding. The values in Table 3-5 are 7.4 x $10^{-20}$ m$^2$ normal to bedding and 8.6 x $10^{-20}$ m$^2$ parallel to bedding. These lie within the observed range although they do not tend to fall at the lower end of the observations as expected. Neuzil (1993) reports on underpressures on the order of -100 m head, or about -1 MPa at depths of 150 m, which is close to the estimated value in Table 3-5 of -0.70 MPa.

### 3.3.6 Monterey Shale

The velocity measurements reported in Tables 3-4 and 3-5 for the Monterey Shale are on a low-organic-content sample from an outcrop. In addition to sonic velocities, measurements of porosity and dry bulk density were performed and reported in Liu (1994). The value of porosity is 0.05 and 2730 kg/m$^3$ for dry bulk density. The estimated values of these parameters from Table 3-5 are 0.033 for porosity and 2650 kg/m$^3$ for dry bulk density.

## 3.4 CONCLUSIONS

Correlations for estimating hydrological and geomechanical formation properties and in-situ conditions from sonic velocities have been developed from data on shale formations that lie outside the United States. These correlations have been applied to estimate properties for several large shale formations in the United States. The advantage of using correlations based on sonic velocity is that properties can be estimated from geophysical logs. This information is often more readily available and in greater quantity than direct property measurements on core that would otherwise be required. Furthermore, geophysical logs provide a continuous readout along wells that can be more readily used to characterize spatial variability in properties.

Correlations developed for porosity, uniaxial compressive strength, Young's modulus, and shear modulus with the compressional sonic velocity are reasonably consistent with other correlations that have been documented in the scientific literature. The approach has been extended here to include several other properties: bulk density, clay content, permeability, Poisson's ratio, cohesive strength, friction angle, and tensile strength. The correlation for permeability is based on an existing correlation that requires porosity and clay content as inputs. However, this correlation is limited to the permeability of the undisturbed rock matrix. Therefore, ways to estimate bulk-rock permeability are still needed.

Anisotropy is often found in many shale properties as a result of their bedding structure. A method to account for anisotropy in the property correlations has been developed and applied to correlations for permeability, Young's modulus, cohesive strength, and tensile strength.

A method for the estimation of in-situ effective stress and pore-fluid pressure has also been developed. This is based on combining previously developed correlations for the maximum effective stress experienced by the formation, which requires porosity and clay content as inputs, as well as correlations linking the uniaxial compressive strength with the overconsolidation ratio.

Correlations for the bedding-parallel sonic velocity with the normal to bedding sonic velocity and for clay content with the mean sonic velocity were found to be relatively weak and should be supplemented with additional independent measurements if possible. All of the correlations require additional development and verification. In particular, correlations for Poisson's ratio, cohesive strength, friction angle, and tensile strength need to be checked with additional data because of a very limited number of documented values that could be identified to create the correlations. Several factors that can influence properties have not been investigated here, including confining stress, fluid saturation conditions, and the organic content of shale. Further verification is also needed for many of the parameter estimates in Table 3-5; therefore, they should be viewed as initial estimates.

## 3.5 REFERENCES

Baeyens, B., Bradbury, M.H. (1994). Physico-Chemical Characterisation and Calculated In Situ Porewater Chemistries for a Low Permeability Palfris Marl Sample from Wellenberg, Nagra Technical Report 94-22.

Bastiaens, W., Bernier, F., Li, X.L. (2007). SELFRAC: Experiments and conclusions on fracturing, self-healing and self-sealing processes in clays, Physics and Chemistry of the Earth, 32, 600–615.

Bock, H. (2001). RA Experiment Rock Mechanics Analyses and Synthesis: Data Report on Rock Mechanics, Mont Terri Project, Technical Report 2000-02.

Bock, H. (2009). RA Experiment: Updated Review of the Rock Mechanics Properties of the Opalinus Clay of the Mont Terri URL based on Laboratory and Field Testing, Mont Terri Project, Technical Report 2008-04.

Boisson, J.-Y. (2005). Clay Club Catalogue of Characteristics of Argillaceous Rocks, Nuclear Energy Agency, Organisation for Economic Co-Operation and Development.

Bruner,K.R. and R. Smosna 2011. A Comparative Study of the Mississippian Barnett Shale, Fort Worth Basin, and Devonian Marcellus Shale, Appalachian Basin, DOE/NETL-2011/1478.

Burland, J.B., Longworth, T.I., Moore, J.F.A. (1977). A study of ground movement and progressive failure caused by a deep excavation in Oxford Clay, Géotechnique 27, No. 4,557-591.

Charlier, R., Collin, F., Pardoen, B., Talandier, J., Radu, J.-P., Gerard, P. (2013). An unsaturated hydro-mechanical modelling of two in-situ experiments in Callovo-Oxfordian argillite, Engineering Geology, http://dx.doi.org/10.1016/j.enggeo.2013.05.021.

CNX/GTI (2008). New Albany Shale RVSP, New Albany Shale Gas Project, RVSP Seismic Project Report.

Dehandschutter, B., Gaviglio, P., Sizun, J.P., Sintubin, M., Vandycke, S., Vandenberghe, N., Wouters, L., (2005a). Volumetric matrix strain related to intraformational faulting in argillaceous sediments, Journal of the Geological Society, London, Vol. 162, 2005, pp. 801–813.

Dehandschutter, B, Vandycke, S., Sintubina, M., Vandenberghe, N., Wouters, L. (2005b). Brittle fractures and ductile shear bands in argillaceous sediments:inferences from Oligocene Boom Clay (Belgium), Journal of Structural Geology 27, 1095–1112.

EAEC (European Atomic Energy Community) (1984). Nuclear Science and Technology - Research Project for the Determination of the Suitability of the Mine 'Konrad' as a Final Repository for Radioactive Waste Products, Final report 1978-80, EUR 8984 EN.

EIA (Energy Information Administration) (2011). http://www.eia.gov/pub/oil_gas/natural_gas/analysis_publications/maps/maps.htm

Fedor, F., Hámos, G., Jobbik, A., Máthé, Z., Somodi, G., Sz}ucs, I. (2008). Laboratory pressure pulse decay permeability measurement of Boda Claystone, Mecsek Mts., SW Hungary, Physics and Chemistry of the Earth 33, S45–S53.

Geosites in Denmark (2013). Retrieved November 13, 2013, from http://geosites.dk/lokaliteter/jylland/hanklit.html.

Ghorbani, A., Cosenza, Ph., Revil, A., Zamora, M., Schmutz, M., Florsch, N., Jougnot, D. (2009). Non-invasive monitoring of water content and textural changes in clay-rocks using spectral induced polarization: A laboratory investigation, Applied Clay Science, 43, 493–502.

Giraud, A., Huynh, Q.V., Hoxha, D., Kondo, D. (2007). Application of results on Eshelby tensor to the determination of effective poroelastic properties of anisotropic rocks-like composites, International Journal of Solids and Structures, 44, 3756–3772.

Han, D.-H., Nur,A, Morgan, D. (1986). Effects of porosity and clay content on wave velocities in sandstones, Geophysics, Vol. 51. No. II; P. 2093-2107.

Hardage, B.A., Alkin, E., Backus, M.W., DeAngelo, M.V., Sava, D., Wagner, D., Graebner, R.J. (2013). Evaluation of Fracture Systems and Stress Fields Within the Marcellus Shale and Utica Shale and Characterization of Associated Water-Disposal Reservoirs: Appalachian Basin, Final Report to RPSEA, RPSEA Subcontract: 08122-55.

Horseman, S. T., McCann, D. M., McEwen, T. J., Brightman, M. A. (1986). Determination of the geotechnical properties of mudrocks .from geophysical logging of the Harwell boreholes. Report, Fluid Processes Research Group, British Geological Survey, FLPU 84-14.

Horsrud, P. (2001). Estimating Mechanical Properties of Shale From Empirical Correlations, SPE Drilling & Completion.

Ingram, G.W., Urai, J.L. (1999). Top-seal leakage through faults and fractures: the role of mudrock properties, from." Aplin, A. C., Fleet, A. J., Macquaker, J. H. S. (eds) Muds and Mudstones: Physical and Fluid Flow Properties. Geological Society, London, Special Publications, 158, 125-135.

Johnston, J.E., Christensen, N.I. (1995). Seismic anisotropy of shales, Journal Of Geophysical Research, Vol. 100, No. B4, pp. 5991-6003.

Jougnot, D., Revil, A., Lu, N., Wayllace, A. (2010). Transport properties of the Callovo-Oxfordian clay rock under partially saturated conditions, Water Resources Research, Vol. 46, W08514, doi:10.1029/2009WR008552.

Kerner, C., Dyer, B., Worthington, M. (1989). Wave propagation in a vertical transversely isotropic medium: field experiment and model study, Geophysical Journal, 7, 295-309.

Kutschke, W.G, Vallejo, L.E. (2012). Investigation of Lateral Stress Relief Using Finite Elements and Fracture Mechanics: Case History Study of the Saxon Pit, J. Geotech. Geoenviron. Eng., 138:1277-1283.

Lima, A., Romero, E., Piña, Y., Gens, A., Li, X. (2012). Water Retention Properties of Two Deep Belgian Clay Formations, in: Unsaturated Soils: Research and Applications 1, Mancuso, C., Jommi, C., D'Onza, F. (eds), Springer-Verlag, Berlin Heidelberg.

Liu, X. (1994). Nonlinear Elasticity, Seismic Anisotropy, and Petrophysical Properties of Reservoir Rocks, Ph.D. thesis, Stanford University.

Liu, E. (1997). Crosshole Channel Wave Analysis from Antrim Shale Gas Play, Michigan Basin, EAGE Conference and Technical Exhibition, 59th annual meeting 1997, European Association of Petroleum Geoscientists.

Matray, J.M., Savoye, S., Cabrera, J. (2007). Desaturation and structure relationships around drifts excavated in the well-compacted Tournemire's argillite (Aveyron, France), Engineering Geology 90, 1–16.

McDonal, F.J., Angona, F.A., Mills, R.I., Sengbush, R.L., Van Nostrand, R.G., White, J.E. (1958). Attenuation Of Shear And Compressional Waves In Pierre Shale, Geophysics, Vol. XXIII, No. 3, pp. 421-439.

Midttømme, K., Roaldset, E., Aagaard, P. (1998). Thermal conductivity claystones and mudstones of selected from England, Clay Minerals (1998) 33, 131-145.

Millard, A., Rejeb, A. (2008). Simulation of Short Term and Long Term Responses of the Tournemire Argillite in a Mine-by-test Experiment, The 12th International Conference of International Association for Computer Methods and Advances in Geomechanics (IACMAG) 1-6 October, 2008 Goa, India.

Montaut, A. 2012. Detection and Quantification of Rock Physics Properties for Improved Hydraulic Fracturing in Hydrocarbon-Bearing Shales, Master of Science in Engineering Thesis, The University of Texas at Austin.

Neuzil, C.E. (1993). Low Fluid Pressure Within the Pierre Shale: A Transient Response to Erosion, Water Resources Research, Vol. 29, No. 7, pp. 2007-2020.

Neuzil, C.E. (1994). How permeable are clays and shales? Water Resources Research, Vol. 30, No. 2, pp. 145-15.

Niandou, H., Shao, J.F., Henry, J.P., Fourmaintraux, D. (1997). Laboratory Investigation of the Behaviour of Tournemire Shale, Int. J. Rock Mech. Min. Sci. Vol. 34, No, 1, pp. 3-16.

Nichols, T.C. (1992). Rebound in the Pierre Shale of South Dakota and Colorado Field and laboratory evidence of physical conditions related to processes of shale rebound, U.S.G.S. Open-File Report 92-440.

Nunn, J.A. 2012. Burial and Thermal History of the Haynesville Shale: Implications for Overpressure, Gas Generation, and Natural Hydrofracture, GCAGS Journal, v. 1 (2012), p. 81–96.

Nygård, R., Gutierrez, M., Bratli, R.K., Høeg, K. (2006). Brittle–ductile transition, shear failure and leakage in shales and mudrocks, Marine and Petroleum Geology, 23, 201–212.

Parshall, J. (2008). Barnett Shale Showcases Tight-Gas Development, Journal of Petroleum Technology, Vol. 60, No. 9.

Piña-Diaz, Y.E. (2011). Thermo-Hydro-Mechanical Behaviour of Ypresian Clay, Dept. de Enginyeria del Terreny, Cartogràfica i Geofisica E.T.S. Enginyers de Camins, Canals i Ports, Universitat Politècnica de Catalunya.

Pope, C.D., Palisch, T.T., Lolon, E.P, Dzubin, B.A., Chapman, M.A. (2010). Improving Stimulation Effectiveness: Field Results in the Haynesville Shale, Society of Petroleum Engineers, Conference Paper 134165-MS, SPE Annual Technical Conference and Exhibition, 19-22 September 2010, Florence, Italy.

Shaw, R. (2010). Review of Boom Clay and Opalinus Clay parameters, FORGE Report D4.6 – VER 1.0. Euratom 7th Framework Programme Project.

Sondhi, N. (2011). Petrophysical Characterization of Eagle Ford Shale, M.S. Thesis, University of Oklahoma.

Tosaya, C.A. (1982). Acoustical Properties of Clay-Bearing Rocks, Ph.D. Dissertation, Standford University.

USGS (United States Geological Survey) (2013). http://mrdata.usgs.gov/geology/state/sgmc-lith.php?code=2.1.1

Verma, S., Mutlu, O., Marfurt, K.J. (2013). Seismic modeling evaluation of fault illumination in the Woodford Shale, SEG Houston 2013 Annual Meeting.

Volckaert, G., Bernier, F., Sillen, X., Van Geet, M., Mayor, J.-C., Göbel, I., Blümling, P., Frieg, B., Su, K. (2004). Similarities and Differences in the Behaviour of Plastic and Indurated Clays, http://cordis.europa.eu/fp6-euratom/ev_euradwaste04_proceedings.htm, The Sixth European Commission Conference on 'The Management and Disposal of Radioactive Waste: Euradwaste '04', held on 29-31 March 2004 in Luxembourg.

Wang, F.P., Hammes, U. (2010). Effects of petrophysical factors on Haynesville fluid flow and production, World Oil, June 2010.

Wenk, H.-R., Voltolini, M., Mazurek, M., Van Loon, L.R., Vinsot, A. (2008). Preferred Orientations and Anisotropy in Shales: Callovo-Oxfordian Shale (France) and Opalinus Clay (Switzerland), Clays and Clay Minerals, Vol. 56, No. 3, 285–306.

Wong, S.-W., Kenter, C.J. (1993). Optimising Shale Drilling in the Northern North Sea: Borehole Stability Considerations, SPE 26736, Offshore European Conference, Aberdeen, Scotland, 7-10 September 1993.

Wyllie, M.R.J., Gregory,A.R., Gardner, L.W. (1956). Elastic Wave Velocities in Heterogeneous and Porous Media, Geophysics, Vol. XXI, No. 1. pp. 41-70.

Wyllie, M.J.R., Gregory, A.R., Gardner, G.H.F. (1958). An Experimental Investigation of Factors Affecting Elastic Wave Velocities in Porous Media, Geophysics, Vol. XXIII, No. 3, pp. 459-493.

Yang, Y., Aplin, A.C. (2004). Definition and practical application of mudstone porosity–effective stress relationships, Petroleum Geoscience, Vol. 10, pp. 153–162.

Yang, Y., Aplin, A.C. (2010). A permeability–porosity relationship for mudstones, Marine and Petroleum Geology, 27, 1692–1697.

Zinszner, B., Meynier, P., Cabrera, J., Volant, P. (2002). Vitesse des ondes ultrasonores, soniques et sismiques dans les argilites du tunnel de Tournemire. Effet de l'anisotropie et de

la fracturation naturelle, Oil & Gas Science and Technology – Rev. IFP, Vol. 57, No. 4, pp. 341-353.

# 4. ACKNOWLEDGMENTS

Funding for this work was provided by the Used Fuel Disposition Campaign, Office of Nuclear Energy, of the U.S. Department of Energy under Contract Number DE-AC02-05CH11231 with Berkeley Lab.

From Lawrence Berkeley National Laboratory, Curt Oldenburg reviewed this report and his feedback was greatly appreciated. Editorial assistance was also provided by Helen Prieto and Peter Persoff.

Section 2 of this report represents a major collaborative effort with Frank Perry and Rick Kelley of Los Alamos National Laboratory (LANL). They have scanned and generated GIS data from pdf versions of isopach and structure maps, and have uploaded existing GIS data into their database. They used the resulting GIS data to create contoured structure and isopach maps.

In addition, many individuals generously shared their knowledge and data to help populate the GIS database described in Section 2. Steve Ruppel and Cari Breton of the University of Texas, Bureau of Economic Geology, provided us with their GIS dataset for the Woodford Shale in the Permian Basin. John Bocan, with the West Virginia Geological and Economic Survey, provided us with GIS data for the Utica Shale that had been developed by the Trenton-Black River Research Consortium. Jim McDonald of the Ohio Department of Natural Resources shared with us a regional GIS dataset for the Marcellus Shale. Christopher Korose of the Illinois State Geological Survey provided us with GIS data for the New Albany Shale that was developed by the Illinois Basin Consortium. Jeff Zimmerman of the Susquehanna River Basin Commission provided us with some USGS GIS data for the Utica and Marcellus Shales. David Effert of the Louisiana Department of Natural Resources gave us access to GIS data for the Haynesville Shale. Brian Cardott of the Oklahoma Geological Survey provided us with additional references on the Woodford Shale and Sue Palmer (also of the Oklahoma Geological Survey) provided us with pdf copies of plates depicting the thickness and depth of the Woodford Shale in the Anadarko Basin. Sue Hovorka of the University of Texas, Bureau of Economic Geology, pointed us towards a study conducted by the Gulf Coast Carbon Center, which contains abundant information regarding seals (i.e., shales) in many sedimentary basins in the US. Prof. James Wood (Michigan Tech) provided us with a copy of his digital dataset for the Antrim Shale in the Michigan Basin. Julie LeFever (North Dakota Geological Survey) shared her GIS data for the Bakken Formation. Sam Limerick helped us track down the source files for the EIA shale play maps, and Jack Perrin and Meg Coleman (US EIA) generously provided us with the associated GIS data. Don Sweetkind (USGS) shared the GIS data associated with his reports on the Monterey Formation in the Cuyama and Santa Maria Basins. Many thanks for all of their contributions.